SIZE EFFECTS IN

FERROMAGNETIC SHAPE MEMORY ALLOYS

A Dissertation

by

NEVIN OZDEMIR

Submitted to the Office of Graduate Studies of
Texas A&M University
in partial fulfillment of the requirements for the degree of

DOCTOR OF PHILOSOPHY

May 2012

Major Subject: Materials Science and Engineering

Size Effects in

Ferromagnetic Shape Memory Alloys

SIZE EFFECTS IN

FERROMAGNETIC SHAPE MEMORY ALLOYS

A Dissertation

by

NEVIN OZDEMIR

Submitted to the Office of Graduate Studies of
Texas A&M University
in partial fulfillment of the requirements for the degree of

DOCTOR OF PHILOSOPHY

Chair of Committee,	Ibrahim Karaman
Committee Members,	K. Ted Hartwig
	Xinghang Zhang
	Tahir Cagin
Interdisciplinary Faculty Chair,	Ibrahim Karaman

May 2012

Major Subject: Materials Science and Engineering

ABSTRACT

Size Effects in

Ferromagnetic Shape Memory Alloys. (May 2012)

Nevin Ozdemir, B.S., Anadolu University;

M.S., New Mexico Institute of Mining and Technology

Chair of Advisory Committee: Dr. Ibrahim Karaman

The utilization of ferromagnetic shape memory alloys (FSMAs) in small scale devices has attracted considerable attention within the last decade. However, the lack of sufficient studies on their reversible shape change mechanisms, i.e, superelasticity, magnetic field-induced martensite variant reorientation and martensitic phase transformation, at the micron and submicron length scales has prevented the further development and the use of FSMAs in small scale devices. Therefore, investigating the size effects in these mechanisms has both scientific and technological relevance.

Superelastic behavior of $Ni_{54}Fe_{19}Ga_{27}$ shape memory alloy single crystalline pillars was studied under compression as a function of pillar diameter. Multiple pillars with diameters ranging between 200 nm and 10 μm were cut on a single crystalline bulk sample oriented along the [110] direction in the compression axis and with fully reversible two-stage martensitic transformation. The results revealed size dependent two-stage martensitic transformation which was suppressed for pillar sizes of 1 μm and

below. We also demonstrated that the reduction in pillar diameter decreases the transformation temperature due to the difficulty of martensite nucleation in small scales.

Size effects in the magnetic field-induced martensite variant reorientation were investigated in the $Ni_{50}Mn_{28.3}Ga_{21.7}$ single crystals oriented along the [100] direction of the austenite phase. Single crystalline compression pillars were fabricated on the martensite twins between the sizes of 630 nm and 20 μm. It was found that the stress-induced and magnetic field-induced martensite variant reorientation are size dependent and became more difficult with the reduction in sample size. Surprisingly, it was still possible to magnetically activate the shape change in the micropillars which indicates the fact that magnetocrystalline anisotropy energy increases with the reduction in sample dimensions.

$Ni_{45}Mn_{36.6}Co_5In_{13.4}$ pillars between the 600 nm and 10 μm diameters were investigated along the [100] direction of the austenite to study the size effects in the magnetic field-induced phase transformation (MFIPT). MFIPT was obtained down to 5 μm size in these pillars with reasonable magnetic field levels similar to their bulk counterparts.

To my parents, my sister and Bedri

ACKNOWLEDGEMENTS

First of all, I would like to thank and extend my gratitude to my advisor, Prof. Ibrahim Karaman for his tremendous support and mentorship during my Ph.D. studies over the last four years. This dissertation would not exist if he had not given me the opportunity of pursuing a doctoral degree.

I would like to thank my committee members, Prof. K. Ted Hartwig, Prof. Xinghang Zhang and Prof. Tahir Cagin for their critical review and valuable suggestions.

This work has benefited from the use of the Focused Ion Beam at the Center for Integrated Nanotechnologies (CINT) in Sandia National Laboratories (SNL) and the use of the nanoindenter at CINT in Los Alamos National Laboratory (LANL). I would like to thank Dr. Nathan A. Mara at LANL for providing us with the nanoindenter and his valuable collaboration. I also would like to thank Douglas V. Pete at SNL for assisting with the use of the Focused Ion Beam.

This dissertation included experiments performed at National High Magnetic Field Laboratory located in LANL. I would like to thank Dr. Vivien Zapf who helped using the magnet and showed remarkable flexibility reserving the magnet time during my tight schedule at LANL.

I would like to thank Prof. Yuriy Chumlyakov for his discussions which helped me to gain a better understanding of the subject. I also wish to thank Dr. Esad Ozmetin for help with the modeling part of this dissertation and Dr. Ersin Karaca for sharing his

bulk material mechanical testing results. I would like to acknowledge the help of Robert Barber during the sample preparation steps.

I am very thankful to all the colleagues that I worked with in our laboratory over the years, who were very supportive and friendly: Dr. Kadri C. Atli, Ji Ma, Ebubekir Dogan, James A. Monroe, Sonia M. Razavi, Ruixian Zhu, Alper Evirgen, Dr. Burak Basaran, Cengiz Yegin, Erhan Akin and Murat Kaynak.

Thanks also to my dear friend Gokcen Aykac who hosted me in her house during my three months of stay in New Mexico while performing experiments at Sandia and Los Alamos National Laboratories. Her hospitality and giving friendship led me to overcome my difficult working conditions and accomplish my goal.

I am indebted to the endless love, support and encouragement I received from my parents and my sister. Without them, I could have never succeeded this far. Finally, I would specially like to thank my sweetheart, Bedri, who has always been there for me to share and support every aspect of my life. His unconditional love, patience and understanding comforted and motivated me throughout my Ph.D. studies.

NOMENCLATURE

A_f	Austenite finish temperature
AFM	Atomic force microscopy
A_s	Austenite start temperature
BSE	Backscattered electron
DSC	Differential Scanning Calorimetry
EDM	Electrical discharge machining
EDS	Energy dispersive spectroscopy
FIB	Focused ion beam
FSMA	Ferromagnetic shape memory alloy
M_f	Martensite finish temperature
M_s	Martensite start temperature
PPMS	Physical property measurement system
SE	Secondary electron
SEM	Scanning electron microscopy
SQUID	Superconducting quantum interference device
σ_c	Critical stress for austenite to martensite transformation
σ_r	Martensite reorientation stress
SMA	Shape memory alloy
WDS	Wavelength dispersive spectroscopy

TABLE OF CONTENTS

CHAPTER Page

CHAPTER Page

LIST OF FIGURES

Page

Page

Page

Page

Page

Page

Page

Page

Page

LIST OF TABLES

CHAPTER I

INTRODUCTION

This chapter describes the motivation and the need for investigating the size effects in Ferromagnetic Shape Memory Alloys (FSMAs). The mechanisms responsible for the reversible shape change in FSMAs were summarized and the importance of understanding these mechanisms at small structural length scales was discussed. Finally, the objectives of the present work were summarized together with the outline of the work performed.

1.1 Motivation and Significance

FSMAs offer both large strains comparable to that of conventional SMAs and fast response as in magnetostrictive materials. Due to their unique ability to convert magnetic energy into mechanical work, or heat, or vice versa, FSMAs are capable of magnetic field-induced actuation, sensing, magnetic refrigeration, and energy harvesting, making them truly multifunctional. However, the functional behavior of FSMAs at small structural length scales is completely unknown due to the lack of studies on the effect of length scales on magnetic field-induced shape changes. In FSMAs, there are two main mechanisms responsible for the magnetic field-induced shape change: the field-induced martensite reorientation/detwinning and field-induced martensitic phase transformation.

This dissertation follows the style of Acta Materialia.

Up to now, the former mechanism is the most studied one, especially in NiMnGa [1]. The latter mechanism is relatively new and was discovered in NiMnCoIn FSMAs demonstrating simultaneous structural and magnetic first order phase transformations and allowing magnetic field-induced martensitic transformation to take place [2]. In addition to these magnetically-induced shape change mechanisms, FSMAs also possess conventional shape memory alloy properties and exhibit thermally-induced shape memory effect and superelasticity.

Understanding stress-, temperature- and magnetic field-induced shape changes at small structural length scales is crucial for FSMAs due to their potential in small size scale applications. However, there is a limited number of studies on the effect of length scales in FSMAs and these studies do not present a fundamental understanding of the governing physics for the actuation mechanisms in micro/nano length scales. In the present work, the effects of structural size scales on the stress- and magnetic field-induced shape changes are systematically studied in micrometer and sub-micrometer length scales using NiFeGa, NiMnGa and NiMnCoIn FSMAs. These three alloys are ferromagnetic and demonstrate all major microstructural mechanisms that are unique to martensitic phase transformation and responsible for reversible external shape changes. The mechanisms that are investigated here are superelasticity in NiFeGa, martensite variant reorientation in NiMnGa and martensite variant reorientation and reverse martensitic transformation in NiMnCoIn alloys. They will be studied as a function of specimen size scale using bulk, micron and submicron size compression pillars. Thus, the overall goal of the present study is to investigate mechanical, magneto-mechanical

and magneto-microstructural properties of FSMAs at small length scales. We expect that FSMAs will exhibit different functionality at micron/nano length scales due to size dependence of these properties.

Size effects arise when the dimensional or microstructural constraints exist. These constraints become the "size parameter" which controls the materials behavior. The size parameter can be the sample size (e.g. film thickness, and fiber, pillar, wire and particle diameters) or the microstructural size (e.g. grain size, grain boundary width and obstacle spacing). These size parameters can interact with each other and with the "characteristic length" (e.g. the equilibrium diameter of a dislocation loop, spacing between partial dislocations and the width of a magnetic domain wall) which is related to a governing deformation mechanism or a physical phenomenon [3]. In this case, size effects become significant in materials. The presence of a length scale at which the size effects start to arise has been observed for various materials [4-6]. It is on the order of 1 μm for dislocation-mediated deformation [7], and is also observed to be similar for twinning [6]. We expect to see significant size effects in SMAs at several micrometers since twinning is one of the deformation mechanisms in SMAs. In addition to the critical microstructural length, the effect of decreasing specimen size on the magneto-microstructural coupling which is the correspondence between magnetic and microstructural domains in FSMAs is expected to have a strong influence on the magneto-mechanical behavior of FSMAs [8]. Therefore, the pillar diameter is the main size parameter in the present study, which is expected to have an influence on the microstructural length scale such as the twin width. As a result, the twin width becomes

the secondary size parameter whose interference with the magnetic domains and domain walls should be investigated to fully understand the size effects in FSMAs.

The studies reported in the literature to explain the size effects in superelasticity are only based on single-stage martensitic transformation in conventional SMAs. Superelastic behavior with two-stage phase transformation including martensitic and inter-martensitic transformations still needs to be understood at small length scales.

Bulk single crystal NiFeGa FSMAs have been shown to exhibit superelastic behavior with large recoverable strains up to 12-13% due to two-stage martensitic transformation at room temperature [9, 10]. The first-stage transformation includes the formation of modulated martensites (10M and 14M) from austenite ($L2_1$) whereas the second-stage governs inter-martensitic transformation between modulated martensite (14M) and non-modulated martensite ($L1_o$) [9-12]. In the present work, the size effects in superelasticity in SMAs showing two-stage phase transformation will be studied for the first time by fabricating and testing micron/sub-micron single crystalline compression pillars of NiFeGa FSMAs. Our findings on NiFeGa pillars are expected to shed light into the role of sub-micron and nano size scales on the stress-induced martensitic and inter-martensitic phase transformations to better assess their utility in small scale mechanical devices.

Besides superelasticity, the actuation mechanisms that result in magnetic field-induced shape changes in FSMAs will also be studied as a function of size. NiMnGa is chosen to study martensite reorientation at small length scales since it is the most well-known FSMA exhibiting large reversible field-induced shape change via martensite

reorientation [1]. NiMnCoIn is chosen to investigate the effect of small length scales on magnetic field-induced martensitic transformation since it demonstrates fully reversible field-induced transformation at reasonable field levels in bulk form. NiMnCoIn FSMAs possess the lowest transformation hysteresis among all FSMAs exhibiting field-induced phase transformation [2]. These mechanisms will be studied by fabricating micron and sub-micron compression pillars. Martensite reorientation stresses and magnetic field requirements to recover the shape in the deformed micron/submicron size pillars will be examined as a function of pillar size. The findings will not only lead us to develop a fundamental understanding on how these FSMAs would function as small structures but also provide crucial information for magneto- and microstructural evolution of these materials at small length scales.

Investigating micron/submicron single crystalline pillars will allow a direct comparison of small sample size behavior with their bulk counterparts. Since micron/submicron pillars are compression specimens with small sizes, they provide the most valuable information among the other small scale specimens such as thin films, particles, wires etc. for comparison with the bulk mechanical response under compression. In addition, preparing different size specimens by keeping the same composition is quite challenging and hard to achieve with other techniques such as thin film deposition. With micron/sub-micron pillar fabrication on bulk crystals these significant compositional differences are eliminated between the specimens with various sizes.

It is crucial whether the size parameter under consideration is surrounded by free space or is constrained [13]. The size parameter which is the sample size in the present work is not constrained by its surrounding. In addition, in small scale structures one or two dimensions are much larger than other(s). For example, fibers have one dimension much larger than the other two dimensions and films have two dimensions much larger than the third dimension. This dimensionality is also expected to affect material behavior at small length scales due to the surface effects. Thus, as compared to other small structures, micro/nano pillars exhibit more representative character of the bulk single crystals since they are also single crystalline specimens with similar dimensionality to the bulk and their size is not constrained by the surrounding material. For this reason, in order to investigate size effects in FSMAs from bulk to submicron size scale, fabricating, testing and characterizing micron/submicron was selected as the main focus of this work.

1.2 Objectives

The objective of the present study is to investigate the sample size effects in FSMAs in order to utilize them in small scale applications. For this purpose, it is crucial to understand how the reversible shape change mechanisms in FSMAs function at small structural length scales. Therefore, the current study investigates the three underlying mechanisms of FSMAs as a function of the specimen size. These mechanisms are superelasticity due to stress-induced martensitic transformation, martensite variant reorientation and magnetic field-induced martensitic transformation. Investigating a two-stage superelasticity instead of a single-stage one is one of the goals here since there is

no work describing the size effects in two-stage martensitic transformations in the literature.

The first focus of this study is to choose the materials with right compositions and crystallographic orientations, which show good characteristics for two-stage superelasticity, martensite variant reorientation, and magnetic field-induced phase transformation in their bulk forms. The second focus is to decrease the size of these bulk specimens into micron and submicron length scales and fabricate the samples in order to investigate these mechanisms at the small length scales. The materials selected for this purpose are $Ni_{54}Fe_{19}Ga_{27}$, $Ni_{50}Mn_{28.3}Ga_{21.7}$ and $Ni_{45}Mn_{36.6}Co_5In_{13.4}$ single crystals along the [110], [100] and [100] crystallographic directions of austenite, respectively.

The overall objectives of this study can be summarized as follows;

1) Investigate the size effects on the two-stage superelasticity in NiFeGa FSMAs. The investigation of the size effects on this mechanism will provide an understanding on the achievable stress levels and the recoverable strains at micron and submicron length scales. The stress-induced martensitic transformation path will also be identified at these small length scales. The compression pillars will be prepared from single crystalline bulk samples. Producing micron/submicron pillars of different sizes from bulk single crystals should provide opportunity for comparison with the bulk superelastic behavior of the same composition and orientation. In order to evaluate the performance of this material at small length scales, the size dependence of the following parameters/characteristics will be monitored:

a) Critical stress required for austenite to martensite phase transformation;

b) Stress hysteresis;

c) Superelastic behavior / Recoverability;

d) Nature of the inter-martensitic transformation path;

e) Critical stress required for plastic deformation of martensite.

2) Investigate the size effects on the martensite variant reorientation/detwinning in NiMnGa FSMAs. The study of the size effects on this mechanism will result in insights to the stress-favored or magnetic field-favored twin boundary motion as a function of size. The nature of this mechanism is not well understood at the submicron length scales due to the absence of systematic works in this field, especially in unconstrained structures. Our work here will provide an understanding on the nature of this mechanism and the changes observed as a function of sample size. Size dependence of the following parameters/characteristics will be examined and discussed on NiMnGa pillars:

a) The stress required for martensite reorientation and detwinning;

b) Martensite reorientation strain;

c) Critical magnetic field required for martensite reorientation (recovery);

d) Magnetocrystalline anisotropy energy;

e) Magneto-microstructural coupling.

These findings will not only lead us to develop a fundamental understanding on how these FSMAs would function as small structures but also provide crucial information for magneto- and microstructural evolution of these materials at small length scales.

3) Investigate the size effects on the magnetic field-induced martensitic transformation in NiMnCoIn FSMAs. The investigation of the size effects in this mechanism will prove if this mechanism can still be utilized at micron and submicron length scales. Magnetic field-induced martensitic transformation was not systematically examined at this length scale before. Therefore, our goal is to prepare different size single crystalline micron/submicron pillars and examine the evolution of this mechanism in these pillars. Size dependence of the following parameters/characteristics will be determined on NiMnCoIn pillars:

a) The stress required for martensite reorientation;

b) Martensite reorientation strain;

c) Recoverability due to magnetic field-induced martensite to austenite reverse transformation.

With these objectives, the outline of this dissertation is as follows;

CHAPTER II: A brief literature review on the size effects in SMAs and FSMAs. The literature review includes two main parts; the superelasticity and shape memory effect at small length scales and the magnetic field-induced actuation at small length scales.

CHAPTER III: Experimental methods used in this study.

CHAPTER IV: The investigation of the size effects in the two-stage superelasticity in NiFeGa FSMAs.

CHAPTER V: The investigation of the size effects in the magnetic field-induced martensite reorientation in NiMnGa FSMAs.

CHAPTER VI: The investigation of the size effects in the magnetic field-induced phase transformation in NiMnCoIn FSMAs.

CHAPTER VII: Summary, main conclusions and the future directions.

CHAPTER II

BACKGROUND

This chapter summarizes the current literature related to the objectives of this study. The background is separated into two sections to give a relevant comparison between the reported studies and the experimental results in this dissertation.

2.1 Superelasticity and Shape Memory Effect at Small Length Scales

Size effects in superelasticity and shape memory behavior have gained an increasing attention due to potential utilization of shape memory alloys (SMAs) in small scale devices [14-18]. Various studies investigating size effects in SMAs have been reported in the literature [5, 19-31]. These investigations can be categorized into two groups as those conducted on constrained structures and others on unconstrained ones. The constrained structures mostly involved nanocrystalline materials, thin films and particles embedded in a matrix.

Nanocrystalline NiTi SMAs have been investigated in order to reveal the size effects mostly in thermally-induced martensitic transformation. Martensitic transformation was fully suppressed when the grain size decreased below 50-60 nm due to large interface energies leading to an increased energy barrier for transformation [5, 32]. In nanocrystalline SMAs, the transformation strains are accommodated and thus the strain energy is minimized by the formation finely twinned martensitic structure with an

optimum twin width; i.e. the compound twins having widths in atomic scale (2 nm) were observed in nanocrystalline NiTi SMAs [5]. Below a critical crystal size, the formation of large surface to volume ratio starts to have a significant effect on the contribution of the total surface energy per unit of transformed volume to the total free energy of transformation. Therefore, energy required to form martensite increases as the grain size decreases and suppression of martensitic transformation takes place below a critical size in nanocrystalline SMAs [5]. Complete suppression of martensitic transformation in NiTi thin films was also reported below ~50 nm thickness by mechanical testing [19] and electrical resistivity measurements [20]. It was suggested that the formation of surface oxides and interfacial diffusion layers restricted the phase transformation in such thickness range in addition to causing stoichiometric changes in the film [19]. In thin films, spatial constraints by the film surface and the film/substrate interface dominate the transformation process in thinner films eventually preventing lattice distortion and twinning [20]. These constraints also decreased the transformation strain in NiTi films with 500 nm thickness as compared to that of the thicker films [21]. Similarly, ultra thick NiTi films up to 10 μm thickness were shown to have lower transformation temperatures than their bulk counterparts [23]. This is consistent with the size effects found in NiTiCu foils. NiTiCu foils having thicknesses of 20-100 μm were compared with the foils exposed to additional chemical thinning down to below 5 μm revealing the decrease in the martensitic transformation temperatures with decreasing film thickness [22]. The presence of a critical size for suppression of martensitic transformation was shown for NiTiCu nanoparticles embedded in an amorphous matrix. Transformed nanocrystal

volume decreased as the size of the crystal became smaller and a critical size of less than 16 nm was reported at which the martensitic transformation was fully suppressed [24]. Clearly, there seems to be a dimensionality effect where the reduction in transformation temperatures with smaller size depends on whether the size is smaller in 3-D (nanograins, particles), 2-D (wires) and 1-D (thin films).

Besides these constrained structures, size effects in martensitic transformation have been investigated in free-standing structures where the influence of dimensionality is more obvious. Free-standing AuCd nanoparticles were observed to possess lower martensitic transformation temperatures when their sizes are down to 6 nm than that of 46 nm particles which showed bulk-like transformation temperatures [33]. NiTi nanopowders also demonstrated thermally-induced martensitic phase transformation in an average crystal size of ~50 nm [25]. Similarly, in-situ TEM studies on free-standing In-Tl nanowires reported that when compared with bulk no size effect is present in phase transformation behavior within the diameter range of 10-650 nm [26]. In addition, microwires with the diameters down to 23 μm exhibited superelastic behavior with full recovery however wires with smaller diameters showed higher transformation temperatures studied by differential scanning calorimetry demonstrating opposite size effect from what has been summarized above [31].

Compression pillars have also been studied to determine the size effects in superelasticity and temperature-driven shape memory behavior. Norfleet et al. [34] and Manjeri et al. [35] showed fully recoverable superelastic response of NiTi pillars at micron size scale. Norfleet et al. studied NiTi compression pillars prepared with FIB

lathe machining technique which produces uniform cross-sections. The micron-scale (5 μm and 20 μm) samples showed a forward transformation plateau stress which is ~60 MPa higher than that of bulk with the same composition [34]. Studies on smaller pillar sizes were also reported. CuNiAl sub-micron compression pillars in the size range between 900 nm and 1.6 μm exhibited superelastic behavior [29, 30]. When compared with its bulk, 900 nm pillar size was shown to have significant size effect in critical stress for austenite to martensite phase transformation and stress hysteresis [29]. Clearly the critical stress required for martensitic transformation in SMAs follows a similar trend in size effect with plastic deformation of metals, i.e. the materials become stronger when their sizes get smaller [4, 6, 36-41]. Furthermore, NiTi pillars with diameters between 2 μm and 400 nm showed superelasticity however when compared with the bulk response, irrecoverable strains appeared at lower applied strains. Frick et al. showed that superelasticity deteriorated with decreasing pillar size and complete suppression of superelasticity was observed for diameters below 200 nm [27, 42]. By testing NiTi compression pillars under in-situ TEM, Ye et al. evidenced stress-induced austenite to martensite phase transformation in the sample size range below 200 nm [43]. They also showed large recoverable response in the stress-strain plots due to pseudoelastic response coming from the substrate [43], most likely due to small substrate geometry underneath the pillar. The findings by Frick et al. and Ye et al. reveal that the stress-induced austenite to martensite phase transformation takes place at the 200 nm length scale but this transformation can be irreversible upon unloading.

Recovery due to temperature-induced shape memory behavior upon bending of CuNiAl [30] and NiTi [28] micro/nanopillars was also studied. It was shown that thermally-driven shape memory effect was achieved for CuNiAl bending pillars with 1.8 μm and ~300 nm diameters [30] and for NiTi pillars with 1.2 μm down to 200 nm diameters [28]. These findings support the aforementioned results by Ye at al. [43] that the martensite still forms at 200 nm but conflict with the suppression of pseudoelasticity in NiTi [27] at this length scale. However, the recoverable strains at 200 and 300 nm NiTi pillars were reported to be low which may indicate the deterioration in shape memory effect below 200 nm. Recovery due to temperature-induced shape memory behavior in pillars has not been systematically studied and no critical size below which the shape memory effect is suppressed has been reported for unconstrained structures.

In SMAs, stress required for the plastic deformation of martensite was studied using micro/nano pillars of NiTi with precipitates. Testing NiTi pillars along the same orientation including precipitates demonstrated size-independent flow stress required for martensite yielding [27, 28]. Since the spacing between the precipitates was smaller than the pillar diamater, this size-independent behavior is expected in this case. In order to study size effects in plasticity of martensite, single crystalline pillars without precipitates are required to be investigated to prevent precipitate spacing from becoming the controlling size parameter. For this reason, in the present work, we focused on single crystalline pillars with no precipitates to systematically study plasticity at sub-micron length scale.

When size effects in SMAs are considered, the effects of different length scales on the superelastic behavior and shape memory effect are addressed. Correspondingly, change in critical stress (σ_{cr}) required to form stress induced martensite and shift in martensitic transformation temperature (M_s) with reduction in size are main parameters that identify the presence of the size effects in SMAs. The size effects arise when the external size of the sample becomes comparable to the microstructural parameters, i.e. grain size, particle spacing, and to the characteristic length, i.e. diameter of a dislocation loop, related to a physical mechanism [3]. Therefore when investigating size effects in martensitic transformation, it is critical to consider the sample size, sample geometry, sample dimensionality (i.e. 1-D, 2-D, and 3-D) and the size under consideration being constrained or not. Depending on these size parameters, the change in observed behavior is mainly because of reduction in M_s and increase in dissipation with smaller size.

Various mechanisms have been introduced to explain the aforementioned size effects reported in the literature. All the observations and arguments have been mainly explained by the effect of crystal size on the kinetics of nucleation and propagation of martensite and on the thermodynamical aspects contributing to the free energy change required for transformation. For example, suppression of martensitic transformation by decreasing particle size has been statistically rationalized by the lack of pre-existing nucleation sites in small particles. According to this statistical model, below a certain size, particles have negligible probability of having pre-existing nucleation sites and will remain untransformed even upon large undercooling [44]. Another approach explains the stabilization of austenite due to prevention of growth of martensite. Small austenite grain

size or closely-spaced boundaries limit the size of martensite units by inhibiting their growth after nucleation [45, 46] even though increased grain boundaries of austenite provide more nucleation sites for martensite [45]. In other words, the density of nuclei can be increased with smaller grain size however the net fraction of martensite decreases in comparison to that of martensite in larger grains [46]. As a result, more undercooling, thus lower experimental M_s is required to detect the transformation in finely grained austenite [45]. Another explanation has been introduced for nanocrystalline materials that the increase in grain boundary area also increases the barrier energy required for martensitic transformation due to larger surfaces, resulting in suppression of transformation below a critical grain size [5]. Effects of constraints for martensitic transformation such as irreversibility of the equilibrium microstructure and incompatibility between martensite and austenite due to formation of non-invariant interface have also been introduced for thin films. Since the accommodating microstructure for austenite/martensite and film/substrate interface constraints can be different in thin films, different domain structures form leading to an irreversible transformation [47]. In unconstrained structures such as pillars, difficulty in martensitic transformation for small sizes has been related to the lack of nucleation sites [29], which has similarities with crystal strengthening due to dislocation starvation in small sizes [4, 48, 49].

2.2 Magnetic Field-induced Actuation at Small Length Scales

In magnetic field-induced actuation, besides the size effects mentioned for conventional shape memory alloys in Section 2.1, the change in martensite reorientation stress and critical magnetic field required for actuation is expected. We also expect that magneto-microstructural coupling will have a significant effect on the field-induced martensitic transformation in these materials and change the martensite reorientation and phase transformation characteristics at lower micron and submicron length scales. This is due to the fact that one-to-one correspondence between magnetic domains and martensite twins are sometimes observed in NiMnGa FSMAs, i.e. martensite twin size is dictated by magnetic domains. Such magneto-structural correspondence and the control of magnetic domains with specimen shape and size control led to a two-fold increase in actuation stress levels in NiMnGa experiencing field-induced martensite reorientation [8]. However, this study was the only one demonstrating the importance of magneto-structural coupling and the effect of length scales on the field-induced martensite reorientation, without presenting a fundamental understanding of the governing physics.

Literature on the size effects in magnetic actuation involves studies on fibers, particles obtained from fibers, pillars and films. Size effect for fibers was dictated by the grain size for which magnetic field-induced strain (MFIS) increased by the increase in grain size with bamboo structure spanning across the fiber diameter [50]. There is only one micropillar study reported for the rectangular pillars with 10 μm x 15 μm cross-section, which does not demonstrate magnetic field-induced actuation [51]. Magnetic field-induced phase transformation was demonstrated for epitaxially grown NiMnGa

thin films with 500 nm thickness [52]. Magnetic field-induced strain (MFIS) up to 0.065% was obtained due to martensite reorientation in NiMnGa thin films (0.1-1μm thickness) attached to substrates [16, 53] and magnetic field-induced martensite reorientation was shown in NiMnGa thin films without demonstrating external strain [54-59].

CHAPTER III

EXPERIMENTAL METHODS

This chapter describes the experimental methods used in this dissertation. First of all, the experimental methods for the bulk samples were introduced. Then, the pillar fabrication, pillar testing and characterization

3.1 Experimental Methods for the Bulk Specimens

3.1.1 Bulk Materials Fabrication

A NiFeGa ingot with a nominal composition of $Ni_{54}Fe_{19}Ga_{27}$ (at. %) and a NiMnCoIn ingot with a nominal composition of $Ni_{45}Mn_{36.6}Co_5In_{13.4}$ (at. %) were prepared with vacuum induction melting. Single crystals were grown using the Bridgman technique in He atmosphere. $Ni_{50}Mn_{28.3}Ga_{21.7}$ (at. %) single crystal was provided from AdaptaMat.

3.1.2 Compositional and Calorimetric Analysis

Compositional analysis of the bulk specimens used in this study was performed using a Cameca SX50 (Gennevilliers Cedex, France) scanning electron microscope (SEM). SX50 is equipped with four wavelength dispersive X-ray spectrometers (WDS) and an energy dispersive X-ray spectrometer (EDS) in combination with BSE (Backscattered Electron) and SE (Secondary Electron) detectors. All the quantitative

work was conducted using the wavelength-dispersive spectrometers at an accelerating voltage of 15 kV and a beam current of 20 nA. BSE imaging was performed to find the area of interest to determine the composition of the single crystals.

Calorimetric measurements were carried out in order to find the phase transformation temperatures of the bulk specimens used in the present study. These temperatures are called martensite finish, M_f; martensite start, M_s; austenite start, A_s; and austenite finish, A_f temperatures and were measured using a Perkin- Elmer Pyris I differential scanning calorimeter (DSC) at a heating-cooling rate of 10 °C/min and 30 ^{o}C/min. The DSC specimens were obtained using wire electrical discharge machining (EDM) as 1 mm thick discs with 5 mm diameter.

3.1.3 Magnetic Characterization of the Bulk Specimens

Characterization of magnetic properties was performed to obtain thermo-magnetization response and the change in magnetization as a function of magnetic field using the Quantum Design superconducting quantum interference device (SQUID). For the NiMnGa single crystal, magnetic field versus magnetization response was recorded using the magnetic field application rate of 500 Oe/min. To determine the magnetic field-induced phase transformation characteristics of the NiMnCoIn single crystal, thermo-magnetization response was measured by heating and cooling the specimen with 5K/min at a constant magnetic field up to 7 Tesla.

3.1.4 Bulk Mechanical Testing

Bulk mechanical testing involved studying two mechanisms under compression; superelasticity and martensite reorientation.

Superelasticity experiments were performed on the NiFeGa single crystals with their compression axis along the [110] crystallographic direction. The size of the specimens used was 4 mm x 4 mm x 8 mm except the one sample having 4 mm x 4 mm x 7 mm dimensions which was shortened to obtain the 1 mm thick sample used for pillar machining. These compression samples were used for bulk testing in the temperature range between 22 ^{o}C and 80 ^{o}C in order to reveal the superelastic behavior in the single crystals. Two room temperature (22 ^{o}C) experiments were performed. The first experiment was conducted with a 4 mm x 4 mm x 8 mm sample using an MTS servohydraulic test frame which was also used to perform the high temperature experiments. The second experiment used the 4 mm x 4 mm x 7 mm sample (the rest of the sample used to obtain the sample for pillar fabrication) in order to prevent possible compositional changes between the pillars and the bulk crystal. The second room temperature test was conducted using an electromechanical MTS testing system.

The room temperature superelasticity experiment on the NiFeGa bulk single crystal compression specimen, performed using an electromechanical MTS testing system, used a miniature extensometer. This extensometer had a 3 mm gauge length and was directly attached on the sample to measure the axial strain. The strain rate during testing was $5x10^{-4}$.

One room temperature experiment and all the compression experiments at high temperatures on the NiFeGa single crystals were conducted using an MTS servohydraulic test frame. The specimens were either thermally cycled under constant applied stress or stress was loaded and then unloaded at constant temperature. A capacitive displacement sensor (Capacitec, Ayer, MA) was utilized to measure the strain for tests that are performed at high temperatures. Stable heating and cooling rates were obtained using Omega CN8200 series temperature controllers with K type thermocouples attached to the test specimen and the nonmagnetic compression grips. Fluctuation of the actual temperature readings from the set point was at most $\pm 1^{o}C$. Nitrogen gas was supplied into the chamber enclosing the test specimen. Cryogenic grade, ON/OFF solenoid valves were used to control the flow of nitrogen and are commanded by the temperature controllers. In this polymer chamber, the temperature could be varied from 200 ˚C down to -110 ˚C.

Martensite reorientation under compression was performed at room temperature on the NiMnGa single crystal by the electromechanical MTS testing system used for the NiFeGa crystal. The NiMnGa compression specimen was 3.2 mm x 5.3 mm x 7 mm with the compression axis along the [100] orientation of the austenite. Strain was measured using an extensometer with 12.7 mm gage length, which was attached to the grips.

3.2 Experimental Methods for the Micron/Sub-micron Pillars

3.2.1 Sample Preparation for Pillar Fabrication

Slices with the dimensions of 4 mm x 4 mm x 1 mm, 3.2mm x 5.3mm x 3mm and 2mm x 2mm x 1mm were cut from one end of the NiFeGa, NiMnGa and NiMnCoIn compression specimens respectively, with EDM to be used for machining micron/sub-micron compression pillars. These bulk sample slices were cut from the bulk compression specimens in a way that the pillars could be made on the desired surface of the bulk specimens. The NiFeGa pillars were machined on the (110) plane of the austenite (4mm x 4mm surface) such that their compression axis was along the [110] crystallographic direction. The NiMnGa pillars were prepared on the (100) plane of the austenite (3.2mm x 5.3mm surface) as their compression axis were along the [100] direction. The NiMnCoIn pillars were cut on the surface of the (100) plane of the austenite (2mm x 2mm surface) therefore the longitudinal axis of the pillars were along the [100] orientation.

The NiFeGa sample to be used for pillar preparation was ground and polished down to 0.05 μm alumina slurry with a lapping fixture to keep the surfaces parallel. This sample was completely austenite at room temperature and it was used in as-received condition without any heat treatment after the single crystal fabrication process. The NiMnCoIn bulk sample slice to be used for pillar fabrication was heat treated in vacuum environment at 900 ^{o}C for 24 hrs and then water quenched. This homogenization process provided the formation of continuous martensite plates at room temperature, in which

the pillars were later fabricated. NiMnGa slice cut for pillar fabrication was an electropolished sample, thus, the pillars were machined on an electropolished surface.

3.2.2 Pillar Fabrication

An FEI Nova 600 NanoLab Dual Beam^{TM} Focused Ion Beam (FIB) system was used to machine the compression pillars along the [110], [100] and the [100] orientations of the NiFeGa, NiMnGa and NiMCoIn single crystals respectively at the Center for Integrated Nanotechnologies (CINT) in Sandia National Laboratories (SNL). The NiFeGa pillars had diameters ranging from 10 μm to 235 nm, the NiMnGa pillars had diameters between 20 μm and 630 nm and the NiMnCoIn pillars were machined in diameters between 10 μm and 500 nm.

The pillar fabrication initially involved opening the pillar surrounding with rough-milling, then forming the pillars in the middle of this opening with finer cutting steps. Figure 3.1 shows the 5 μm pillar with trench surrounding it. The purpose of creating a large opening around the pillars is to allow the indenter to come in contact with the pillar without touching any surrounding material. First, a crater of a 70 μm outer diameter and a 30 μm inner diameter was cut away using 30 keV accelerating beam voltage and 7 nA beam current. Then, the desired diameter of the pillar was achieved by further milling with decreasing beam current in several steps. The finest milling of the pillars was carried out using the beam current of 100 pA for the 10 μm and 5 μm pillars and 10 pA for the smaller pillars to minimize Ga^+ ion damage. These beam currents used for the final milling produces less than 20 nm Ga^+ ion implantation to the

FIB machined samples [60]. This much Ga^+ damage is not expected to cause any significant effect in the superelastic responses of these pillars. However, it is important to notice that the smaller pillars have larger ion implanted sections than the larger pillars. The aspect ratio of the pillars in the present study was kept between 2.5:1 and 3.5:1 which falls within the suggested range for preventing buckling while still ensuring that the deformation is not hindered by the material beneath the pillar [40].

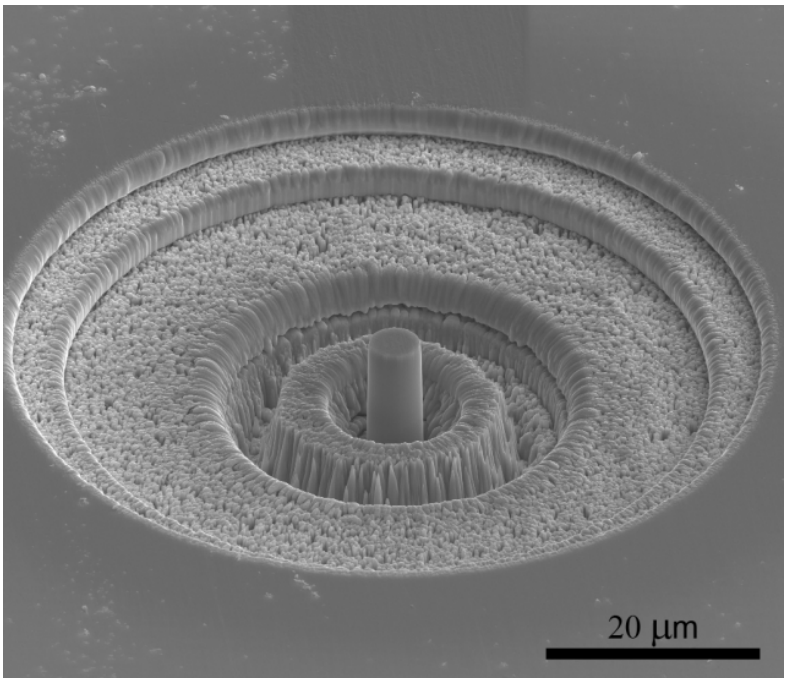

Figure 3.1 Scanning electron microscopy image of a 5 µm pillar and the trench surrounding it.

3.2.3 Pillar Mechanical Testing / Micro-mechanical Testing

Compression testing of the pillars was performed using an instrumented Hysitron Triboindenter at CINT in Los Alamos National Laboratory (LANL). Two types of indenter tips were used for the testing. A flat diamond punch of 30 μm diameter was used to test the 10 μm and 5 μm pillars, whereas for the 1 μm and smaller pillars, a diamond sphero-conical tip with 100 μm tip diameter was used. The uniaxial pillar compression experiments were conducted using the displacement controlled testing mode with a constant displacement rate of 2 nm/sec. All the pillar compression tests were carried out at room temperature. The drift correction was included in the displacement data obtained from the nanoindenter. This was automatically done by the nanoindenter software according to the drift rate calculated during the drift analysis period performed before each test was started. The drift rate monitoring was conducted for 300 sec and the last 40 sec of this time period was utilized to calculate the drift rate. Such a long drift rate monitor time was chosen to completely stabilize the system before starting the compression experiment and to minimize any thermal drift during the test. Since the superelasticity tests involve austenite to martensite phase transformation which gives rise to an exothermic reaction, it is crucial to start the experiment when the system is completely stabilized.

3.2.4 Geometrical and Microstructural Characterization of Pillars

Scanning electron microscopy (SEM) imaging of the pillars was performed before testing to measure their precise dimensions. These dimensions were later used to

obtain engineering stress-strain plots. Pillar manufacturing with FIB, except the FIB lathe milling technique [39], results in slightly tapered pillars since the ion beam is kept normal to the sample surface. In this study, the pillar taper determined using SEM imaging range between 1.2^{o}-5.2^{o}. Engineering stress-strain plots after the compression testing were calculated using the load and displacement data. The diameters at the half of the pillar heights were used to determine the stresses, in order to prevent the overestimation of the stress levels by only considering the top diameters. The diameters at the half of the pillar heights were determined using the SEM images.

After deforming the pillars, SEM images were taken again to observe the permanent deformation on the pillars. The change in the microstructure such as the appearance of the remnant twins and the twin boundary motion upon compression was identified using the SEM micrographs. SEM was also used to capture the twin boundary motion in NiMnGa pillars due to martensite reorientation by taking images before and after magnetic field application. Similarly, magnetic field-induced phase transformation in NiMnCoIn pillars was also observed using the SEM micrographs by the evolution of the new martensitic twins after the application of magnetic field. All the SEM images were taken using the secondary electrons (SE).

3.2.5 Magnetic Characterization of Pillars

Magnetic field experiments were performed on the pillars in order to obtain magnetic field-induced recovery of the deformed NiMnGa and the NiMnCoIn single crystal pillars via martensite reorientation and martensite to austenite phase

transformation respectively. Quantum Design physical property measurement system (PPMS) device was used to apply the magnetic field to the pillars.

The bulk specimens which had the FIB machined pillars on their top surfaces were attached to the PPMS sample holder using GE varnish in a way that the applied magnetic field was perpendicular to the compression axis of the NiMnGa pillars and parallel to the compression axis of the NiMnCoIn pillars. After the sample was placed inside the magnet, magnetic field was loaded and unloaded with a rate of 50 Oe/sec at 300 K. 2 Tesla and 5 Tesla magnetic fields were applied to the NiMnGa pillars while 8 Tesla and 12 Tesla fields were reached for the NiMnCoIn pillars. When the test was finished, the sample holder was withdrawn and the bulk specimen was separated from the holder using acetone and cleaned with ethyl alcohol or isopropanol for further SEM imaging.

3.2.6 Measurement of Pillar Profiles

The recovery of the NiMnGa pillars was quantified using the Hysitron TI 900 atomic force microscopy (AFM) with the imaging performed by the SPIP^{TM} software. The top surfaces of the pillars and the surrounding material outside the 70 μm opening were scanned at the same time in order to define reference points on the surrounding material. The AFM scans were conducted in the tapping mode and the cantilever type AFM probe with a sharp tip was used for all images. The z-axis range of this AFM is 4.5 μm with the z-axis resolution of 0.7 A^{o} and the x- and y- axis resolution of 7 A^{o}. 50 μm

x 50 μm square regions were scanned by locating the pillar in the center of this area. The 0.25 Hz scan rate was used to take all the AFM images.

The AFM scans of the pillars were first taken before the deformation to determine the initial pillar profiles. After the pillar deformation, they were again scanned with AFM to obtain the height profiles for the deformed pillars. Finally, after magnetic field application, the AFM scans were conducted once more to quantify the magnetic field-induced recovery of the pillars by comparing their profile heights after each of these steps.

CHAPTER IV

SIZE EFFECTS IN SUPERELASTIC RESPONSE OF $Ni_{54}Fe_{19}Ga_{27}$ SHAPE MEMORY ALLOY PILLARS WITH TWO-STAGE MARTENSITIC TRANSFORMATION

4.1. Introduction

Superelastic behavior of $Ni_{54}Fe_{19}Ga_{27}$ Shape Memory Alloy single crystalline pillars oriented along the [110] direction was studied under compression as a function of pillar diameter. The studies performed to explain the size effects in superelasticity are mainly based on single-stage martensitic transformation. In the present work, we studied, for the first time, the size effect in superelasticity in an SMA that shows two-stage martensitic transformation in bulk form. For this purpose we selected the $Ni_{54}Fe_{19}Ga_{27}$ SMA composition. Single crystalline NiFeGa SMAs have been shown to exhibit superelastic behavior with large recoverable strains up to 12-13% due to a two-stage martensitic transformation at room temperature [9, 11]. This first-stage of the transformation path includes the transformation from $L2_1$ austenite to a mixture of modulated martensites (10M and 14M) whereas in the second-stage the modulated martensites transform into non-modulated $L1_o$ martensite [9, 11]. Both 10M and 14M martensites both possess monoclinic structures and $L1_o$ martensite has a tetragonal structure [9]. Depending on the orientation, composition and testing conditions (temperature, tension or compression) the phase transformation in NiFeGa SMAs show

different characteristics in terms of transformation pathways and achievable stress and strain levels [9-12].

In order to make an adequate comparison with the bulk superelastic behavior of the NiFeGa SMA under compression, we produced micron and sub-micron compression pillars with the diameters between 10 μm and 200 nm using the bulk single crystal of same composition and orientation. The results revealed an increase in the critical stress for the stress-induced martensitic transformation and in the yield stress of martensite with decreasing pillar size. The stress hysteresis also increased with the reduction in pillar size and the superelastic response started to diminish below 500 nm pillar diameter. Two-stage martensitic transformation was suppressed for pillar sizes of 1 μm and below, which exhibited $L2_1$ to $L1_o$ transformation directly. Such change in the transformation path-ways, i.e. transition from a two-stage to one-stage transformation, was also observed in bulk single crystals with increasing temperature. We demonstrated the absence of two-stage transformation in bulk at higher temperatures. This finding suggests that decreasing sample size and increasing temperature have similar effects on the superelastic response of the NiFeGa SMA with two-stage transformation and points out that the reduction in pillar diameter decreases the transformation temperature due to the difficulty of martensite nucleation in small scales.

Our findings for the NiFeGa SMA are expected to bring further insights into the stress-induced martensitic and inter-martensitic phase transformations in sub-micron size scales in order for utilization of SMAs in small scale mechanical devices.

While all the literature in Section 2.1, support the difficulty in martensitic transformation at small length scales, the reasons for suppression of transformation were explained in different ways depending on the geometry and structure of the specimen. A complete understanding on the effects of free surfaces in martensitic transformation and martensite propagation in single crystalline and unconstrained structures still seems to be lacking at very small length scales. Finally, in the present work, we introduced a thermodynamical framework which explains the contributions of elastic and dissipation energies to the martensitic transformation in single crystalline pillars. Our thermodynamical framework gives further insights to the effects of high surface to volume ratio on the nucleation and propagation of martensite in unconstrained structures.

Detailed information for the sample preparation, testing and characterization was given in Chapter III.

4.2 Experimental Results

Transformation temperatures of the NiFeGa bulk single crystals were determined using differential scanning calorimetry (DSC). Martensite start (M_s), martensite finish (M_f), austenite start (A_s) and austenite finish (A_f) temperatures are found to be 3.5, -7, 7 and 14 °C respectively, suggesting that the crystal is completely austenitic at room temperature.

Figure 4.1 shows the bulk compression response of the NiFeGa single crystal along [110] at room temperature. Incremental superelastic response of this bulk crystal

clearly exhibits two-stage transformation. The two-stage transformation for the [110] oriented NiFeGa was previously reported [9, 11, 12]. The parent phase for the NiFeGa has $L2_1$ structure for temperatures lower than about 700 ^oC above which it transforms into B2 structure [61, 62]. The martensitic structures determined for the NiFeGa are 10M, 14M, $L1_o$ and inter-martensitic phase transformations were reported between 10M - 14M and 14M - $L1_o$ [9, 12].

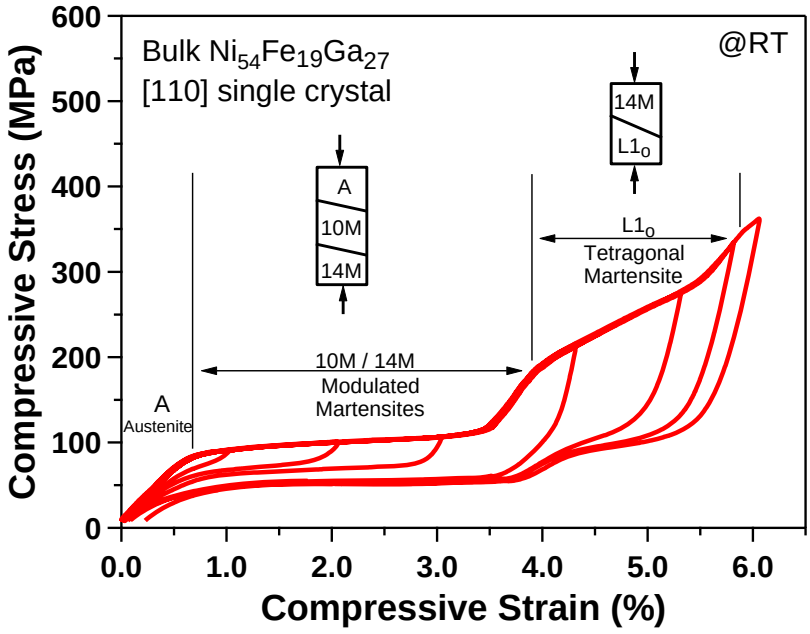

Figure 4.1 Testing of bulk $Ni_{54}Fe_{19}Ga_{27}$ single crystals oriented along the [110] direction at room temperature showing two-stage martensitic transformation.

In Figure 4.1, the NiFeGa has $L2_1$ austenite (A) structure at room temperature [61-65] and under the stress application, it transforms into the first martensitic phase

indicated by the formation of the first plateau region starting at a critical stress (σ_c) of 88 MPa. The first-stage transformation in this case is attributed to $A \rightarrow 10M/14M$ transformation based on the following. The presence of 10M and 14M martensites has been previously reported in the first plateau region under tension at room temperature using the full-field strain measurements [9]. The transformation path was determined to be from austenite to 10M martensite and from 10M to 14M martensite whose coexistence was identified in the first plateau region [9], although was not clearly distinguishable on the stress-strain response as in the present work. Similar transformation path has also been shown under compression [10].

Furthermore, we calculated the theoretical transformation strains for austenite to 10M and 14M martensitic transformations along the [110] orientation in the bulk NiFeGa using the "Energy Minimization Theory" [66-68]. The transformation strains of 10M, 14M and $L1_o$ martensites were determined by considering the twinned martensite which is composed of variant pairs with a certain volume ratio. After finding their respective habit planes and directions, and twinning shear and directions, the transformation strains were quantified [69]. Our theoretical transformation strain calculations for the [110] oriented $Ni_{54}Fe_{27}Ga_{19}$ crystals resulted in 2.44% and 3.0% in compression for the 10M and 14M martensites respectively, thus the experimental transformation strain of about 3% in the first stage indicates the existence of 14M martensite at the end of the plateau region even though 10M to 14M transformation is not distinguishable on the stress-strain response. Considering the study performed by Efstathiou et al. [9], the transformation strains can be measured by local strain

measurements more accurately since the strain measured by an extensometer can be misleading due to averaging the contributions from different martensite plates. Their local strain measurements indicated a combined austenite to 10M and 10M to 14M martensite transformation in the first plateau.

This first stage transformation was followed by the second plateau showing inter-martensitic transformation starting at 196 MPa, which was fully recoverable upon unloading. 14M to detwinned $L1_o$ martensite transformation is responsible from this second stage resulting in a reasonably close strain value to the theoretical detwinned $L1_o$ martensite strain of 6.25%. 14M to $L1_o$ transformation in the second stage was also reported in [9, 12]. Upon unloading, the reverse transformation takes place from the second martensitic phase, $L1_o$, to the modulated martensites which then transform back to austenite leading to fully recoverable superelastic behavior. As seen in Figure 4.1, when further strain is applied, plastic deformation of $L1_o$ starts at around 345 MPa, and after unloading some residual strain remains.

In order to study the size effect during this two-stage phase transformation, micron/sub-micron pillars were prepared using a sample from the same single crystal used in Figure 4.1. Figure 4.2(a) shows the incremental strain superelastic response of a 10 μm pillar including six cycles for which the strain levels were increased in each subsequent cycle. The pillar was deformed to 2% for the first cycle and 7.5% for the sixth cycle. Similar to the bulk response, the micro-pillar showed austenite to 10M martensitic transformation at a critical stress (σ_c) of 135 MPa, followed by 10M to 14M transformation. In the present work, two 10 μm pillars were tested, which exhibited

repeatable transformation stress levels for the first- and the second-stage transformation. Stress-induced martensitic transformation started with a sudden load burst especially for the first three cycles. The first and the third cycles are separately shown in Figure 4.2(b). The load bursts continued through the entire plateau region indicating the motion of austenite-martensite interface. The loading-unloading cycles reveal that up to 5% strain (the black curves), the deformation is fully recoverable during unloading showing the ideal superelastic behavior as seen in the bulk samples (Figure 4.1). Two-stage transformation seems to still exist in this pillar due to fully recoverable deformation reached similar to the bulk behavior. Two transformation regions are distinguishable in the stress-strain plot (shown in Figure 4.2(a)), observed at similar strain levels as in the bulk, prior to the plastic deformation of $L1_o$. The onset of plastic deformation of $L1_o$ (the blue curve) started at around 340 MPa resulting in noticeable residual strain upon unloading. The residual strain accumulated further upon straining to higher levels due to plasticity in martensite. Figure 4.2(c) and (d) show images of this 10 μm pillar before and after deformation respectively. Figure 4.2(d) reveals the martensite twins on the surface formed after the loading-unloading cycles in Figure 4.2(a).

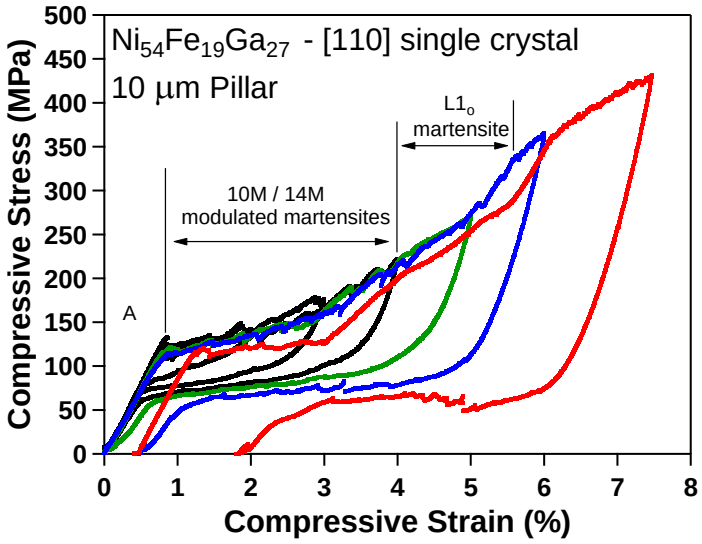

(a)

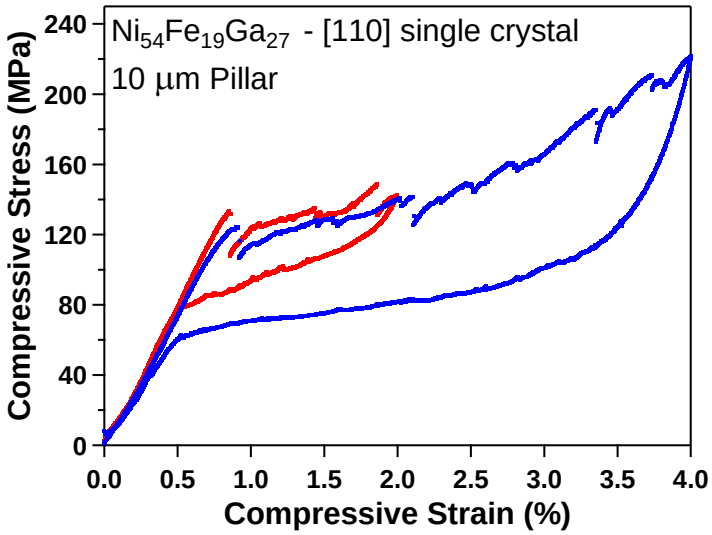

(b)

Figure 4.2 (a) Superelastic response of a 10 μm pillar on the [110] oriented $Ni_{54}Fe_{19}Ga_{27}$ crystal at room temperature. (b) The first and the third straining cycles of the superelastic response shown in (a). (c) SEM picture of the 10 μm pillar in (a) before deformation; and (d) after deformation having 1.8% residual strain upon unloading. The arrow points the twinned surface relieves on the pillar surface.

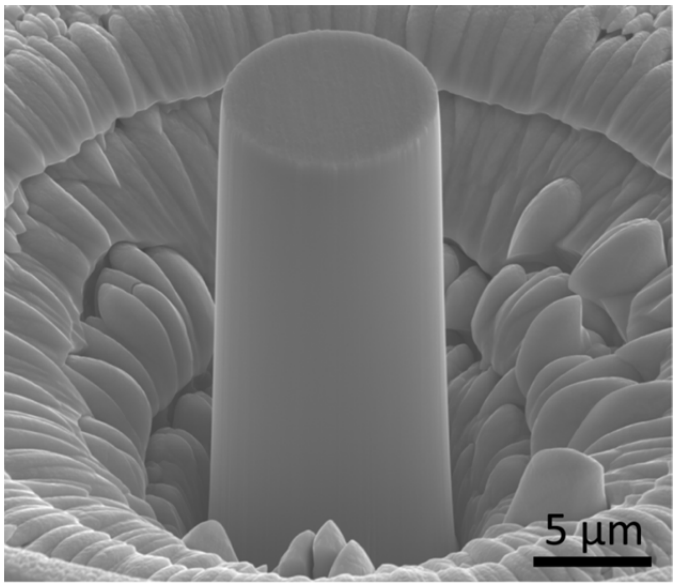

(c)

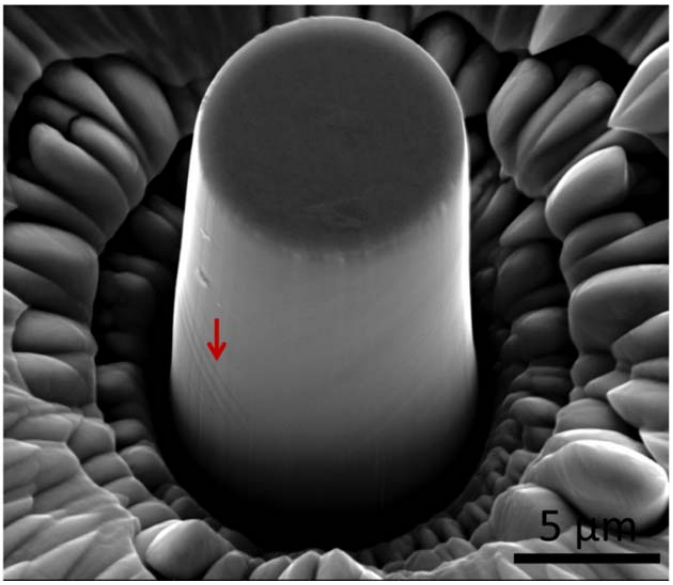

(d)

Figure 4.2 Continued.

A pillar with a diameter of 5 μm was also tested and a similar superelastic behavior with two-stage martensitic transformation at comparable strain levels was observed as shown in Figure 4.3(a). In comparison to the 10 μm pillars, the 5 μm pillar showed slightly higher stress levels for σ_c and for plastic deformation of $L1_o$. Figures 4.3(b) and (c) show images for the 5 μm pillar before and after deformation respectively. There is a small amount of remnant deformation (3.5%) on the pillar after unloading from 9.5% applied strain, and twinning surface relieves on the side surfaces are observed similar to the 10 μm pillar.

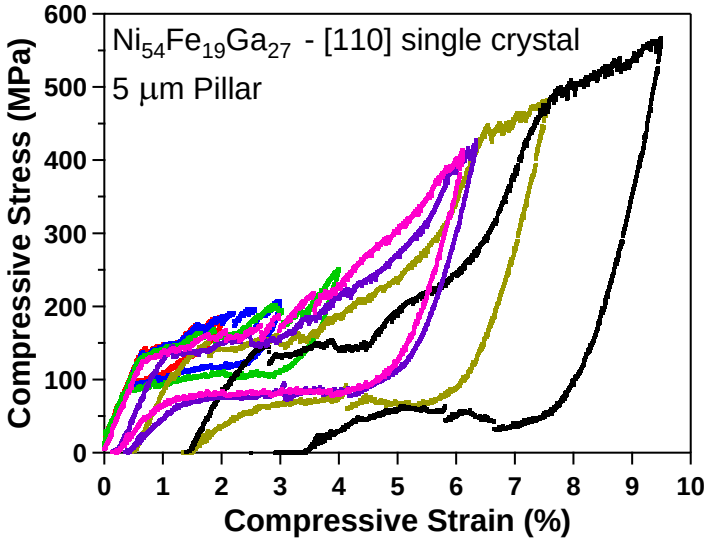

(a)

Figure 4.3 (a) Superelastic response of the 5 μm pillar on the [110] oriented $Ni_{54}Fe_{19}Ga_{27}$ crystal at room temperature. (b) SEM image of the 5 μm pillar in (a) before deformation; and (c) after deformation with 3.5% residual strain. The arrow points the twinned surface relieves on the pillar surface.

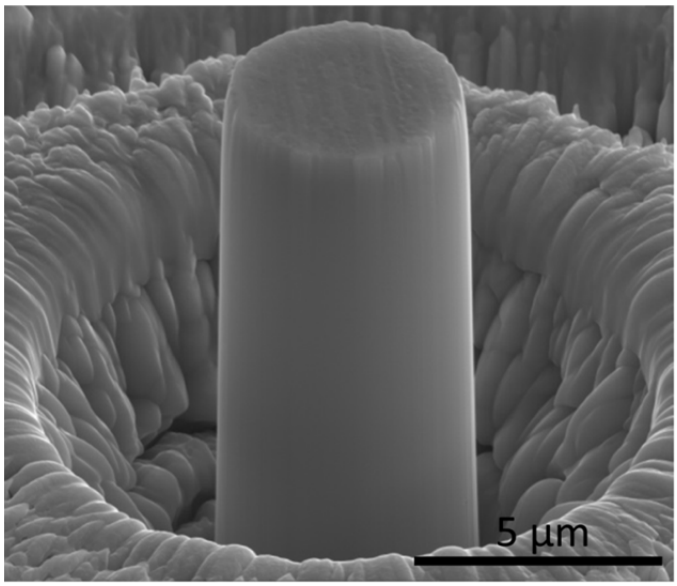

(b)

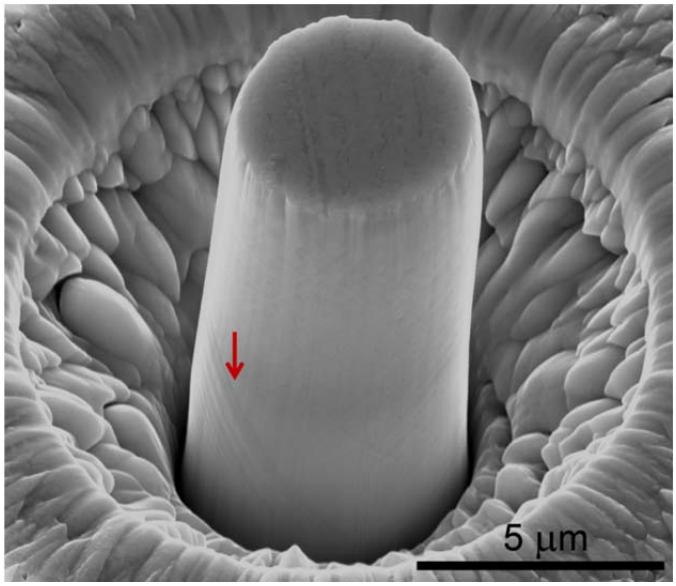

(c)

Figure 4.3 Continued.

Figure 4.4(a) shows the superelastic response of a 1 μm pillar including six straining cycles starting from 2% strain. The σ_c for stress-induced martensite formation is 275 MPa which is much higher than those of 10 μm and 5 μm pillars. Residual strain first appeared during the second cycle after unloading from 3% and more residual strain accumulated upon further straining. From these results, two-stage martensitic transformation seems to be vanished. A single stage martensitic transformation is followed by the plastic deformation of martensite leading to residual strain upon unloading from relatively low strain levels. Even though we do not have direct evidence at the moment, we believe that the single stage transformation occurs between $L2_1$ austenite and $L1_o$ martensite, as discussed in the next section with few indirect proofs. The increase in σ_c for this pillar should be responsible for such change in the transformation path since a similar change is observed in the bulk single crystal upon increase in σ_c via an increase in the testing temperature. In micro and nano compression testing, every significant stress or displacement change can be correlated to an event taking place within the material such as twinning or slip due to sensitivity of micro/nano mechanical testing. Therefore, the first stress drop during the superelastic response of the 1 μm pillar indicated the first stress-induced martensite nucleation. Similarly, large stress drops in bulk single crystals were observed during stress-induced, austenite to $L1_o$ transformation [70, 71]. In this pillar, cubic austenite to tetragonal $L1_o$ martensite transformation resulted in a sudden volume change in the pillar which was accommodated by a large stress burst at the onset of transformation. It is important to note that a possible change in the stress state during the testing of this small scale pillar

should not be the reason in the change in the transformation path here since the non-linear region which may sometimes be seen in the initial portion of the stress-strain plots of micro/nano pillars was minimal in our pillars at this size scale. This suggests the good alignment and contact between the indenter and the pillar. SEM images of the 1 μm pillar before and after deformation are seen in Figures 4.4(b) and (c) where the deformation is visible in the middle section of the pillar.

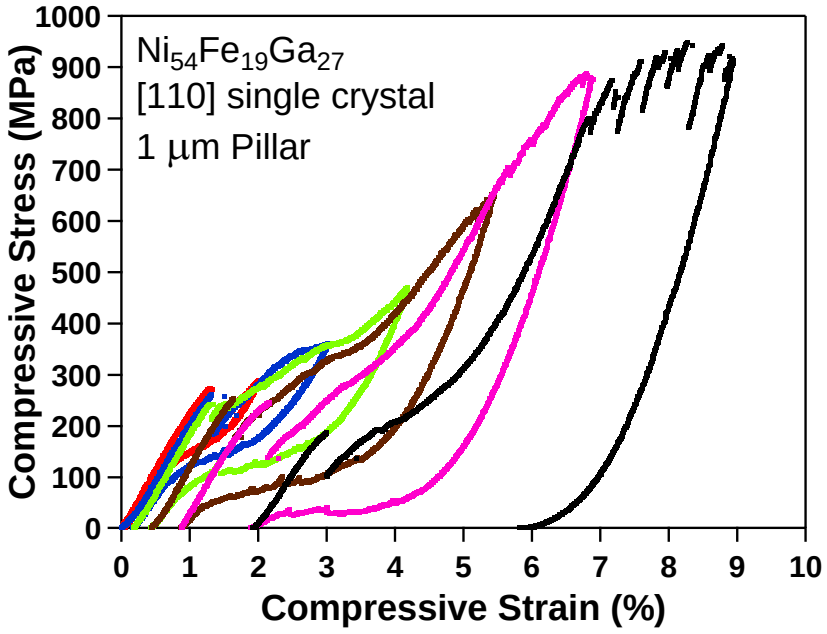

(a)

Figure 4.4 (a) Superelastic response of the 1 μm pillar on the [110] oriented $Ni_{54}Fe_{19}Ga_{27}$ crystal at room temperature. (b) SEM image of the 1 μm pillar in (a) before deformation; and (c) after deformation having 6% residual strain.

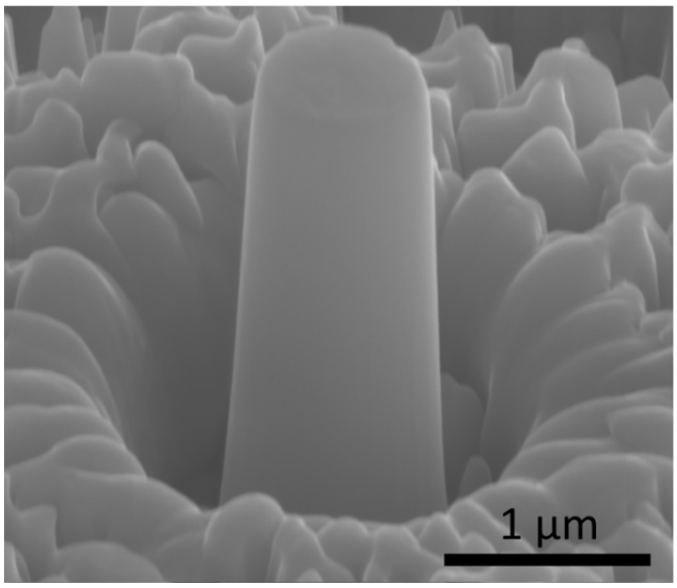

(b)

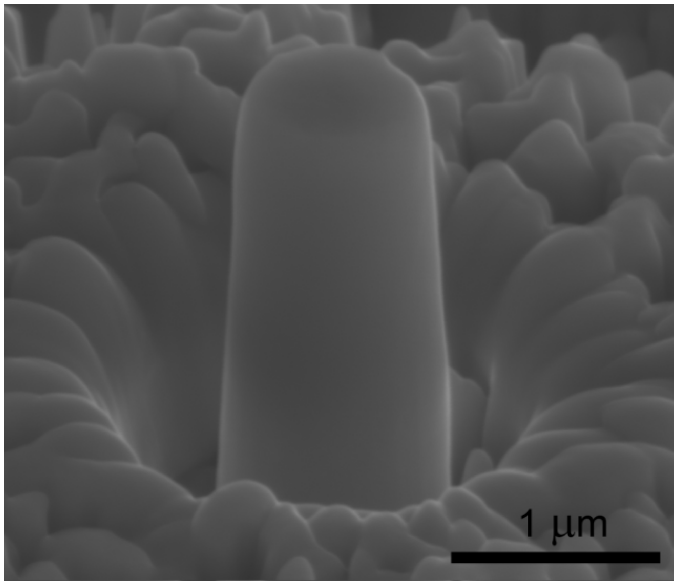

(c)

Figure 4.4 Continued.

A pillar with 585 nm diameter was also tested. It exhibited even higher σ_c for martensitic transformation and less recoverable strain than the 1 μm pillar. The pillar with 420 nm diameter demonstrated the deterioration of the typical superelastic curve shape (Figure 4.5). At such small size scale, the superelastic behavior almost completely vanished with large amount of residual strain left upon unloading in each cycle. For the 420 nm pillar, the onset of phase transformation at 360 MPa seems to be also accompanied by the plastic deformation of austenite and/or martensite phases leading to the loss of superelasticity. The smallest sample studied in this work is the pillar with 235 nm diameter. As seen in Figure 4.6, in this pillar we observed complete loss of superelasticity with a critical stress of 618 MPa at the onset of combined martensitic transformation and plastic deformation. The suppression of superelasticity with sample size was demonstrated for NiTi pillars in a similar size range [27] which is consistent with the results in this work. At this size we suggest that martensitic transformation might still take place as shown for NiTi pillars in similar sizes [43] even though the transformation is not recoverable upon the removal of stress.

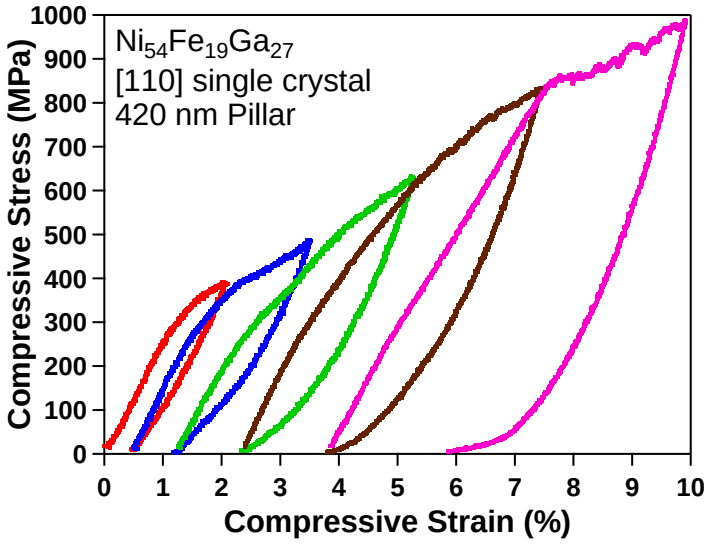

Figure 4.5 Compressive response of the [110] oriented $Ni_{54}Fe_{19}Ga_{27}$ single crystal pillar with 420 nm diameter.

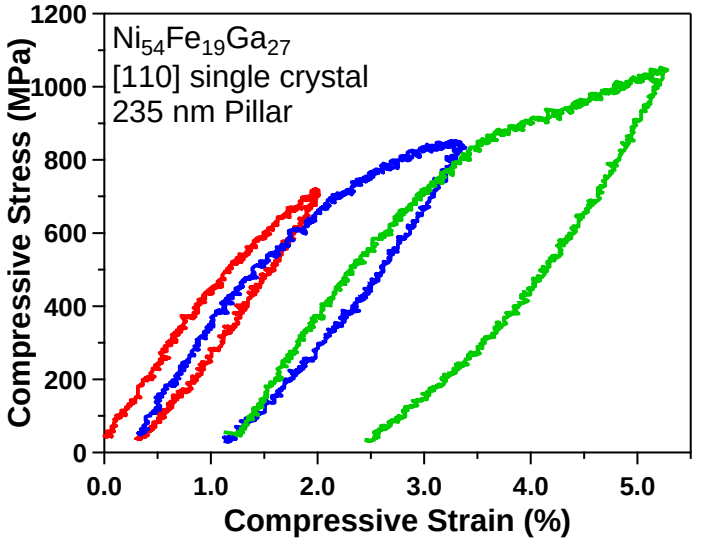

Figure 4.6 Compressive response of the [110] oriented $Ni_{54}Fe_{19}Ga_{27}$ single crystal pillar with 235 nm diameter.

4.3 Discussion

4.3.1 Size Effect in the Stress Required for Martensitic Transformation and Plasticity

It is evident from the superelastic behavior of the [110] oriented $Ni_{54}Fe_{19}Ga_{27}$ bulk crystals and compression pillars with diameters between 10 μm and 235 nm that the critical stress (σ_c) for the onset of martensitic transformation increased as the size of the sample decreased. Increase in σ_c with decreasing size is summarized in Figure 4.7. Bulk sample, 10 μm, 5 μm and 1 μm pillars show distinct critical stresses for austenite to martensite transformation whereas smaller pillars seem to have critical stresses indicative of not only phase transformation but also the onset of plastic deformation caused by local defect generation.

During heterogeneous nucleation of martensite, the probability of martensite nucleation was stated to be higher in larger particles than that of small particles [72]. In the literature, the probability of martensite nucleation was considered as the probability of finding nucleation sites in particles and was investigated by a statistical model based on the assumption that the larger particles include more nucleation sites than smaller particles describing the suppression of martensitic transformation in smaller volumes [44]. Supporting these findings, sub-micron/nano single crystalline pillars were suggested to have less nucleation sites than larger samples which led to an increase in σ_c for stress-induced martensitic transformation [29]. Same rationale was also used to explain suppression of twinning in nanopillars in the absence of dislocations [6]. The present results on the single crystalline NiFeGa pillars support these arguments on the

decrease in the potential nucleation sites with decreasing crystal size and eventually suppression of the martensite nucleation at the pre-existing nucleation sites. With decreasing pillar size, less number of potential internal nucleation sites and surface defects which cause stress concentrations and thus, additional nucleation sites, on the free surfaces of the pillars, seem to be responsible from the increase in σ_c for martensite nucleation. This increase in σ_c leads to an apparent reduction in the martensitic transformation temperature.

Several studies in the literature reported drop of martensitic transformation temperature (M_s) or stabilization of austenite with decreasing crystal size [5, 24, 33, 46, 73-75]. In stress-induced martensitic transformation at a constant temperature, the decrease in M_s temperature leads to an increase in the externally applied stress required for the onset of austenite to martensite transformation. Therefore, increase in σ_c with the reduction in pillar size should correspond to a decrease in transformation temperatures. Similar increases in σ_c with decreasing sample size were also observed in CuNiAl [29] and NiTi [27, 42] pillars.

Plastic deformation of the bulk specimen, 10 μm, 5 μm and 1 μm pillars occurs when $L1_o$ martensite reaches its yield strength. On the other hand, pillars less than 1 μm may involve not only the plastic deformation of $L1_o$ martensite but also the austenite since at high stress levels pillars exhibit residual strains right at the beginning of phase transformation. As seen in Figure 4.7, there is a size dependence of plastic deformation which reveals an increase in the yield stress of martensite with the decreasing size

especially below 10 μm. At 1 μm, the critical stress for the onset of plastic deformation of $L1_o$ showed a significant increase in comparison to those of the larger pillars.

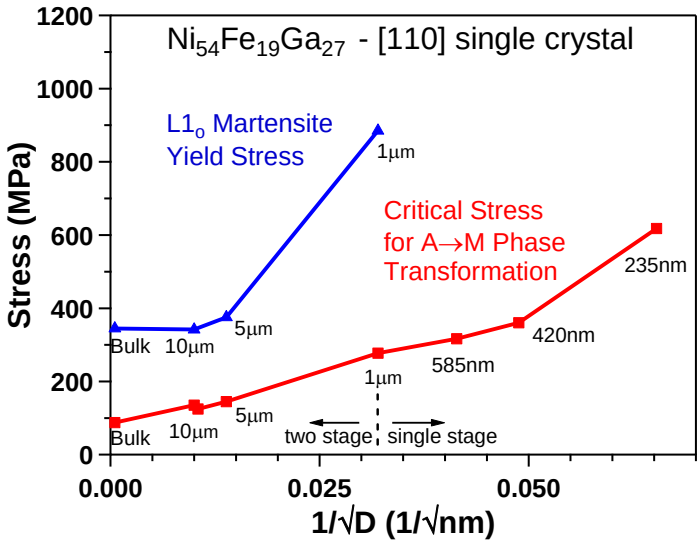

Figure 4.7 The critical stress required for austenite to martensite phase transformation and martensite plastic deformation as a function of size (pillar diameter). A: Austenite, M: Martensite, D: Pillar diameter or bulk compression sample width.

The plastic deformation behavior of the 1 μm pillar is compared with the 10 μm pillar in Figures 4.8(a) and 4.8(b). Although it is not the main focus of the present work, it is imperative to point out that the plastic deformation mechanisms for the 10 μm and 1 μm pillars might be different as a result of the decrease in size. In the 1 μm pillar, deformation twinning seems to be the mechanism for plasticity. The stress drops in the plastic region point out the deformation twinning which acts as a relaxation mechanism

such that we see the plateau region during plastic deformation. At this size scale, the deformation of $L1_o$ martensite seems to involve the nucleation of many fine twins rather than the nucleation of few twins and their propagation. In the 10 μm pillar, even though the large hardening associated with plasticity is an indicative of dislocation plasticity, it should be noted that both stress and strain values are engineering quantities, therefore, hardening rate is somewhat misleading. Additionally, twins appear on the 10 μm pillar surface upon unloading, which is contradictory to the deformation mechanism being dislocation plasticity.

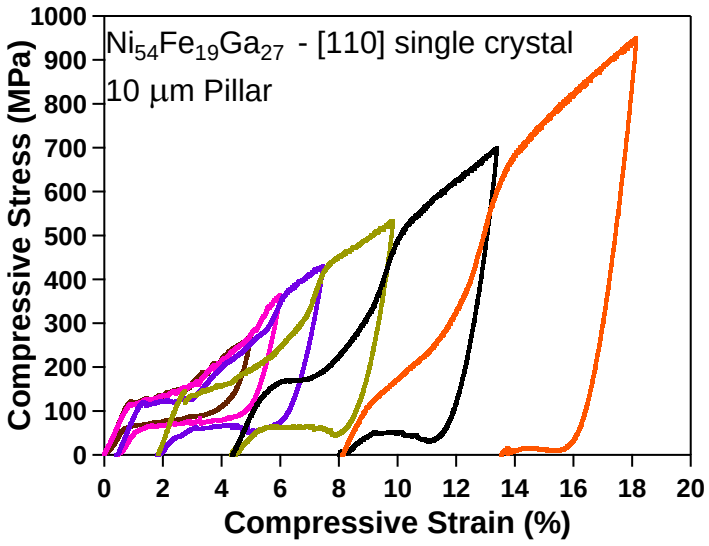

(a)

Figure 4.8 Plastic deformation of $L1_o$ martensite in (a) the 10 μm (b) the 1 μm pillars. The strain cycles for the 1 μm pillar were combined without showing the elastic unloading and loading curves for clarity and each cycle was shown in different color and was separated by solid lines, where they start and end.

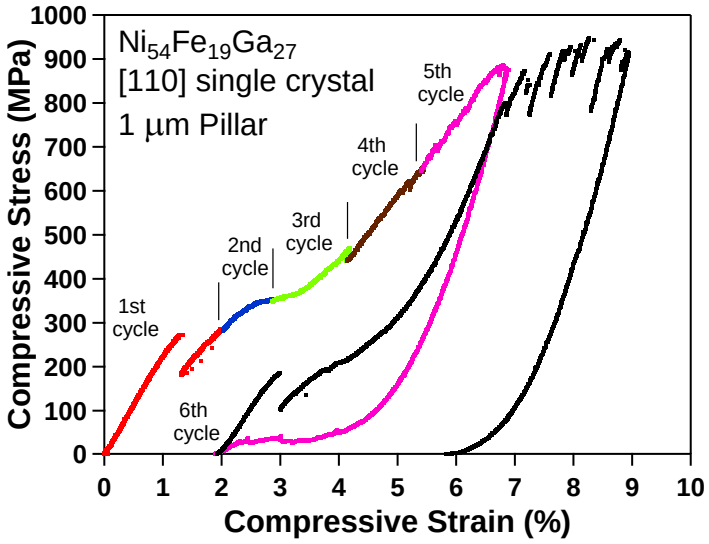

(b)

Figure 4.8 Continued.

When the onset of the plastic deformation is reached in $L1_o$ martensite, the residual strain starts appearing upon unloading. In the pillar images in Figures 4.2(d) and 4.3(c) after unloading from the onset of plasticity in $L1_o$ martensite, twinning surface relieves are seen which may indicate that some of the residual strain can be a consequence of remnant martensite. Another possibility is that the deformation twinning of $L1_o$ martensite takes place during loading and upon unloading reverse transformation of these compound twins in $L1_o$ transforms into twins in austenite. In addition, once the plastic deformation of $L1_o$ is reached in the 10 μm pillar, the unloading curves for each further straining cycle shows similar back transformation stresses in addition to large recoverable strains between 2% and 4%. The presence of the similar reverse

transformation stresses and this much recoverable strains even after the large deformation in the plastic region (up to 18% applied strain) may also indicate the presence of austenite twins. Such mechanism and the large recoverable strains after apparent plastic deformation of were also reported in bulk ultra-fine grained NiTi [76] and bulk single crystalline CoNiAl SMAs [77].

Contrarily to the size dependent plasticity in this work, a size independent plastic deformation of martensite in the [111] oriented NiTi single crystal pillars with precipitates was reported [27, 28]. Similar size independent behavior was observed in the Ni-based oxide-dispersion strengthened alloy micropillars having an internal obstacle spacing smaller than the pillar diameter [78]. In the present work, there are no precipitates that will prevent the surface effects controlling the deformation mechanisms in NiFeGa pillars and significant size effect at the onset of yielding of martensite was observed.

4.3.2 Size Effect in Two-Stage Martensitic Transformation

Two-stage martensitic transformation observed in the [110] oriented NiFeGa bulk crystals was also shown in the 10 μm and 5 μm pillars under compression at room temperature. However, when the diameter of the pillars decreased to 1 μm, according to the superelastic response, the austenite directly transformed to the $L1_o$ martensite. Once the size of the pillar further reduced down 420 nm, superelastic behavior diminished and finally fully suppressed at 235 nm.

To reveal whether such changes in superelastic response are a consequence of the change in the M_s with size and the relative change in the test temperature with respect to the M_s, we conducted superelastic experiments on the bulk crystals at different temperatures. As summarized in the introduction, it is reported in the literature that the reduction of the structural or geometrical size scale, regardless of the dimensionality, leads to a drop in M_s temperature in SMAs. However, there is no report on how scale influences a two-stage martensitic transformation. Figure 4.9(a) shows the bulk compression test results of the NiFeGa oriented along [110] at 30 ^oC and superelastic behavior of the 10 μm pillar along the same orientation at room temperature. The critical stress (indicated by the dashed line) for the austenite to 10M and then to 14M martensite transformation is almost the same for both the bulk crystal at 30 ^oC and the 10 μm pillar at room temperature (~20 ^oC). The shapes of the superelastic curves are also very similar. Figure 4.9(b) shows the superelastic response of the same bulk crystal at 70 ^oC and the 1 μm pillar at room temperature. The critical stresses for austenite to martensite transformation (indicated by the dashed line) are similar for both samples. It is obvious from the 10 μm and 1μm pillars that the increase in the temperature in the bulk has the same effect on the onset of the martensitic transformation as the decrease in the size of the pillars.

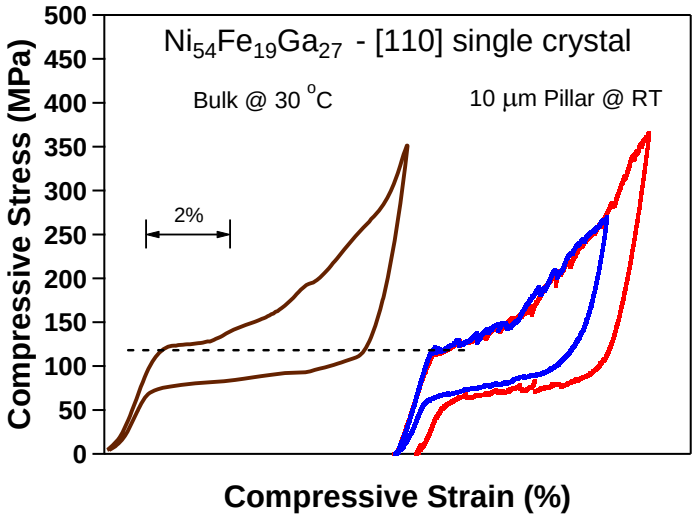

(a)

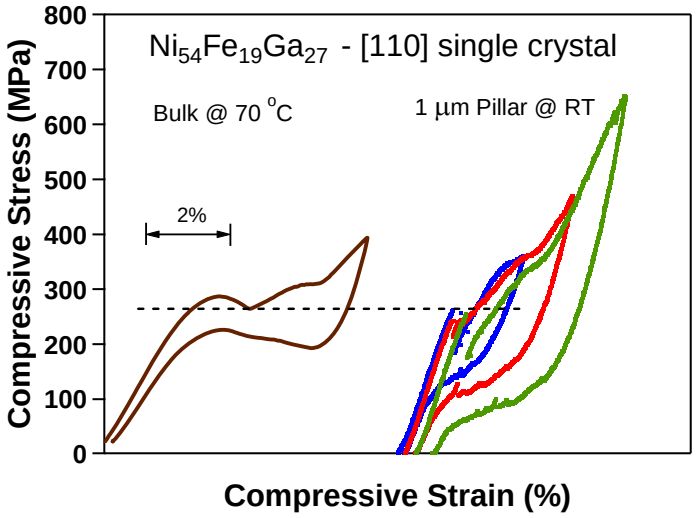

(b)

Figure 4.9 Compressive superelastic response of $Ni_{54}Fe_{19}Ga_{27}$ single crystal oriented along [110]: showing (a) bulk response at 30 °C and the response of the 10 µm pillar at room temperature, (b) the bulk response at 70 °C and the response of the 1 µm pillar at room temperature.

As seen in Figure 4.10, we demonstrated a decrease in transformation strains and increase in the critical stress with increasing temperature in the bulk, which is an indication of the elimination of the modulated martensites and formation of only $L1_o$ martensite. We also conducted load-biased cooling-heating experiments from which a clear transition between a two stage and one stage martensitic transformation at high stresses and high temperatures was observed.

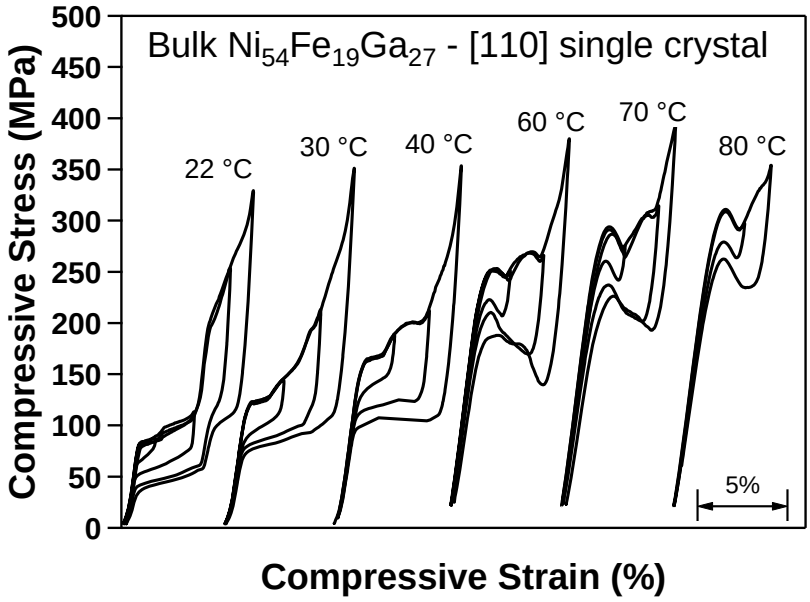

Figure 4.10 Compressive superelastic response of the [110] oriented $Ni_{54}Fe_{19}Ga_{27}$ crystals in bulk tested at 22 ^{o}C, 30 ^{o}C, 40 ^{o}C, 60 ^{o}C, 70 ^{o}C and 80 ^{o}C.

Figure 4.11 summarizes the stress-temperature phase diagram of the bulk $Ni_{54}Fe_{19}Ga_{27}$ oriented along [110] obtained from the superelastic and load-biased cooling-heating tests at different temperatures and stresses, respectively. In this phase diagram, three different regions appear, where the $L2_1$ austenite, the 10M and 14M modulated martensites, and the $L1_o$ non-modulated martensite are stable. It is clear that above 50 ^oC the austenite can directly transform to $L1_o$ martensite whereas below 50 ^oC, the modulated martensites are needed before $L1_o$ formation. As mentioned previously, the 1 μm pillar in the present study has very similar σ_c to the bulk crystal tested at 70 ^oC. Therefore, they are located at almost the same point in the stress-temperature phase diagram where 70 ^oC intersect with 265 MPa for the bulk. Since 70 ^oC is above the temperature required for the transition between two-stage and one-stage transformation, the absence of the $A \rightarrow 10M \rightarrow 14M$ path-way is observed in the stress-strain plots of the 1 μm pillar and the bulk at 70 ^oC. The direct transformation from the austenite to $L1_o$ at 70 ^oC was indicated by the dashed arrow and refers to the transformation path of the 1 μm pillar showing the absence of modulated martensites at this temperature or size range.

Suppression of the inter-martensitic transformation provided less transformation strain than that of the transformation involving modulated martensites. We calculated 3.06% theoretical transformation strain for the [110] oriented $Ni_{54}Fe_{19}Ga_{27}$ under compression. This is somewhat higher than the experimental transformation strain of the 1 μm pillar exhibiting the austenite to $L1_o$ martensite transformation at the first plateau region. However, at this size scale we also start observing deterioration in superelasticity

(Figure 4.12) due to high stress levels reached during straining and thus, generation of local defects at these stress levels. The direct transformation from the austenite to $L1_o$ martensite has been reported in the literature for the same NiFeGa crystals along the ~[105] orientation at 60 ^oC in tension [12] and the [001] orientation at 150 ^oC in compression [10].

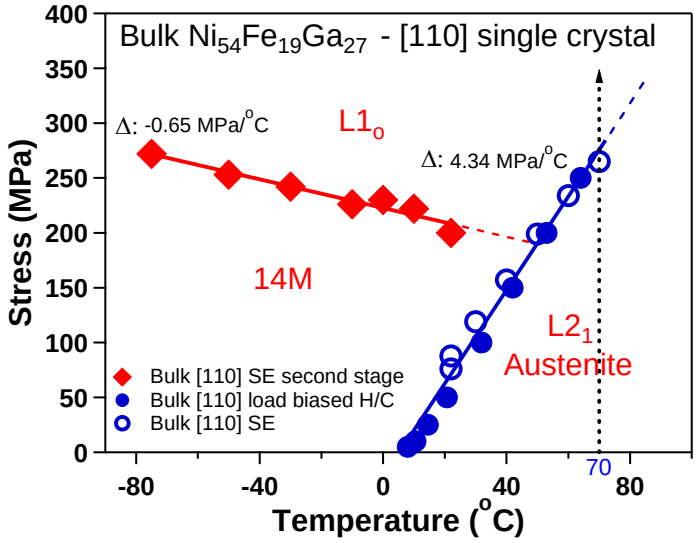

Figure 4.11 Stress versus temperature phase diagram for the bulk $Ni_{54}Fe_{19}Ga_{27}$ oriented along the [110] direction under compression. SE: Superelastic response, H/C: Load-biased heating/cooling response.

Similarities between the small scale pillars at room temperature and the bulk crystals at higher temperatures indicate the drop in M_s with decreasing pillar size. As the pillar size decreases, lower M_s temperatures are expected. As a consequence, the room temperature testing of small pillars with lower M_s gives similar response to the high

temperature testing of the bulk crystal with higher M_s. For example, considering that the Clausius–Clapeyron slope ($d\sigma/dT$) is not size dependent, the M_s temperature of ~40 ^oC can be interpreted for the 1 μm pillar using Figure 4.11. The bulk NiFeGa crystal has an M_s of ~5 ^oC determined using Figure 4.11 and 3.5 ^oC according to the DSC analysis. It is obvious that the testing temperatures of 70 ^oC for the bulk and room temperature for the 1 μm pillar are almost equally above their respective M_s temperatures. In both cases, the large driving force is required to form the martensite due to the large difference between the testing and M_s temperatures, which in turn is observed as an increase in σ_c. Consequently, the decrease in M_s and increase in σ_c is responsible for suppression of two-stage transformation at small length scales. At such high stress level, the cubic austenite is elastically distorted to the level that may transform to the tetragonal $L1_o$ directly without needing accommodation from the monoclinic modulated martensites.

4.3.3 Size Effect in Superelasticity

Size dependence of the superelastic strain is summarized in Figure 4.12 as a function of the applied inelastic strain. Superelastic responses of the bulk sample, and the 10 μm and 5μm pillars along the [110] orientation revealed the complete recovery of applied strain during the incremental straining in the two-stage phase transformation region until the onset of plastic deformation in $L1_o$ martensite. When compared with the bulk, the 10 μm and 5 μm pillars demonstrate inter-martensitic transformation from 14M to $L1_o$ with more hardening, which may originate from the tapered geometry of the pillars and the difficulty of martensite propagation due to the surface effect.

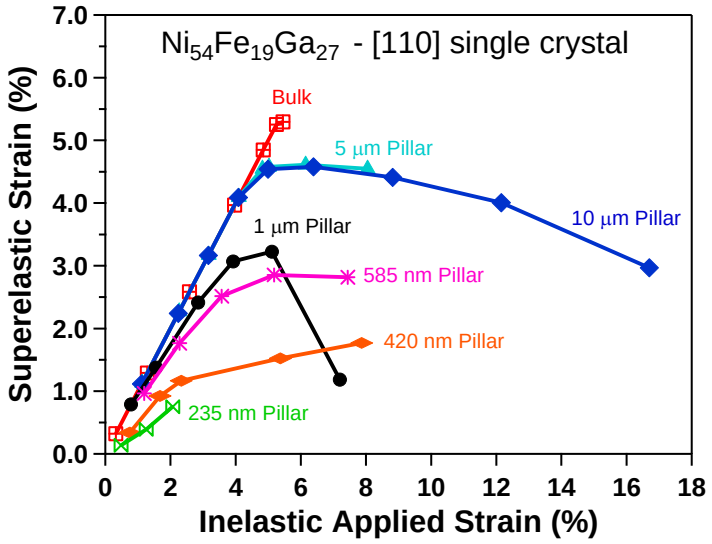

Figure 4.12 Size dependence of superelastic strain in the [110] oriented $Ni_{54}Fe_{19}Ga_{27}$.

When the pillar size is 1 μm, the residual strain starts to appear at 3% total strain (1.56% inelastic strain) as opposed to full recovery of larger samples at much higher strain levels. The residual strains and deterioration of superelasticity were previously reported at similar size scales in NiTi pillars [27]. The smaller transformation strains at these sizes come from the direct transformation of the austenite to $L1_o$ martensite, as discussed in the previous section. The irrecoverability at low strain levels for small size samples, on the other hand, should be due to martensite stabilization and the effect of local defect generation on phase transformation as a result of the increase in the critical stress levels with the reduction in size. Further deformation of this pillar demonstrated a further accumulation of the permanent strain and finally global plastic deformation region of the $L1_o$ martensite (at 885 MPa in Figure 4.8(b)) was reached when more than

5.12% inelastic strain was applied. This plastic deformation region can be clearly seen in Figure 4.8(b) with the large load drops and in Figure 4.12 with the sudden change in the superelastic strain. As the sample size decreased below 1 μm the recoverability also diminished even at lower applied strains due probably to the simultaneous defect generation at the onset of phase transformation, as seen in Figure 4.13, which occurs at significantly higher stress levels in smaller pillars. However, the pillars with 585 nm and 420 nm diameters show more recoverable strains than the 1 μm pillar above the inelastic applied strains of 5.5% and 6.8% respectively. This may be caused by the deformation of the substrate material just beneath the pillar. The significance of this substrate effect has been proven with an in-situ TEM study on NiTi pillars below 200 nm [43]. Supporting our findings above, the loss of superelasticity was also observed in NiTi pillars for which decreasing diameter inhibited superelastic behavior and fully suppressed it below 200 nm [27].

Figure 4.13 shows the superelastic cycles at which the irrecoverability started upon unloading for all sample sizes studied in this work. It is obvious that there is a stress range between 340 MPa and 375 MPa where the residual strain starts to appear for all sizes. This stress range can be an indication of the stress level at which the local defect generation and/or plastic deformation of $L1_o$ martensite starts leading to irrecoverability due to the relaxation of the elastically stored energy upon the defect formation. As explained earlier, increase in the critical stress for austenite to martensite transformation increases as the size of the pillars decrease. In the present work, the critical stress is significantly size dependent whereas the aforementioned stress level for

the local defect generation is size independent. As a consequence, when the sample size is small enough to reach this stress level required for the local defect generation during loading to a certain applied strain level, the residual strain appeared upon unloading.

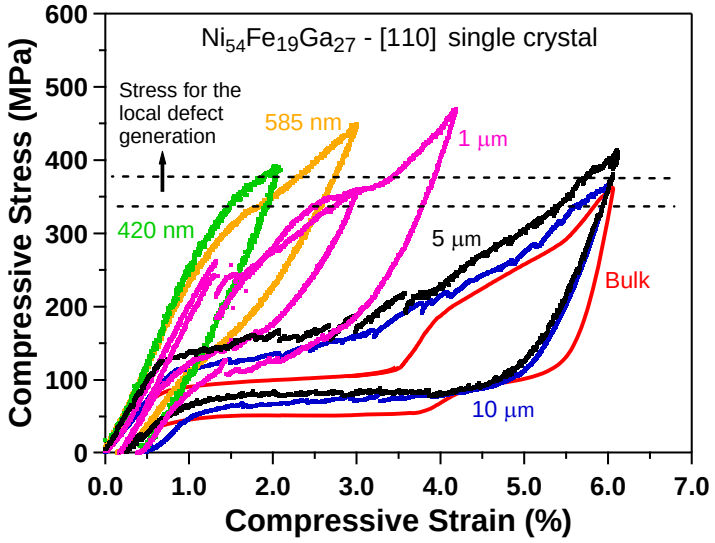

Figure 4.13 Superelastic cycles at which the residual strain starts to appear upon unloading for all sample sizes studied in this work, except the pillar with 235 nm diameter. It is obvious that the residual strain appears when the applied stress level is in the range of 340-375 MPa as indicated by the region between the dashed lines in the figure.

4.3.4 Size Effect in Stress Hysteresis

Stress hysteresis was determined using the stress-strain plots of the different size single crystal samples. Since the bulk single crystal, 10 μm and 5 μm pillars exhibit two-stage transformation, stress hysteresis for the first and second stages were determined separately. For these samples, the first-stage stress hysteresis is identified as the

difference between the stress values of loading and unloading curves at the half length of the first plateau region. First-stage stress-hysteresis values were determined using the straining cycles with the 4% applied strain since the 4% strain included the entire first-stage transformation for all these samples. Second-stage stress hysteresis values were determined at the half length of the second plateau region for the bulk crystal, 10 μm and the 5 μm pillars. For the 1 μm and the smaller pillars stress hysteresis for only one stage is determined due to the suppression of the two-stage transformation. For the 1 μm pillar, the stress hysteresis was determined at the half length of the first plateau using the straining cycle which slightly past the 4% applied strain since it included the entire plateau region. For the 420 nm and 235 nm pillars which show single-stage transformation and plastic deformation at the onset of martensitic transformation, the first straining cycles which past the 4% were used to determine the stress hysteresis to be consistent with the strains used to determine the hysteresis for larger samples. These cycles had 5.2% applied strain for these pillars. In order to be consistent with this strain value, the cycle with the 5.5% applied strain was used for finding the stress hysteresis of the 585 nm pillar. Again, the hysteresis for the 585 nm, 420 nm and 235 nm pillars were determined at the half length of the plateau regions.

Figure 4.14 presents the size dependence of the stress hysteresis for the samples studied in the present work. As seen in the figure, stress hysteresis for the first- and second-stage phase transformations increase with the decrease in the pillar diameter down to 1 μm at which only one-stage transformation takes place with a very large stress hysteresis in comparison with the two-stage transformation hysteresis for larger sizes.

Increase in the stress hysteresis for CuNiAl sub-micron pillars were also reported previously [29]. However, in the present work, the stress hysteresis is not only affected by the size but also the change in transformation paths with the reduction in sample size. Additionally, in NiFeGa pillars, we suggest that the finer twin structure might be present in smaller pillars since it was proposed in the literature that the finer twins form in smaller samples [8]. The formation of finer twins was also shown for the constrained grains of nanocrystalline SMAs [79, 80]. Energy dissipation, and therefore, stress hysteresis, might be increased due to the possible refinement in the twin structure, which is a result of decreasing sample size. More frictional work requirement due to the movement of interfaces in smaller volumes with large surface areas can lead to a larger dissipation, as seen in these pillars.

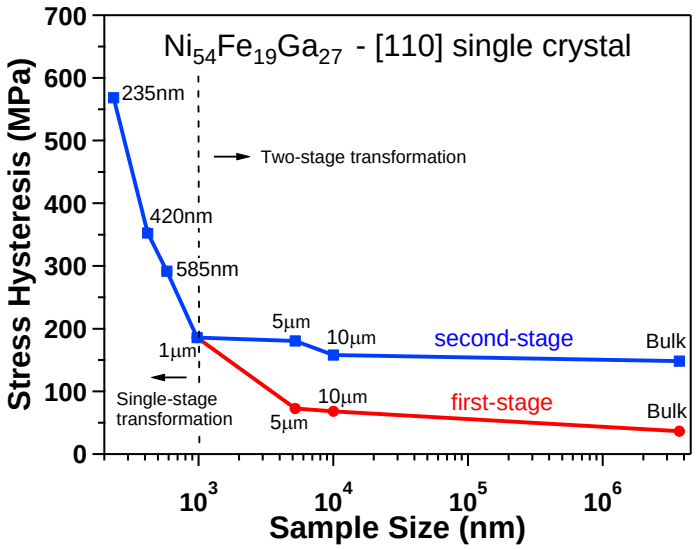

Figure 4.14 Stress hysteresis as a function of sample size for the two-stage and single-stage transformation regions of the stress-induced martensitic transformation in the $Ni_{54}Fe_{19}Ga_{27}$ single crystal pillars oriented along the [110] direction.

The effect of the sample or microstructural size on the hysteresis has been reported in SMAs. In polycrystalline SMAs, there are three length scale factors affecting the hysteresis; the sample size, the grain size and the intrinsic material length (the interface thickness). When the two of these three parameters become comparable to each other, size effect in the hysteresis is observed [81]. This condition is reached when the grain size is very small or very large for a given sample size. For instance, in nanocrystalline SMAs, the stress hysteresis decreases with the grain size. When the grain size is very small, the interface between the austenite and martensite inside a transforming grain becomes comparable to the size of the grain. This leads to a decrease in the stress hysteresis with the reduction in the grain size [81] as shown in nanocrystalline NiTi [82]. On the other hand, in polycrystalline SMAs, when the grain size is large enough to be comparable with the sample size, the system resembles a homogeneous one involving minimal number of grain boundaries. In this system with large grains, the hysteresis decreases when the grain size increases. In between these two regimes for very small and very large grains, the hysteresis is independent of the grain size [81].

Besides the polycrystalline SMAs in which the grain size controlled the stress hysteresis, other systems (microwires and sub-micron pillars) were also studied whose sample size was the controlling parameter determining the stress hysteresis. Increase in the stress hysteresis in CuNiAl microwires with bamboo grain structure was reported for decreasing wire diameters [31]. Since the grains with bamboo structure span across the wire diameter, the controlling size parameter responsible for the increased hysteresis was

the wire diameter. Furthermore, larger stress hysteresis in sub-micron single crystalline CuNiAl pillars was reported than that of their bulk counterpart [29, 30]. These sub-micron pillars showed even larger stress hysteresis than the larger CuNiAl microwires [31]. In single crystalline pillars, the parameter controlling the size effect is the pillar diameter. Therefore, increase in the hysteresis in sub-micron pillars as compared to microwires is consistent and supporting the findings in the present study on the increase in stress hysteresis with the reduction in the pillars size.

Chen et al. reported an existence of a saturation of the increase in the stress hysteresis below the 10 μm sample diameter by combining the results for the CuNiAl pillars of below 2 μm [29, 30] and CuNiAl microwires of above 20 μm [31]. In the present work, we observed a continuous increase in the stress hysteresis with decreasing pillar size also below 10 μm. However, it should be noted that the size effect on the stress hysteresis in NiFeGa pillars, in the present work, is not only related to the decrease in the pillar diameter but also the change in the transformation path with the sample size. Our results indicate that the direct austenite to $L1_o$ martensite transformation in small pillars has higher hysteresis than that of the austenite to modulated martensite transformation in larger pillars.

4.3.5 Thermodynamic Aspects of the Size Effect in NiFeGa Pillars

In this section, we introduce a simple thermodynamical framework on the energetics of martensitic transformation and discuss the effects of size and associated

microstructural factors on individual energy terms. Energy balance for the martensitic transformation can be expressed as

$$\Delta G_{total}^{A\to M} = \Delta H^{A\to M} - T\Delta S^{A\to M} + \Delta E_{el}^{A\to M} + \Delta E_{irr}^{A\to M} \quad (4.1)$$

where $\Delta G_{total}^{A\to M}$ is the total Gibbs free energy difference which needs to be less than zero to trigger the martensitic transformation between Austenite (A) and Martensite (M). In this equation, $\Delta H^{A\to M} - T\Delta S^{A\to M} = \Delta G_{chem}^{A\to M}$ is the chemical free energy difference between A and M phases at temperature T, H and S are the enthalpy and entropy respectively, $\Delta E_{el}^{A\to M}$ is the stored elastic energy upon the transformation, and $\Delta E_{irr}^{A\to M}$ is the energy dissipation during the transformation.

Rearranging the Equation (4.1) by substituting the equilibrium transformation temperature, $T_o = \Delta H^{A\to M}/\Delta S^{A\to M}$, gives the temperatures for the forward (T_{M_s}) and the reverse (T_{M_f}) transformations which can be expressed as [83, 84];

$$T_{M_s} = T_o + \left(\Delta E_{el}^{A\to M} + \Delta E_{irr}^{A\to M}\right)/\Delta S^{A\to M} \quad (4.2)$$

$$T_{A_s} = T_o + \left(\Delta E_{el}^{A\to M} - \Delta E_{irr}^{A\to M}\right)/\Delta S^{A\to M} \quad (4.3)$$

In order to obtain stress dependent expressions for the superelastic response of the pillars in this study we derived Equations (4.4) through (4.7) by substituting ΔS= -$(d\sigma/dT)(\varepsilon_{tr}/\rho)$ in Equations (4.2) and (4.3). In these equations below, σ_{M_s}, σ_{M_f}, $\sigma_{A_s}$and $\sigma_{A_f}$are the stresses at the start and finish of the austenite to martensite transformation and at the start and finish of martensite to austenite reverse transformation, respectively. σ_o is the equilibrium stress and can be found as $\sigma_o = (\sigma_{M_s} + \sigma_{A_f})/2$ for the bulk sample. Here, we assume that ΔS for the forward and

reverse transformations are roughly the same; (i.e., the slopes of stress-temperature phase diagrams are the same). The stored elastic energy and the energy dissipation terms were separated for the nucleation and propagation processes for a better understanding of the transformation at different length scales.

$$\sigma_{M_s=}\sigma_o + (\Delta E_{el}^n + \Delta E_{irr}^n)(\rho/\varepsilon_{tr}) \quad (4.4)$$

$$\sigma_{M_f=}\sigma_{M_s} + \left(\Delta E_{el}^p + \Delta E_{irr}^p\right)(\rho/\varepsilon_{tr}) \quad (4.5)$$

$$\sigma_{A_s=}\sigma_o + (\Delta E_{el}^n - \Delta E_{irr}^n)(\rho/\varepsilon_{tr}) \quad (4.6)$$

$$\sigma_{A_f=}\sigma_{A_s} + \left(\Delta E_{el}^p - \Delta E_{irr}^p\right)(\rho/\varepsilon_{tr}) \quad (4.7)$$

Here, ε_{tr} represents the transformation strain and ρ is the density of the NiFeGa single crystal which is about 8.48 g/cm^3. The contributions of the energy terms during nucleation and propagation were indicated by *n* and *p* respectively. Table 4.1 shows the σ_{M_s}, σ_{M_f}, σ_{A_s}, σ_{A_f} values for the bulk sample, 10 μm and the 1 μm pillars, which were determined using their respective superelastic responses in Figures 4.1, 4.2(a) and 4.4(a) for the first stage transformation. σ_o of 63 MPa determined for the bulk crystal was used for all sample sizes considering that it only changes with the change in the chemical composition similar to T_o.

Table 4.1 Transformation stresses and strains during forward and reverse martensitic transformation for the single crystalline samples with different sizes.

Crystal Size	σ_{M_s}(MPa)	σ_{M_f}(MPa)	σ_{A_s}(MPa)	σ_{A_f}(MPa)	ε_{tr}
Bulk	87.9	115.3	58.9	38	0.03
10 μm Pillar	135.1	180.3	106.3	61.35	0.0316
1 μm Pillar	277.4	367.6	182.5	103.2	0.0285

Using the values of Table 4.1 in the Equations (4.4) through (4.7), we calculated ΔE_{el}^{n}, ΔE_{irr}^{n}, ΔE_{el}^{p} and ΔE_{irr}^{p} for the bulk single crystal and the 10 and 1 μm pillars. The results are listed in Table 4.2. It should be noted that for the bulk and 10 μm pillar samples, these energy terms represent A to 10M/14M martensite transformation while for the 1 μm pillar, they represent A to $L1_o$ transformation.

Table 4.2 Stored elastic energy and energy dissipation contributions to the total free energy change upon martensite nucleation and propagation as a function of sample size.

Crystal Size	ΔE_{el}^{n} (J/g)	ΔE_{irr}^{n} (J/g)	ΔE_{el}^{p} (J/g)	ΔE_{irr}^{p} (J/g)	ΔE_{irr}^{total}(J/g)
Bulk	0.0369	0.0513	0.0117	0.0855	0.1368
10 μm Pillar	0.2151	0.0535	0.00048	0.1681	0.2216
1 μm Pillar	0.5612	0.1595	0.0183	0.2849	0.4444

Elastic stored energy during martensite nucleation, ΔE_{el}^{n}, increases with the decreasing sample size. This indicates that upon nucleation, the stored elastic energy does not relax at the pillar surfaces and more elastic energy is stored in smaller pillars. According to Salzbrenner and Cohen [85], when martensite nucleates at the free corner or edge of a specimen, elastic energy is not stored during nucleation. Our findings here reveal that the stored elastic energy during martensite nucleation increases as the sample size decreases. This is an indirect indication that the martensite nucleates inside the pillars rather than the free surfaces.

As discussed earlier, M_s temperature decreases with the pillar size in the present NiFeGa crystals. The increase in the stored elastic energy during the nucleation without relaxation at pillar surfaces with decreasing pillar size is one of the reasons for the reduction in M_s temperature.

In smaller sample sizes, there are less number of nucleation sites, compared to that of the larger samples, leading to more difficult nucleation and in turn, to a lower M_s temperature. The large increase in ΔE_{el}^{n} between 10 μm and 1 μm pillars also indicates the influence of nucleating a modulated vs. a non-modulated martensite as the transformation pathway changes in the 1 μm pillar.

Elastic stored energy during martensite propagation, ΔE_{el}^{p}, does not follow the same trend as the ΔE_{el}^{n}. Bulk single crystal and the 1 μm pillar have very close stored elastic energies during propagation. Comparing the elastic energies of the bulk sample and the pillars during propagation may lead to a misleading discussion since pillars have a slight taper that will contribute to their hardening behavior during martensitic

transformation. When the 10 μm and the 1 μm pillars are compared, a significant increase in the stored elastic energy during propagation is realized. In addition, in their superelastic responses, more hardening is observed in the 1 μm pillar than that of the 10 μm pillar. As seen in Figure 4.13, this much hardening difference between the 10 μm and the 1 μm pillars cannot be only coming from their taper difference. We argue that this hardening and the increase in the stored elastic energy mostly comes from the difficulty in the martensite propagation in the smaller pillars leading to a larger transformation range such as large M_s-M_f or σ_s-σ_f. The large transformation ranges were reported for the fine grained SMAs [85].

ΔE_{irr}^{total} represents the sum of the frictional energy dissipation during nucleation and propagation. In Table 4.2, significant increase in the energy dissipation is observed with the decreasing crystal size. The dissipation occurs due to the generation of defects and dislocations, and the movement of phase fronts causing frictional losses. The frictional dissipation seems to have a significant effect in the superelastic response of the pillars which appears as the increase in stress hysteresis in Figure 4.14. As the pillar size gets smaller, more dissipation occurs during the movement of interfaces due to a larger surface to volume ratio in the smaller pillars. In the NiFeGa pillars, in the present work, the change in the two-stage martensitic transformation into one-stage transformation at the 1 μm size scale also affects the observed increase in the total frictional energy dissipation. More frictional losses leading to a larger hysteresis are observed during the austenite to $L1_o$ martensite transformation in the 1 μm pillar than the austenite to 10M/14M martensite transformation in the larger samples. When the energy dissipation

is compared during the nucleation of martensite in different size samples, it is observed that the tetragonal $L1_o$ martensite causes more energy dissipation as given by the ΔE_{irr}^{n} for the 1 μm pillar in Table 4.2. Additionally, more frictional losses occur during the propagation of the $L1_o$ martensite (ΔE_{irr}^{p}) in the 1 μm pillar. This should be due to the martensite propagation taking place in a pillar with a larger surface to volume ratio. Furthermore, we mentioned about the possible refinement in the twin structure in the small pillars, such as in the 1 μm pillar earlier. Presence of such microstructure should also have an effect on the large energy dissipation during martensite propagation due to larger surface area provided by fine twins and resulting large friction at the phase fronts between the austenite and martensite.

4.4 Summary and Conclusions

In the present work, the effects of the sample size scale on the superelasticity during a two-stage martensitic transformation were investigated in $Ni_{54}Fe_{19}Ga_{27}$ single crystals oriented along the [110] direction. The bulk crystals have been tested between 22 ^{o}C and 80 ^{o}C and micron/sub-micron compression pillars with sizes ranging from 10 μm to 235 nm were deformed at room temperature. The main findings and conclusions can be summarized as follows;

- 10 μm and 5 μm pillars demonstrated a two-stage martensitic transformation, similar to the bulk single crystals from austenite to 10M/14M modulated martensite for the first stage and to $L1_o$ martensite for the second stage. The reduction in the pillar size led to an increase in the critical stress for martensitic

transformation, similar to the conventional SMAs with single stage martensitic transformation.

- Further reduction in the pillar size down to 1 μm and below, and the associated increase in the critical stress for the first stage transformation resulted in a change in the transformation path. The new transformation path involved the direct transformation of austenite to $L1_o$ martensite.
- Since increase in the critical stress for the transformation is thermodynamically equivalent to reduction in M_s temperature, smaller sample sizes caused an increase in the difference between the test temperature and effective M_s. To achieve the same thermodynamic conditions in the bulk crystals and have more meaningful comparison with smaller pillars, higher superelastic test temperatures were utilized on bulk crystals, extending the gap between the test temperature and the M_s. The higher temperatures resulted in the higher critical stresses for the transformation, as expected, and at the same time, changed the transformation path to the single stage transformation as in the case of the pillar sizes below 1 μm. Clearly, the reduction in the sample size has a similar effect on superelastic response of SMAs as increasing test temperature in the bulk sample, pointing out the similar governing microstructural mechanisms.
- Residual strains started to appear at lower applied strain levels with decreasing pillar size. It was found that there exist a stress range (340 MPa to 375 MPa) where if the applied strain level is sufficient to reach at, then upon unloading from this stress range, the residual strain appeared for the first time, regardless of

the pillar size. We argued that this stress range is the indication of the stress level for the local defect generation in $L1_o$ martensite, which is apparently, size independent. Because of the increase in the critical stress for martensitic transformation and smaller transformation strain required to reach this stress range, the reduction in the pillar size led to the suppression and eventually the complete loss of superelasticity.

- Stress hysteresis at the first plateau region of the different pillar sizes increased as the pillar size decreased. Such increase in the hysteresis is not only a consequence of the decreasing sample size but also a result of the effect of decreasing size on the transformation path. Bulk crystal, 10 μm and 5 μm pillars with two-stage martensitic transformation possessed relatively narrow stress hysteresis at the first stage of transformation, which originally increased with sample size reduction. In the 1 μm and the smaller pillars, showing only one stage martensitic transformation, the stress hysteresis significantly increased as the size decreased. These results reveal that the NiFeGa pillars exhibit an increase in the stress hysteresis due to more energy dissipation in the smaller samples as well as the larger hysteresis required for the austenite to $L1_o$ martensite transformation
- Size effects observed in the present work, such as the increase in the critical stress required for the martensitic transformation and the increase in the stress hysteresis with the decreasing sample size, were discussed by investigating the change in the thermodynamic energy terms with size. The stored elastic energy

and the energy dissipation were calculated for the bulk sample, 10 μm and the 1 μm pillars upon martensite nucleation and propagation. The increase in the stored elastic energy during martensite nucleation seems to be responsible for the increase in the critical stress and thus, the drop in the M_s temperature with the decrease in the sample size. The increase in the stress hysteresis is due to the increase in the energy dissipation as the sample size gets smaller. The energy dissipation is not only increases due to the decrease in the pillar size but also due to the change in the transformation path with the reduction in the sample size.

CHAPTER V

SIZE EFFECTS IN MAGNETIC FIELD-INDUCED MARTENSITE REORIENTATION IN $Ni_{50}Mn_{28.3}Ga_{21.7}$ FERROMAGNETIC SHAPE MEMORY ALLOYS

5.1 Introduction

$Ni_{50}Mn_{28.3}Ga_{21.7}$ single crystals oriented along the [100] direction of austenite was selected to study size effects in martensite variant reorientation in FSMAs due to high reversible strain levels along this orientation. This crystal is martensitic at room temperature, which is not a single crystal since it is composed of twins. First of all, the compression experiments were performed on the $Ni_{50}Mn_{28.3}Ga_{21.7}$ bulk specimen and then the compression pillars with diameters ranging between 20 μm to 630 nm were tested. After testing, magnetic field was applied to the pillars in the direction perpendicular to compression axis to investigate the size dependence of recovery due to magnetic field-induced martensite reorientation. Application of magnetic field perpendicular to the compression axis is required in order to reorient stress-favored variants into magnetically-favored ones leading to a shape change. The details of the sample preparation, testing and characterization are mentioned in Chapter III.

With this systematic study, the size dependence of stress- and magnetic field-induced martensite reorientation was investigated. The factors responsible for the observed size dependence were discussed. The results revealed that the martensite

reorientation stress is size dependent as it increases with the decreasing sample size. The magnetic field required to recover the pillars also increased with decreasing sample size. In this study, the magnetic field levels required to start the recovery of the pillars were between 2T and 5T. It was surprising to observe the shape change of the pillars at this magnetic field level higher than the saturation magnetic field of the bulk single crystal. These findings led us to make our major conclusion that the magneto-crystalline anisotropy energy (MAE) increases with the reduction in sample size which has not been shown in the literature previously, either directly or indirectly.

5.2 Martensite Variant Reorientation/Detwinning in Bulk $Ni_{50}Mn_{28.3}Ga_{21.7}$

Figure 5.1 shows compression test for the bulk $Ni_{50}Mn_{28.3}Ga_{21.7}$ oriented along the [100] direction of the austenite phase. This single crystal is martensitic at room temperature and the test in Figure 5.1 was performed at room temperature to compare the martensite reorientation stress of the bulk with the pillars. In the stress-strain response of the martensite deformation, reaching a plateau region indicates reorientation of martensite by twin boundary motion. During loading, one martensite variant grows at the expense of others until the sample becomes a single variant martensite at the end of the plateau region where this single martensite variant starts to deform elastically. Upon unloading, the amount of deformation, except the elastic deformation, put on the specimen remains. As seen in the figure, the martensite reorientation stress (σ_r) is around 1.5 MPa which is the stress level of the plateau region. In this specimen there is 4.4% deformation left upon unloading, indicating the presence of the 10M martensitic

structure in this $Ni_{50}Mn_{28.3}Ga_{21.7}$ bulk sample [86]. After testing, the deformation was recovered by the application of a magnetic field less than 0.8 Tesla. This bulk sample saturates at 0.8 T as shown in Figure 5.2 meaning there is no twin boundary motion above this field level. This NiMnGa martensitic sample along the same orientation was used to prepare the micron/sub-micron pillars to study the size effects.

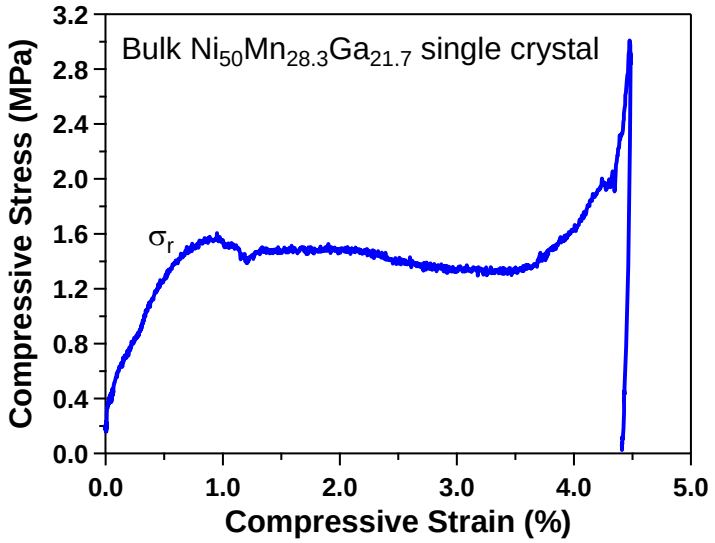

Figure 5.1 Compression test on the bulk $Ni_{50}Mn_{28.3}Ga_{21.7}$ oriented along the [100] direction showing martensite reorientation at ~1.5 MPa. σ_r refers to the stress required for martensite reorientation/twinning.

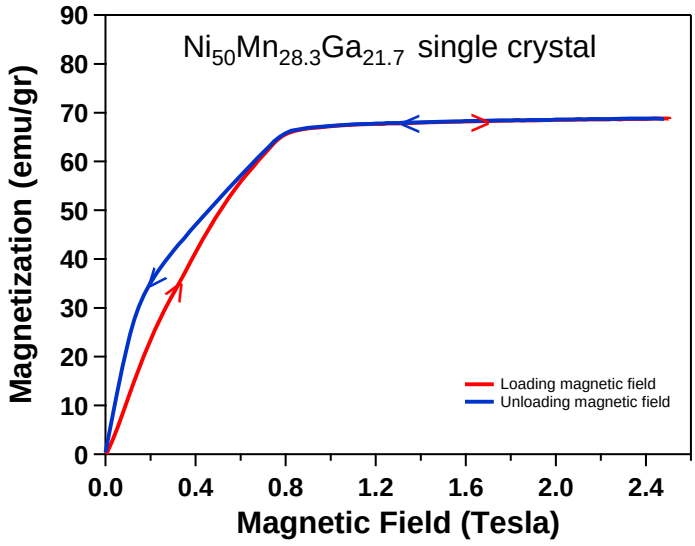

Figure 5.2 Magnetic field versus magnetization plot of the bulk $Ni_{50}Mn_{28.3}Ga_{21.7}$ single crystal showing 0.8 T saturation magnetic field.

5.3 Martensite Variant Reorientation/Detwinning in $Ni_{50}Mn_{28.3}Ga_{21.7}$ Micron/Sub-micron Compression Pillars

5.3.1 Stress-induced Martensite Variant Reorientation in $Ni_{50}Mn_{28.3}Ga_{21.7}$ Pillars

In order to determine how the martensite reorientation stress is affected by decreasing sample size, micron/sub-micron pillars were machined on the magnetically favored twin of the bulk sample. Magnetically favored twin was selected for the pillar preparation in this part of the study because the magnetically-favored twin formed as a result of the application of the magnetic field and thus can be oriented again under stress. To investigate martensite variant reorientation due twin boundary motion at small length scales, pillars having diameters of 20 μm, 10 μm and 5 μm were fabricated and tested

under compression. Since all of these pillars were machined inside a large twin, their initial condition is expected to be a single variant martensite.

The 20 μm pillar and its surrounding are shown in Figure 5.3(a). As seen in Figure 5.3(b), the 20 μm pillar showed around 10 MPa martensite reorientation/twinning stress indicated by the first plateau region and is larger than the 1.5 MPa twinning stress of its bulk counterpart. It is evident that the martensite reorientation became more difficult when the size was decreased to 20 μm. When the single variant martensite pillar was loaded under compression, first the martensite is elastically deformed and then the stress-favored martensite variant nucleated with a large stress drop at 16 MPa as seen in Figure 5.3(b). Since the compression test was carried out in a displacement controlled mode, this sudden stress drop accommodated the large displacement generated due to the formation of the stress-favored martensite twin. Martensite variant reorientation is the rotation of the unit cells under stress. Initially, the magnetically-favored twin of the NiMnGa single crystal is composed of the tetragonal unit cells having their long axis (a-axis) oriented along the compression axis of the pillars. When the pillar is loaded, these unit cells rotate by 90 ^{o}, making the short axis of the tetragonal unit cells (c-axis) parallel to the compression direction and thus stress-favored twin is formed. The stress-strain plot in Figure 5.3(b) shows the direction of the unit cells before and after deformation.

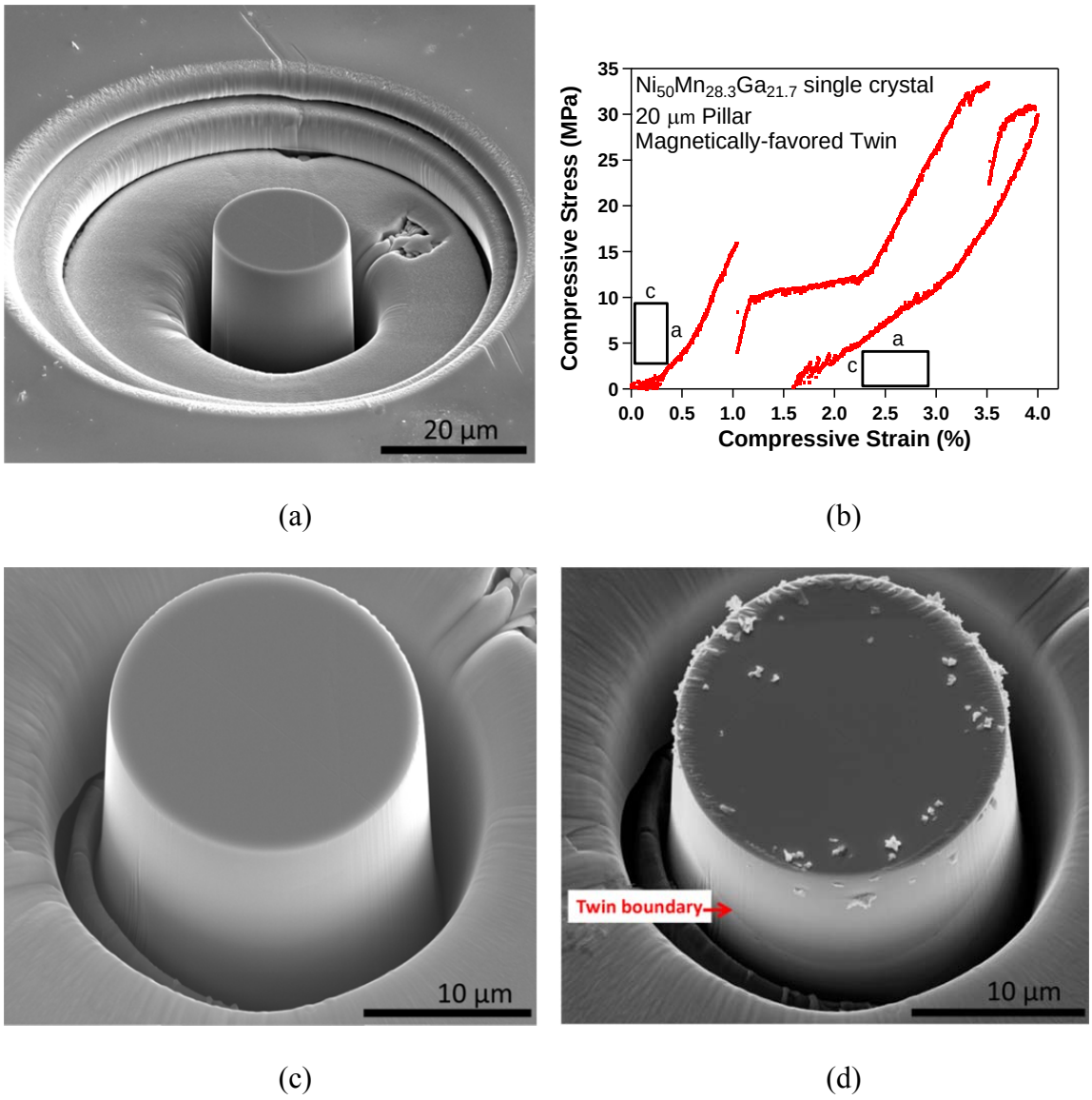

Figure 5.3 (a) SEM image of the $Ni_{50}Mn_{28.3}Ga_{21.7}$ pillar with the diameter of 20 µm and its surrounding trench. (b) Stress-strain plot of the 20 µm pillar showing martensite reorientation response. The tetragonal unit cell was drawn in the plot to show its orientation before and after the deformation. SEM image of the 20 µm pillar, (c) before deformation, and, (d) after deformation showing the twin boundary between the stress-favored and the magnetically-favored twins.

The new twin boundary between the magnetically-favored and stress-favored twins propagated at a lower plateau stress level than the stress required to nucleate the stress-favored martensite twin. This is due to the difficulty in nucleation of another twin at this size scale since the pillar is a single crystal made of only one twin variant with no pre-existing twin boundaries. Once the second twin forms under stress, the martensite reorientation takes place easily at a lower stress level by the twin boundary motion throughout the pillar length. After its propagation, the stress-induced martensite started to deform elastically at the end of the first plateau region.

Upon more loading, the 20 μm pillar reached another plateau region at around 32 MPa. This plateau seems to be caused by the material beneath the pillar. The SEM images of this pillar taken before and after deformation were shown in Figures 5.3(c) and (d) respectively. During loading the twin boundary reached the bottom of the pillar where it is attached to its substrate material. This suggests that the second plateau represents the stress-induced martensite formation in the pillar substrate. The sudden stress drop at 33.4 MPa is because of the formation of a large displacement due to the stress-induced twin nucleation in the substrate. Since the material underneath the pillar has a larger cross-section than the pillar diameter, a higher stress level was calculated by using the pillar diameter for the twin formation in the substrate. Upon unloading, 2.4% deformation was recovered as seen in Figure 5.3(b). This can be caused by the movement of the stress-favored twin in the substrate material towards the pillar during unloading. The recoverable strain observed upon unloading in a 10 μm x 15 μm x 30 μm

NiMnGa pillar was explained by the movement of the martensite twins between the pillar and its substrate material [51].

Figure 5.4(a) shows the 10 μm pillar and the opening surrounding it. This pillar was tested under compression and the resulting stress-strain plot is presented in Figure 5.4(b). The pillar seems to be a single variant martensite as no twin boundaries are observed in its SEM image taken before deformation in Figure 5.4(c). Since the pillar was machined in a magnetically-favored twin of the NiMnGa sample, it is composed of the tetragonal unit cells which have their long axis oriented along the compression axis. When the pillar is compressed, these unit cells rotate by 90^{o} and form the stress-favored twin variant as sketched in the stress-strain plot in Figure 5.4(b). It seems like the martensite propagation became more difficult at the 10 μm length scale due to the surface effects. Instead of a single twin nucleation and its propagation, several twin boundaries were seen on the pillar surface after deformation as shown in Figure 5.4(d). During loading, the stress-favored martensite nucleation and propagation took place between 18 and 21.5 MPa which is a higher stress level than what was required for the 20 μm pillar as discussed above. In this 10 μm pillar, the stress-favored martensite propagated almost throughout the entire pillar length but did not extend into the pillar substrate as indicated by the twin boundary towards the bottom part of the pillar in Figure 5.4(d). Therefore, the stress-strain plot in Figure 5.4(b) is the response of only the 10 μm pillar with no bulk material effect coming from underneath the pillar.

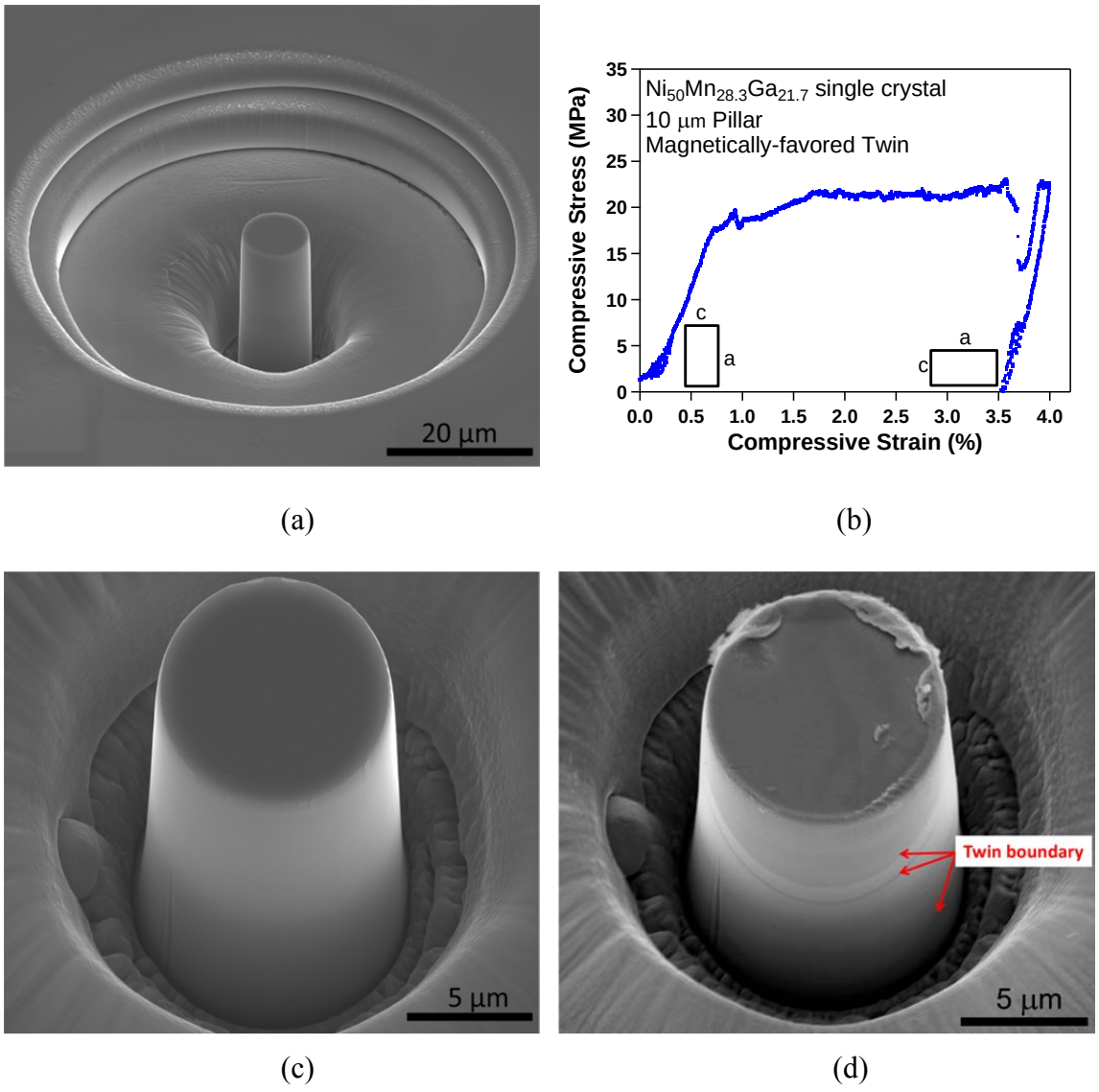

Figure 5.4 (a) SEM image of the $Ni_{50}Mn_{28.3}Ga_{21.7}$ pillar with the diameter of 10 µm and its surrounding opening. (b) Stress-strain plot of the 10 µm pillar showing martensite reorientation response. The tetragonal unit cell was drawn in the plot to show its orientation before and after the deformation. SEM image of the 10 µm pillar, (c) before deformation, and, (d) after deformation showing the twin boundaries between the stress-favored and the magnetically-favored twins.

Figure 5.5(a) shows the 5 μm pillar machined on the magnetically-favored twin of the NiMnGa bulk sample and the pillar surrounding. The compressive test performed on this pillar in Figure 5.5(b) clearly shows a higher stress level of around 40 MPa required for martensite reorientation. As seen in Figure 5.5(c), this pillar seems to be a single martensite variant with no pre-existing twin boundaries. As the previous NiMnGa pillars, this pillar was machined in the magnetically-favored twin. Upon loading, the martensite variants composed of the tetragonal unit cells, rotated to align their short axis with the compression direction and thus formed the stress-favored twin variants similar with the previous pillars above.

There is something that should be taken into consideration when interpreting the stress-strain response of this 5 μm pillar. In Figure 5.5(b), we see the typical contact/release noise of the nanoindenter, in addition to ringing in the displacement at the 1.5% strain where the stress drop occurred due to martensite reorientation. The nanoindenter in this case had a sudden perturbation due resulting change in the displacement (shape change) and the control loop was not able to keep up with it. The magnitude of this ringing is about 65 nm (0.5% strain). With the nanoindenter being this unstable, the stress level we get from about 1.5% to 2.5% strain should not be trusted until the machine re-stabilized at the 2.5% strain. For this sample, the loads are at the extreme low end of the capacity of the load cell and the nanoindenter has a hard time controlling the displacement when the loads are so low.

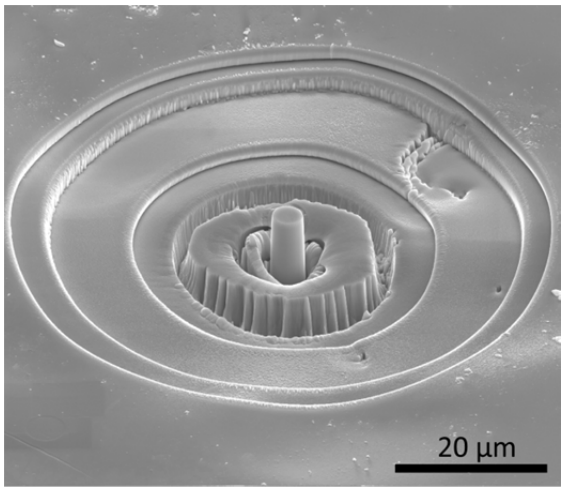

(a)

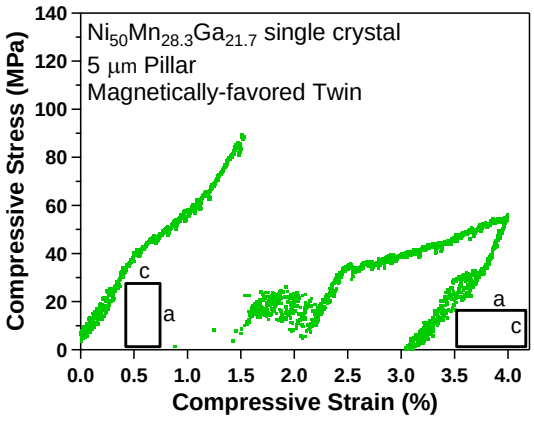

(b)

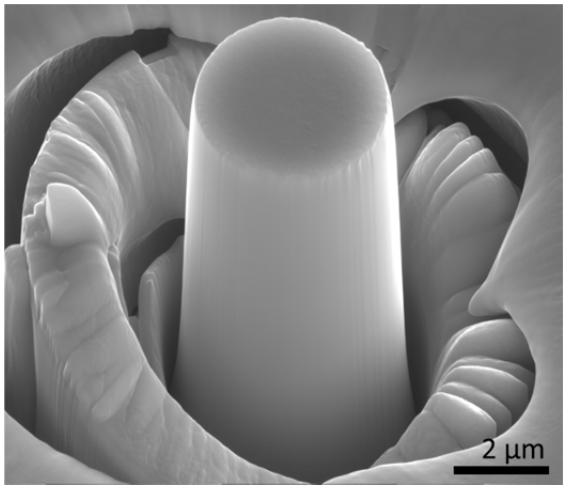

(c)

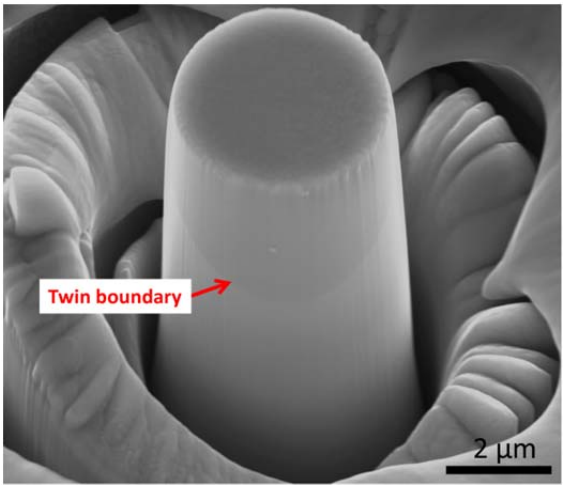

(d)

Figure 5.5 SEM image of the $Ni_{50}Mn_{28.3}Ga_{21.7}$ pillar with the diameter of 5 µm and its surrounding trench. (b) Stress-strain plot of the 5 µm pillar showing martensite reorientation response. The tetragonal unit cell was drawn in the plot to show its orientation before and after the deformation. SEM image of the 5 µm pillar, (c) before deformation, and, (d) after deformation showing the twin boundary between the stress-favored and the magnetically-favored twins.

The elastic modulus of the 5 μm pillar is also slightly different than the previous larger pillars because a very good contact with this pillar was not made until about 160 nm of displacement (1.2% strain). However, it is clear from the after deformation SEM picture in Figure 5.5(d) that there is no bending in this pillar meaning it finally reached the complete alignment after 1.2% strain. With these explanations, we conclude that at the peak stress level of around 90 MPa, a sudden displacement change took place due to the martensite reorientation and the newly formed stress-favored martensite twin propagated throughout the pillar length. The propagation of the stress-favored martensite twin was indicated by plateau region at around 40 MPa by exhibiting a quite high hardening response due to difficulty in the martensite propagation (reorientation) at this length scale. It is evident that as the sample size decreased from bulk to 5 μm, reorientation stress significantly increased.

The post-deformation SEM image of the 5 μm pillar in Figure 5.5(d) shows the twin boundary between the magnetically-favored and stress-favored twins. This pillar did not exhibit any substrate effect in the stress-strain response, which was supported by the SEM images after deformation. It was observed that the stress-favored twin stopped when reached almost the bottom of the pillar without extending into the bulk material under the pillar.

5.3.2 Magnetic Field-induced Martensite Variant Reorientation in $Ni_{50}Mn_{28.3}Ga_{21.7}$ Pillars

Recovery of the deformed pillars due to magnetic field-induced martensite reorientation was studied by the application of 2 Tesla and 5 Tesla fields. Figure 5.6 shows the SEM pictures of the 20 μm pillar before and after deformation and after the application of 2 Tesla and 5 Tesla magnetic fields. The orientation of the tetragonal unit cells before and after martensite variant reorientation was drawn on the pillar images. As seen in Figure 5.6(a), the pillar before deformation has a martensite variant composed of tetragonal unit cells with their long axis oriented along the compression axis. Figure 5.6(b) shows the direction of the stress and magnetic field applied on the pillars. First of all, the pillar was deformed as explained in Section 5.3.1 and 1.6% residual strain remained upon unloading. After deformation of the pillar in Figure 5.6(a), the formation of the stress favored twin was observed in Figures 5.6(c) and (d) with the light contrast on the pillar. Deformation was followed by the application of magnetic field perpendicular to the compression direction. After application of 2T field, there is no twin boundary motion observed on the pillar surface as seen in Figure 5.6(e) and (f). When 5T field was applied after 2T, the stress-favored martensite variants were rotated by 90^{o} due to magnetic field-induced martensite reorientation. The martensite unit cells align their easy magnetization axis along the direction of the applied magnetic field. Since the easy magnetization axis in NiMnGa is the short axis (c-axis), the unit cells rotate such that the short axis becomes parallel to the direction of the magnetic field. As a result, the

recovery is obtained as this pillar completely recovered with 5T field. This can easily be observed by the disappearance of the stress-favored twin in Figure 5.6(g) and (h).

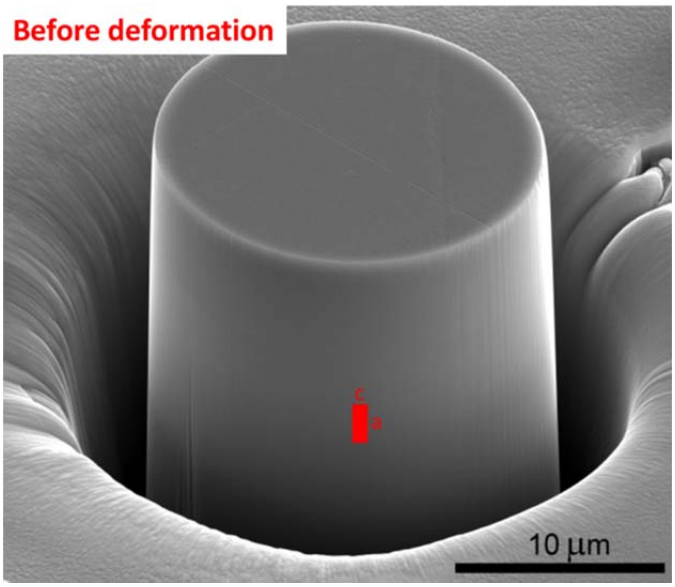

(a)

Figure 5.6 SEM images of the 20 µm $Ni_{50}Mn_{28.3}Ga_{21.7}$ single crystalline pillar, (a) before deformation, (b) before deformation showing first stress and then magnetic field application directions on the pillar, (c) after deformation (front side), (d) after deformation (back side), (e) after 2T field (front side) (f) after 2T field (back side), (g) after 5T field (front side), (h) after 5T field (back side). The orientation of the tetragonal unit cells for before and after martensite variant reorientation and after 2T and 5T magnetic field application was drawn on the pillar images. The unit cell with its long axis (a-axis) oriented along the compression direction represents the magnetically-favored martensite variant whereas the unit cell with its short axis (c-axis) oriented along the compression direction represents the stress-favored martensite variant. The residual material on the pillar in (c)-(h) comes from the pillar processing with AFM after deformation and magnetic field application.

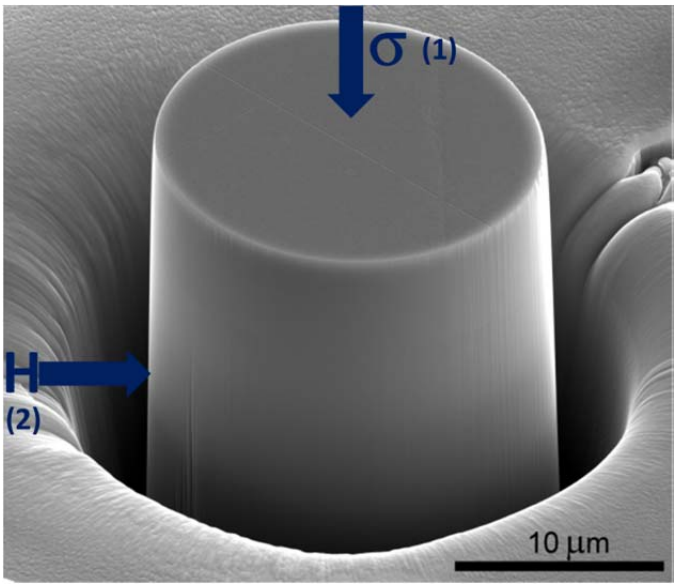

(b)

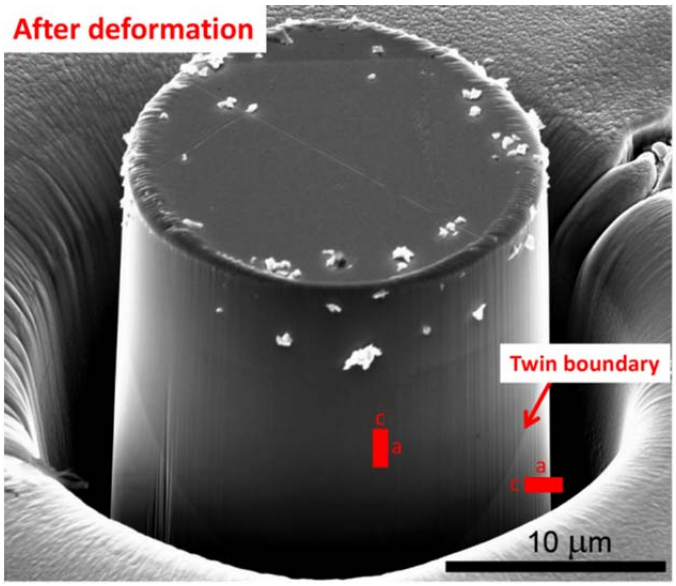

(c)

Figure 5.6 Continued.

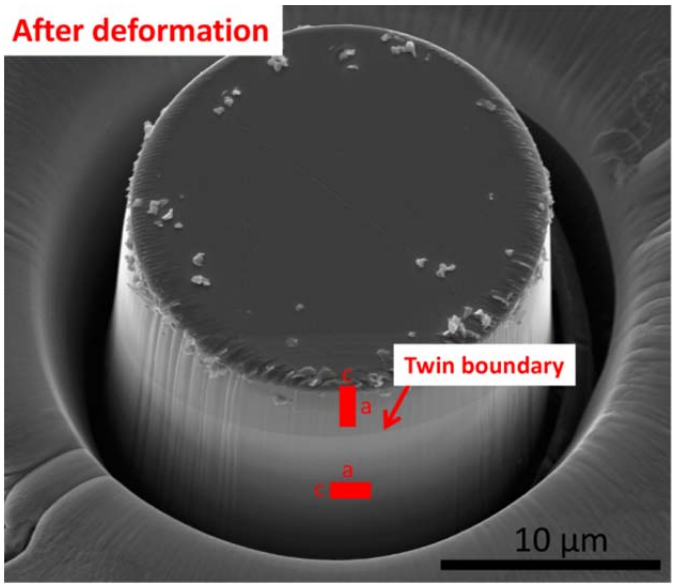

(d)

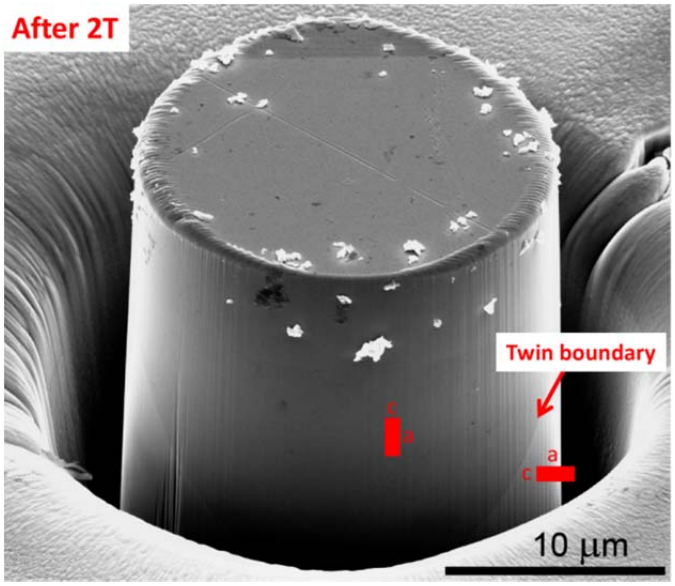

(e)

Figure 5.6 Continued.

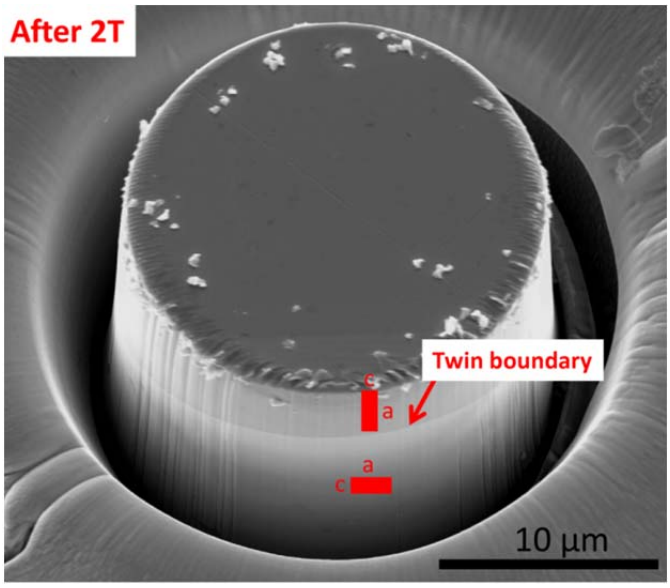

(f)

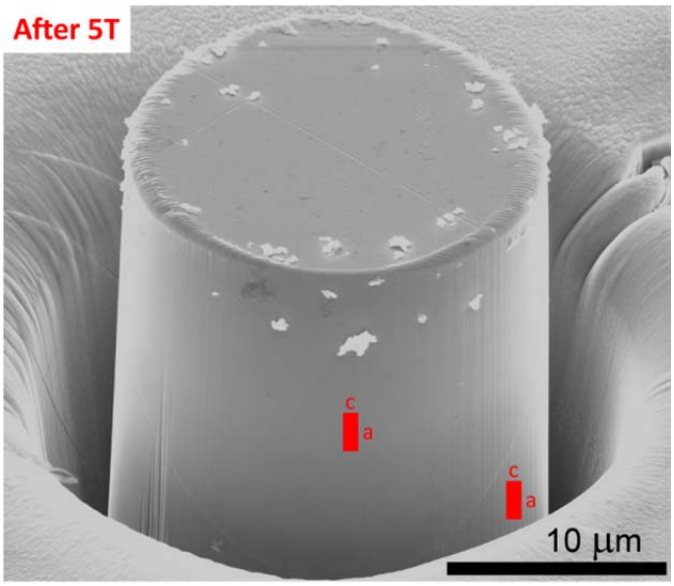

(g)

Figure 5.6 Continued.

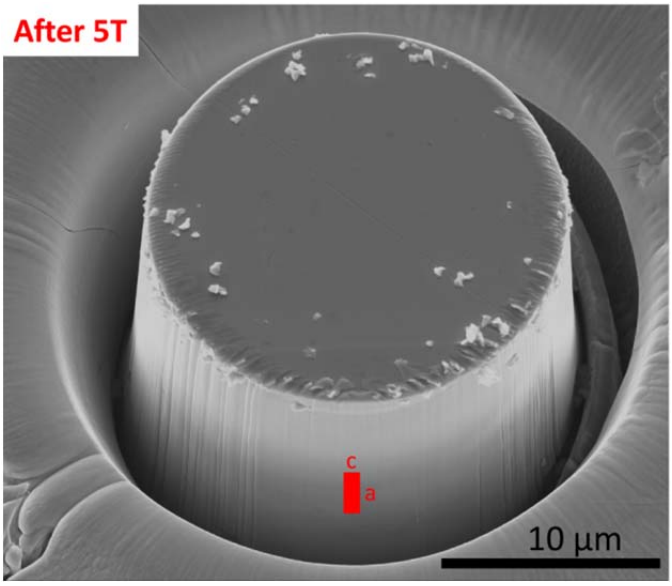

(h)

Figure 5.6 Continued.

Figure 5.7 shows the AFM profiles of this pillar before and after deformation and after application of 5T magnetic field. AFM profiles support the SEM pictures that this pillar completely recovered after the 5T field was applied.

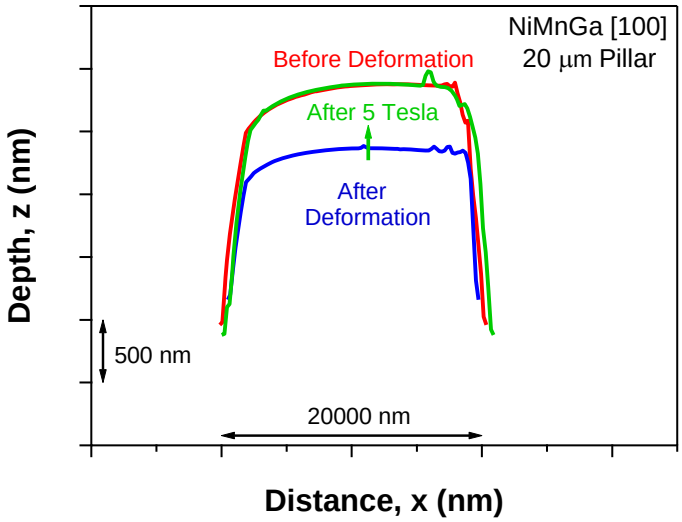

Figure 5.7 AFM profiles of the 20 μm $Ni_{50}Mn_{28.3}Ga_{21.7}$ single crystalline pillar before and after deformation and after the application of 5T magnetic field. The pillar profiles reveal the full recovery after application of 5T field.

SEM images of the 10 μm pillar before and after deformation and after 2 and 5 Tesla fields are seen in Figure 5.8. Before deformation, the pillar possesses only one type of martansite variant forming the magnetically-favored twin. Figure 5.8(a) shows the single crystalline 10 μm pillar before deformation and Figure 5.8(b) demonstrates the stress and magnetic field directions on this pillar. After deformation up to 4% strain and unloading, the pillar had 3.5% residual deformation as shown in Section 5.3.1. Formation of stress-induced twins can be observed in Figures 5.8(c) and (d) with different contrasts in the SEM pictures taken after deformation. Tetragonal unit cells were also sketched on the twins of the pillar images.

After deformation, 2T magnetic field in the direction perpendicular to the compression axis, was applied to the 10 μm pillar. When 2 Tesla was applied, there was no twin boundary motion on the pillar surface as shown in Figures 5.8(e) and (f). These images are exactly the same as the post-deformation images. This proved that the 2T field was not high enough to start the twin boundary motion and thus the recovery of this 10 μm pillar. After 2T magnetic field, 5T was applied to the pillar again in the direction perpendicular to its compression axis. When 5 Tesla was applied, this pillar showed new twin formation and the twin boundary motion as seen on the pillar surface in Figures 5.8(g) and (h). This means that the tetragonal martensite variants started to rotate by 90^{o} to orient the easy axis of magnetization (short axis) along the direction of the applied magnetic field. The formation of new magnetically-favored twin in this pillar shows that the magnetic field-induced martensite reorientation is possible at 5T in 10 μm size scale. However, this pillar still exhibits multi-variant twin state revealed by the presence of twins with different contrast in the SEM image even after 5T. This indicates that there is only partial recovery even at 5T in the 10 μm pillar.

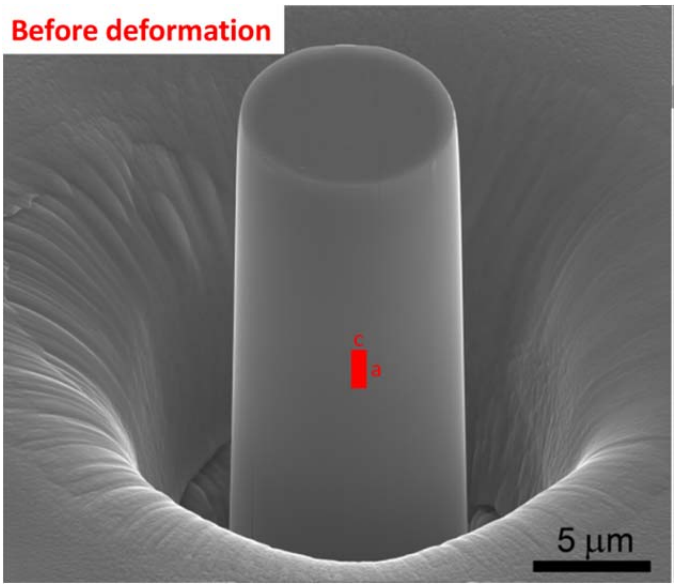

(a)

Figure 5.8 SEM images of the 10 µm $Ni_{50}Mn_{28.3}Ga_{21.7}$ single crystalline pillar, (a) before deformation, (b) before deformation showing first stress and then magnetic field application directions on the pillar, (c) after deformation (front side), (d) after deformation (back side), (e) after 2T field (front side), (the inset of the figure shows a closer image of the pillar surface), (f) after 2T field (back side), (g) after 5T field (front side), (the inset of the figure shows a closer image of the pillar surface), (h) after 5T field (back side). The orientation of the tetragonal unit cells for before and after martensite variant reorientation and after 2T and 5T magnetic field application was drawn on the pillar images. The unit cell with its long axis (a-axis) oriented along the compression direction represents the magnetically-favored martensite variant whereas the unit cell with its short axis (c-axis) oriented along the compression direction represents the stress-favored martensite variant. The residual material on the pillar in (c)-(h) comes from the pillar processing with AFM after deformation and magnetic field application.

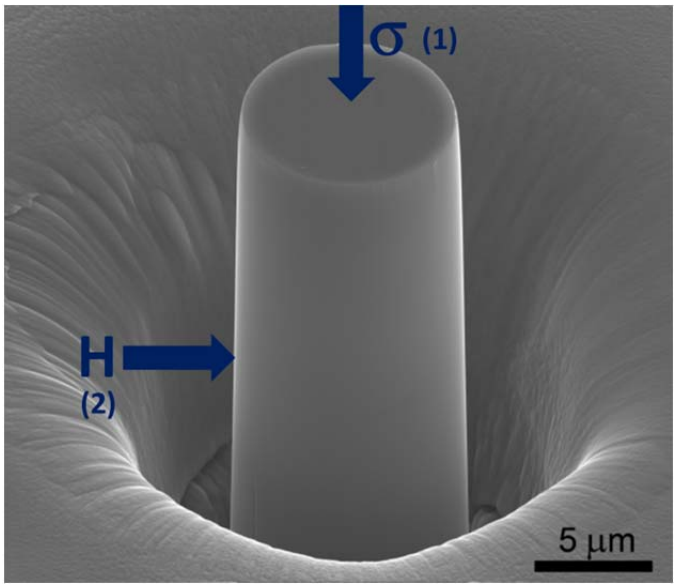

(b)

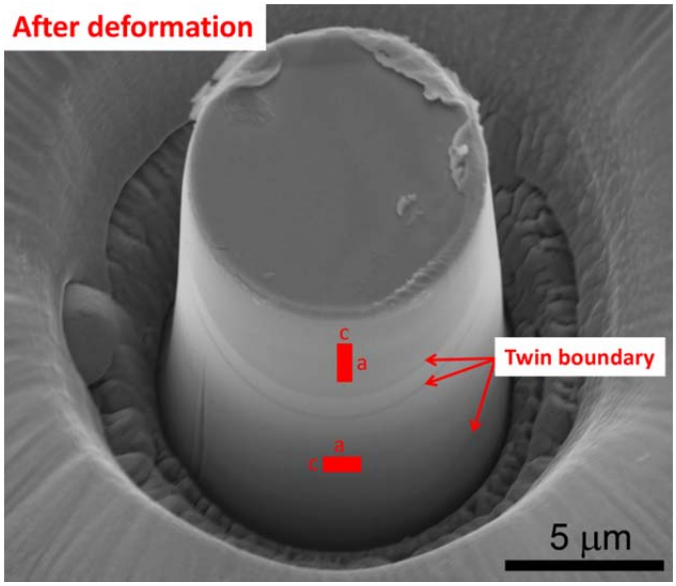

(c)

Figure 5.8 Continued.

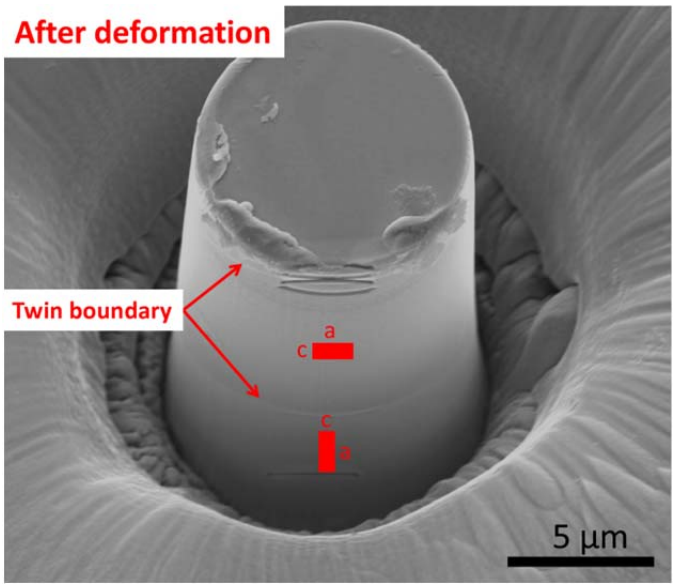

(d)

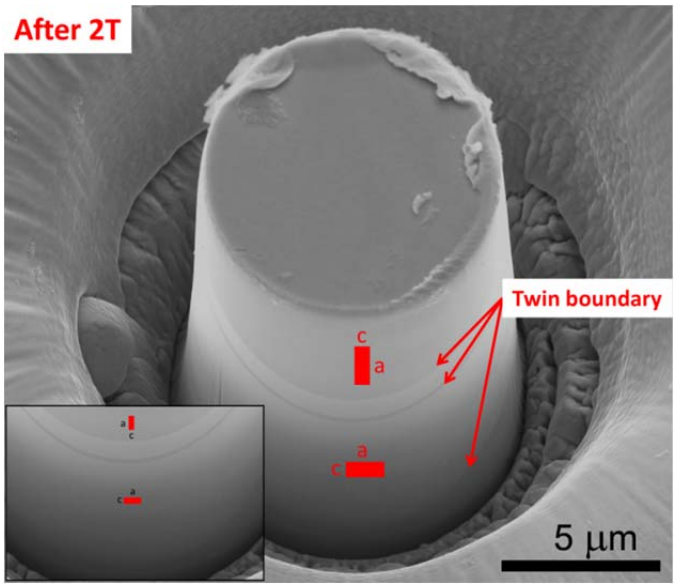

(e)

Figure 5.8 Continued.

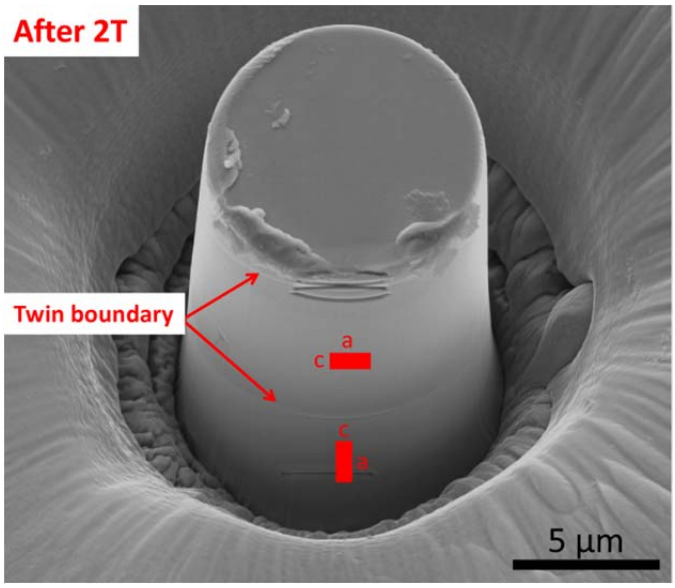

(f)

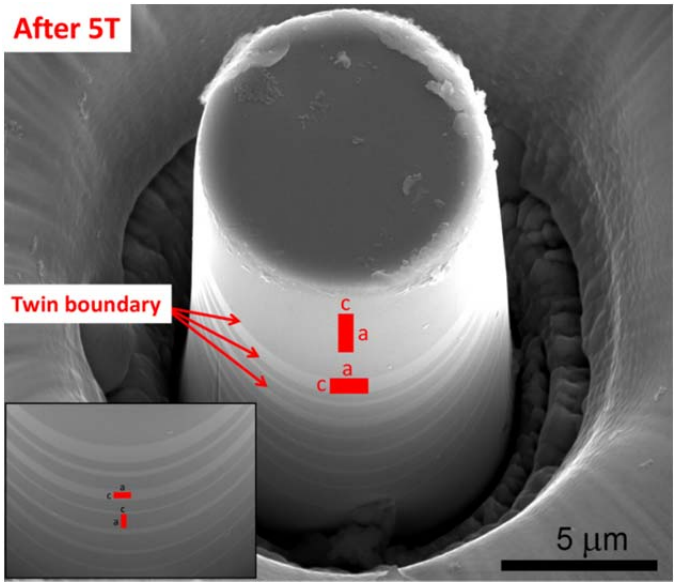

(g)

Figure 5.8 Continued.

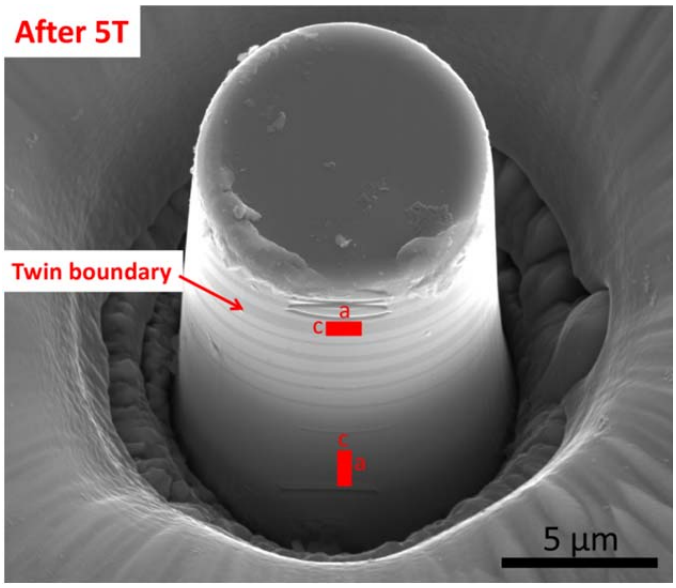

(h)

Figure 5.8 Continued.

These findings are supported by the AFM profiles presented in Figure 5.9. After 2T magnetic field, there was no increase in the pillar height and thus no recovery was observed. On the other hand, after 5T magnetic field, the pillar height increased as seen in the figure supporting the findings mentioned above that the partial recovery of this 10 µm pillar was obtained.

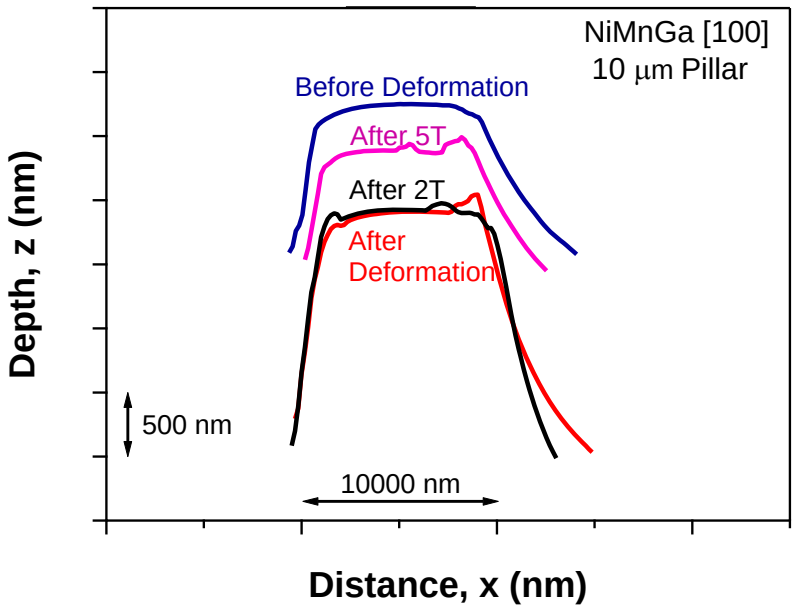

Figure 5.9 AFM profiles of the 10 μm $Ni_{50}Mn_{28.3}Ga_{21.7}$ single crystalline pillar before and after deformation and after the application of 2T and 5T magnetic field. The pillar profiles reveal that there is no recovery at 2T and the partial recovery is observed after application of 5T field.

The 5 μm pillar machined on the same magnetically-favored twin as the previous NiMnGa pillars is shown in Figure 5.10. Figure 5.10(a) reveals the pillar before deformation is a single variant martensite and the Figure 5.10(b) gives the direction of the applied stress and magnetic field. As shown in the Section 5.3.1, after compressing this pillar up to 4% strain, the pillar remained 3% residual deformation upon unloading. SEM images of this 5 μm pillar after deformation were given in Figures 5.10(c) and (d). The stress-favored twin forms in the pillar as indicated by the tetragonal unit cells with their short axis oriented along the compression direction. When 2T magnetic field was applied to this pillar, no twin boundary motion and therefore, no recovery was observed.

The SEM images taken after the application of 2T field were given in Figures 5.10(e) and (f). When 5T field was applied, the twin boundary motion was observed on the pillar surface. As seen in Figures 5.10(g) and (h), the volume fraction of the stress-favored twin decreased after 5T field by the upward movement of the twin boundary as indicated by the arrows.

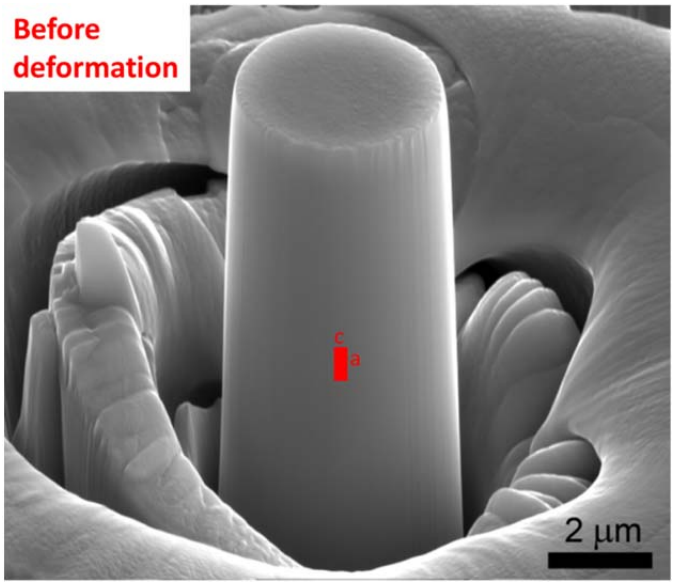

(a)

Figure 5.10 SEM images of the 5 μm $Ni_{50}Mn_{28.3}Ga_{21.7}$ single crystalline pillar, (a) before deformation, (b) before deformation showing first stress and then magnetic field application directions on the pillar, (c) after deformation (front side), (d) after deformation (back side), (e) after 2T field (front side) (f) after 2T field (back side), (g) after 5T field (front side), (h) after 5T field (back side). The orientation of the tetragonal unit cells for before and after martensite variant reorientation and after 2T and 5T magnetic field application was drawn on the pillar images. The unit cell with its long axis (a-axis) oriented along the compression direction represents the magnetically-favored martensite variant whereas the unit cell with its short axis (c-axis) oriented along the compression direction represents the stress-favored martensite variant.

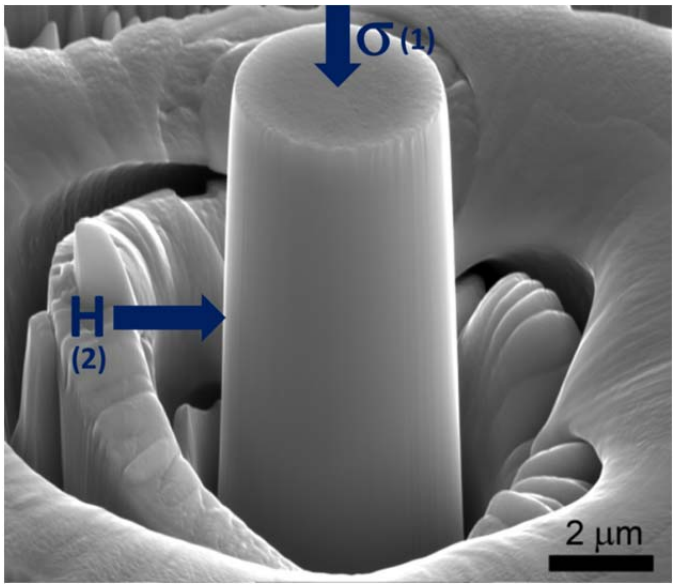

(b)

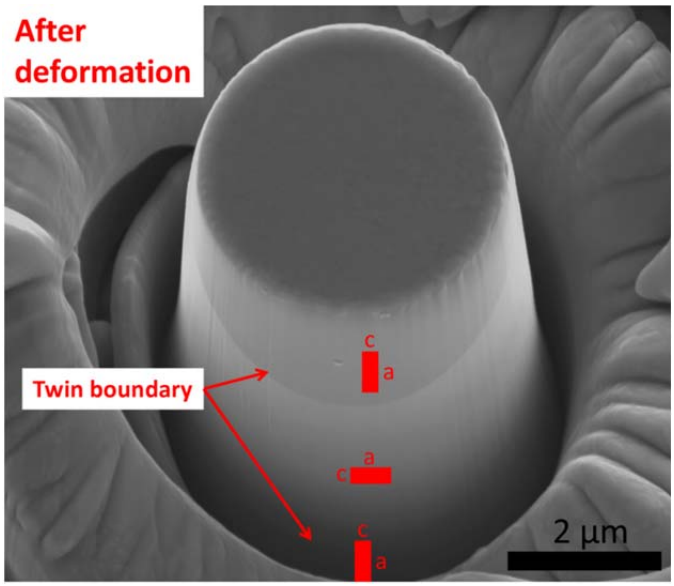

(c)

Figure 5.10 Continued.

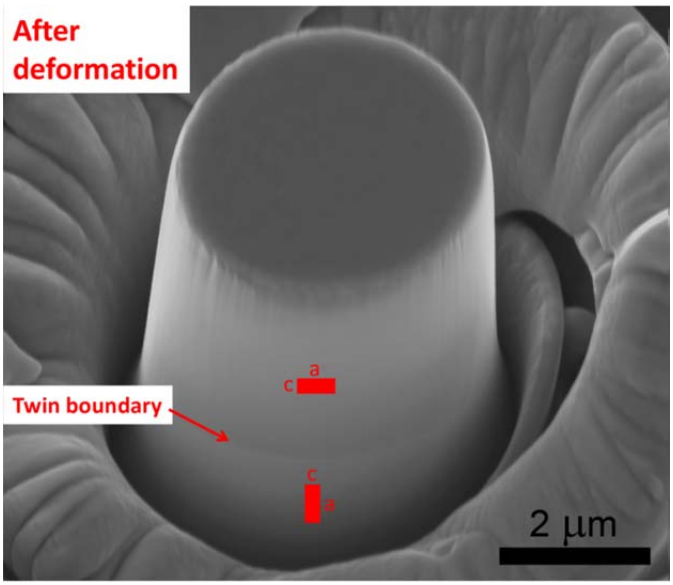

(d)

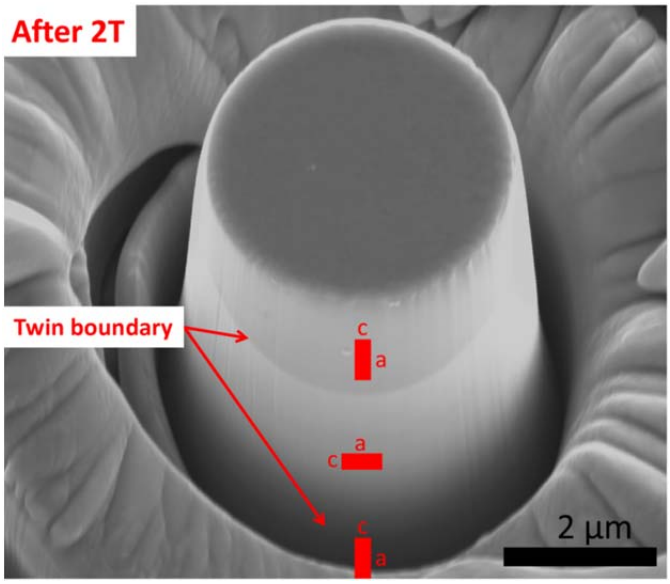

(e)

Figure 5.10 Continued.

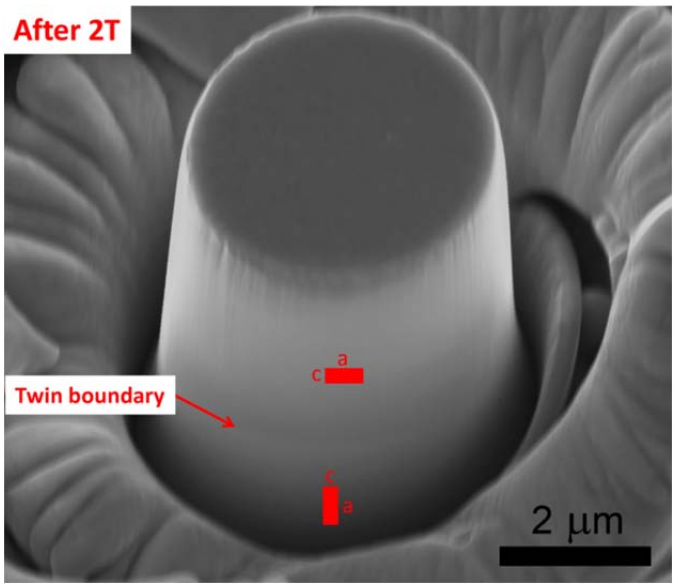

(f)

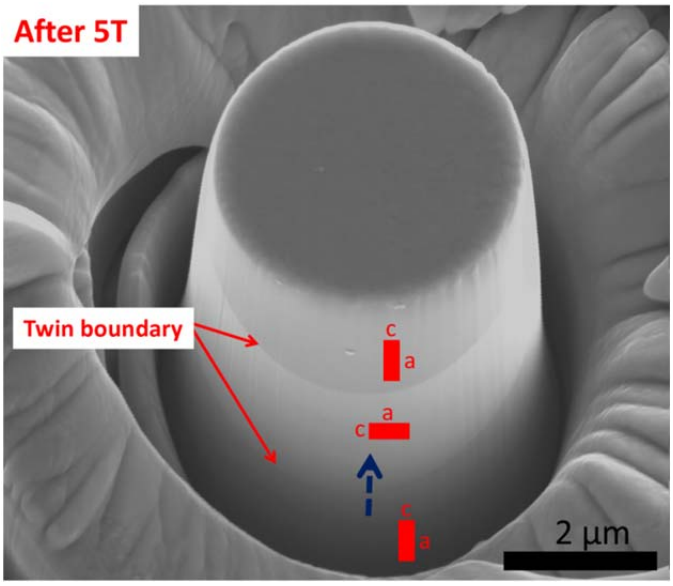

(g)

Figure 5.10 Continued.

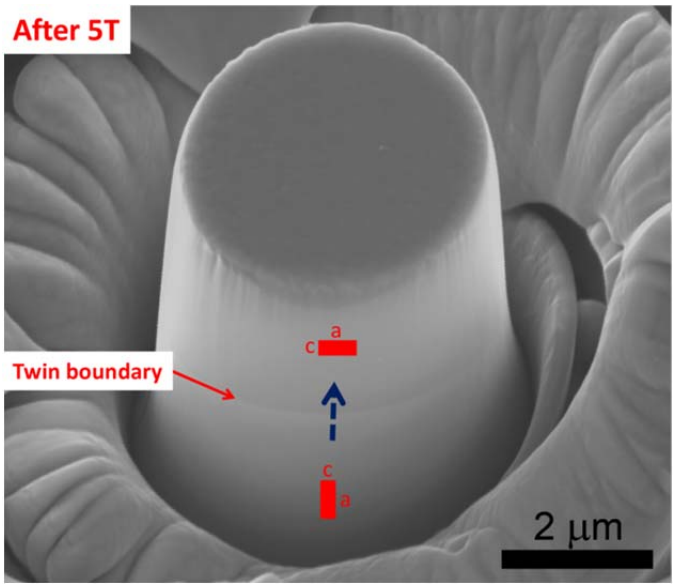

(h)

Figure 5.10 Continued.

The summary of the above observations is that the 20 μm, 10 μm and the 5 μm NiMnGa single crystalline pillars exhibited a similar response under magnetic field. The magnetic field-induced martensite variant reorientation started when the magnetic field between 2T and 5T was applied perpendicular to the compression direction of the pillars. As given in the Section 5.2, the bulk specimen shows martensite reorientation below 0.8T which is the field level required to magnetically saturate the bulk single crystal. Since these micropillars have such high martensite reorientation stresses, it is expected that the 0.8T field is not enough to start the recovery. On the other hand, these results are somewhat surprising because we would expect to reach the saturation field with the micropillars also at around 0.8T and therefore not to observe the martensite reorientation

at magnetic fields higher than 0.8T. In these findings, we show completely different response that the micropillars can still recover at magnetic field higher than the saturation magnetic field of the bulk crystal.

These results on the Ni-Mn-Ga micropillars seem to be brand new fundamental findings that shed light into some possible phenomenon. We suggest that our findings reveal an increase in saturation magnetic field with decreasing sample size such that the micropillars can still show martensite reorientation at magnetic fields higher than the saturation field of their bulk counterpart. Figure 5.11 illustrates a schematic of the magnetization response of the hard and easy axis of martensite variants. An energy term called magnetocrystalline anisotropy energy (MAE or K_u) in Ni-Mn-Ga is determined by the area between the magnetization vesus magnetic field response of ferromagnetic martensite variants along the easy and hard axes. MAE is orientation dependent and is limited by the saturation magnetic field [1, 87]. In order to obtain twin boundary motion, MAE must be higher than the energy required for the twin boundary motion. Since MAE is limited by the saturation magnetic field, it seems to be constant for a material with the given composition and orientation. However, our results suggested that when the size of the sample is decreased, the saturation field increased making it still possible to activate the shape change at higher magnetic fields. The increase in the saturation field leads to an increase in the MAE. This was illustrated by the shift in the saturation magnetic field of the bulk, $H_{s(bulk)}$, into that of the pillars, $H_{s(pillars)}$, resulting in a larger area under the easy and hard axis magnetization responses in Figure 5.11.

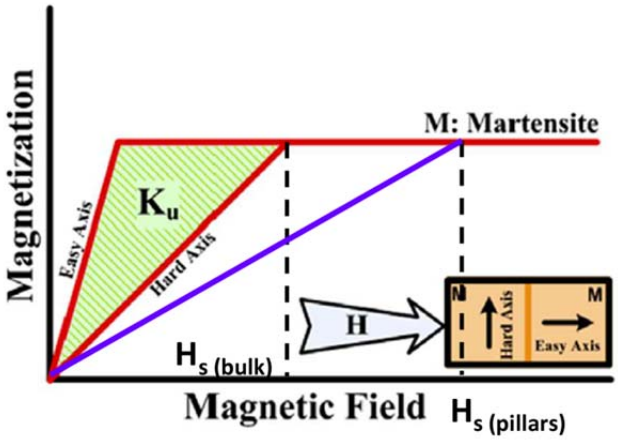

Figure 5.11 Schematics showing the easy and hard axis magnetization response of Ni-Mn-Ga. $H_{s(bulk)}$: Saturation magnetic field for the bulk sample. $H_{s(pillars)}$: Saturation magnetic field for the pillars. K_u: Magnetocrystalline anisotropy energy. Figure modified from reference [88].

This major finding of the increase in the MAE with the reduction in sample size, concluded from the experimental findings has not been shown in the literature previously, either directly or indirectly. We expect that magneto-microstructural coupling (i.e. the coupling between martensite twins and magnetic domain walls) would have a significant effect on the field-induced martensite reorientation and MAE in these materials in small sizes. This is due to the fact that one-to-one correspondence between magnetic domains and martensite twins are observed in Ni-Mn-Ga MSMAs especially when the twin sizes are in the low micron and sub-micron range. The specimen size has an effect on the martensite twin size as shown by Ganor et al. [8] and we argue that the martensite twin size dictates the magnetic domain size. In turn, the smallest domain size means higher volume fraction of domain walls, which make magnetic switching harder

and harder, especially for 90^o domain walls, and thus, lead to higher MAE. Indeed such magneto-structural correspondence and the control of magnetic domains with specimen shape and size control led to a two-fold increase in actuation stress levels in Ni-Mn-Ga experiencing field-induced martensite reorientation [8].

5.3.3 Magnetic Field Distribution in $Ni_{50}Mn_{28.3}Ga_{21.7}$ Pillars

In order to support the experimental observations obtained for the $Ni_{50}Mn_{28.3}Ga_{21.7}$ pillars in the present study, we investigated the magnetic field distribution in the pillars and their surroundings. The reason for examining the field distribution in the pillars was to identify whether there is a geometry effect that prevents the pillars from being exposed to the applied magnetic field due to the large opening around them. The previously mentioned experimental findings on the increase in saturation magnetization with decreasing sample size can therefore be proved if the modeling results conclude the trench surrounding the pillars does not create a large inhomogeneity in the magnetic field distribution in the pillars. The model for the 10 μm $Ni_{50}Mn_{28.3}Ga_{21.7}$ pillar was investigated using the Opera software. Since every pillar has a similar surrounding geometry, 20 μm and 5 μm pillars should have a similar magnetic field distribution as the 10 μm pillar.

The 10 μm pillar was modeled in the Opera software. The entire pillar geometry and its surrounding were created in the software by copying all the dimensions from the SEM images taken before deforming the pillar. As seen in Figure 5.12(a), the SEM

image of the pillar (the inset of the figure) and the image created in the software are in one to one correspondence.

First of all, the 2T magnetic field was applied to the 10 μm pillar in the Opera as shown in Figure 5.12(a). Direction of the magnetic field was kept the same as in the experimental conditions. Then, the magnetic field distribution in the pillar and its surrounding was examined quantitatively. Figure 5.12(b) shows the magnetic field profile along the pillar length. The pillar is exposed to at least around 1.6T magnetic field when 2T external field is applied. It is obvious that the opening around the pillar affected the magnetite of the magnetic field that can reach the pillar, however this much influence does not change any of the conclusions made previously according to the experimental observations. The minimum field in the pillar, ~1.6T, is still well above the 0.8T saturation magnetic field of the bulk.

Figure 5.12(c) gives the same 10 μm pillar model under 5T external magnetic field. It is clear that the magnetic field that can reach the pillar is smaller than the externally applied field but it is still extremely high in comparison to the saturation field of the bulk. The pillar is exposed to at least 4.6T field when the 5T is applied and the difference is the loss due to the geometry of the pillar and its surrounding. As mentioned previously, even though the 4.6T is above the saturation field of the bulk, it provided magnetically-induced shape change in the 10 μm pillar as shown experimentally in the Section 5.3.2. These findings on modeling of the field distribution in the 10 μm pillar reveal that although the trench structure surrounding the pillars blocks some of the applied field, the magnetite of the field is still high enough in the pillars to support our

experimental findings on the increase in the saturation magnetic field with decreasing sample size.

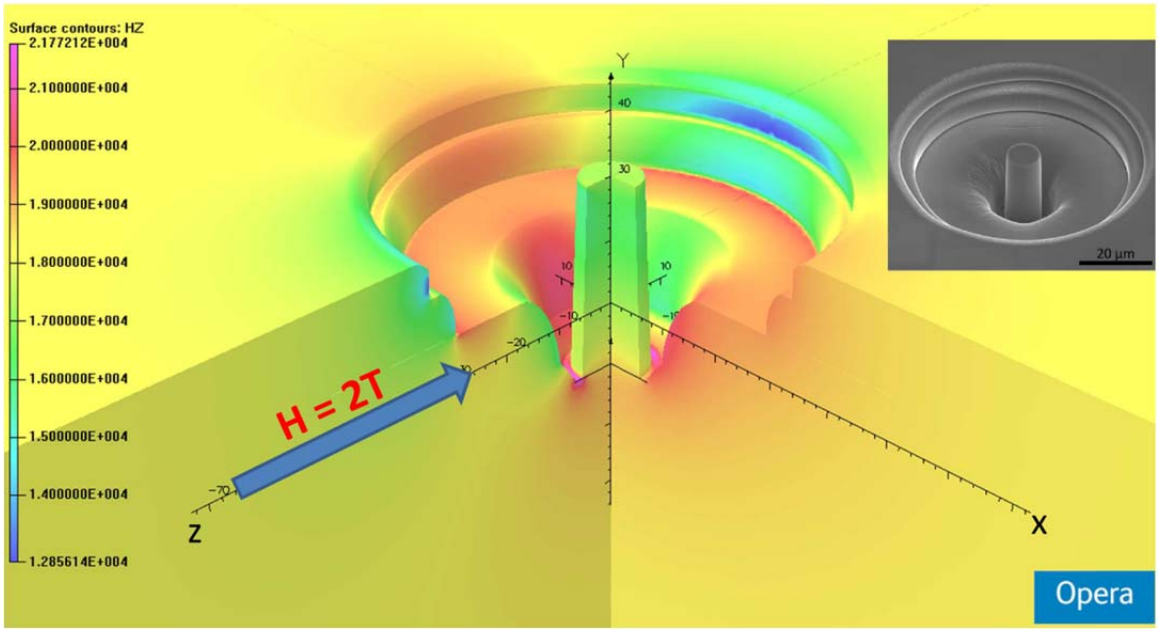

(a)

Figure 5.12 Modeling of the magnetic field distribution in the 10 µm $Ni_{50}Mn_{28.3}Ga_{21.7}$ single crystalline pillar and its surrounding, (a) for 2T magnetic field showing the field distribution along the pillar length in (b), (c) for 5T magnetic field.

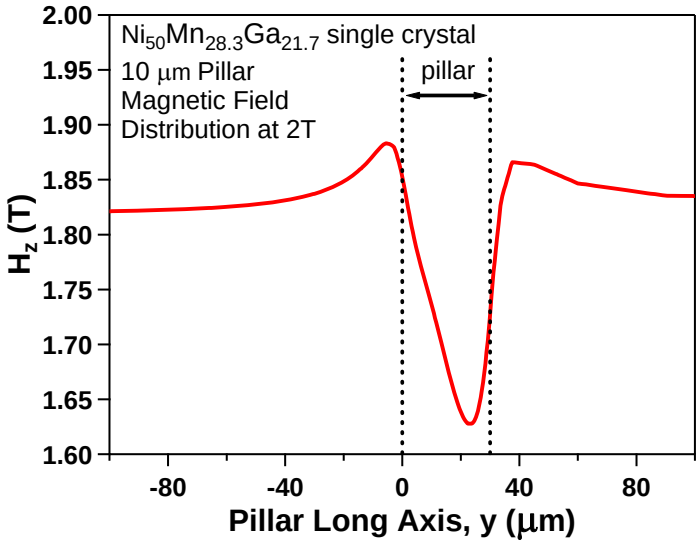

(b)

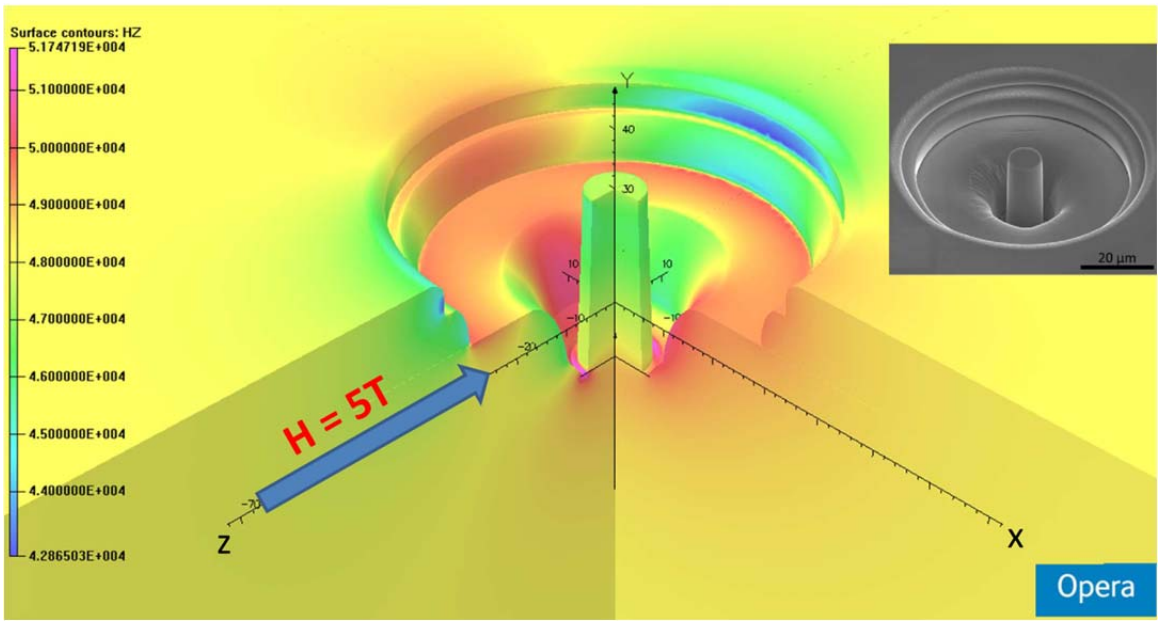

(c)

Figure 5.12 Continued.

Another issue that was investigated using this model was the stress generated on these pillars as a result of inhomogeneous magnetic field distribution. One can argue that if these pillars are exposed to the tensile force due to the inhomogeneous magnetic field, their length can increase regardless of the magnetic field-induced martensite reorientation. In order to examine whether such response would be possible, the stress generated on the 10 μm pillar was calculated by the Opera software using a Maxwell tensor enclosed by the selected volume. When 2T field was applied, the pillar experienced 0.20 MPa tensile stress and this stress was 0.22 MPa when the field was increased to 5T. It is obvious that the stress values calculated by the magnetic field distribution on the pillar were very small that it cannot elongate this pillar having 18-21.5 MPa reorientation stress. In conclusion, the slight inhomogeneous magnetic field distribution in the present study cannot cause any increase in the pillar lengths and the recovery observed in the $Ni_{50}Mn_{28.3}Ga_{21.7}$ pillars can only be due to magnetic field-induced martensite reorientation.

5.4 Superelasticity in Small Size $Ni_{50}Mn_{28.3}Ga_{21.7}$ Pillars

$Ni_{50}Mn_{28.3}Ga_{21.7}$ single crystalline pillars with the diameters of 2 μm, 1 μm and 630 nm were machined in the same magnetically-favored martensite twin as the previous larger $Ni_{50}Mn_{28.3}Ga_{21.7}$ single crystalline pillars. These smaller pillars demonstrated different response from the aforementioned larger pillars showing martensite reorientation. While pillars down to 5 μm size exhibited martensite reorientation, superelasticity was observed during unloading at the smaller size scale.

Figure 5.13(a) shows an image of the 2 μm $Ni_{50}Mn_{28.3}Ga_{21.7}$ pillar and Figure 5.13(b) gives the stress-strain response of this pillar including three consecutive loading/unloading cycles. It is apparent that the pillar had some amount of recovery upon unloading in each straining cycle. Even though this 2 μm pillar is on a martensite twin, its deformation response resembles an austenite to martensite phase transformation resulting in superelasticity in SMAs. There is a clear change in the elastic slope of the stress-strain response at around 60 MPa, especially in the first two straining cycles. This high stress level is also an indicative of an involvement of a phase transformation in this deformation process. Further loading above the 5% strain generated a large amount of residual strain, which can be due to local defect generation at this stress level. The third straining cycle included many abrupt stress drops resulted from large and sudden displacement changes. In micro/nano mechanical testing, this is due to the continuous defect generation and annihilation in the pillar microstructure which resulted in a local plasticity and large irrecoverability in this case.

Figures 5.13(c), (d), (e) and (f) show the images of this pillar for before deformation, after deformation, after application of 2T and 5T fields respectively. After compression experiment, the pillar has prominent deformation at around its half-length, which is pointed out with an arrow in the Figures 5.13(d), (e) and (f). When magnetic fields of 2T and 5T were applied, no recognizable change was observed on the pillar surfaces indicating that there is no recovery due to martensite reorientation.

The superelasticity can be observed as a result of the stress-induced austenite to martensite phase transformation. It is surprising to see the superelastic response in this 2

μm pillar fabricated from a martensitic twin. As explained in Section 2.1, the martensitic transformation temperature (M_s) decreases with the size of the specimen at this length scale. The 2 μm pillar seems to become a mixture of martensite and austenite due to decrease in M_s with decreasing sample size from bulk to 2 μm. As a result of this, partial superelasticity was observed in this pillar at room temperature. 2 μm sample size seems to be the length scale at which the martensitic bulk sample becomes a mixture of austenite and martensite at room temperature.

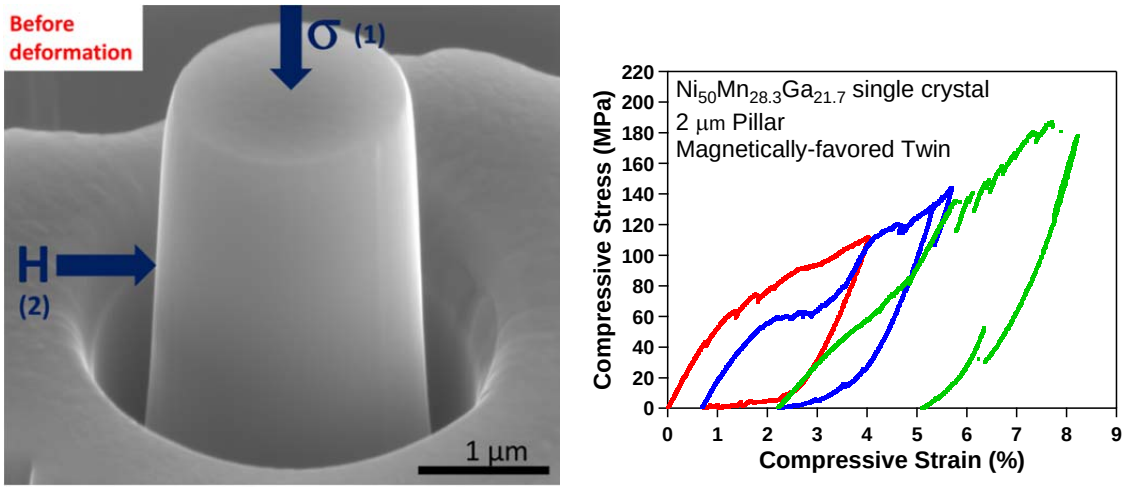

(a) (b)

Figure 5.13 (a) SEM image of the $Ni_{50}Mn_{28.3}Ga_{21.7}$ pillar with 2 μm diameter illustrating the compression and magnetic field application directions. (b) Compressive stress-strain response of this 2 μm $Ni_{50}Mn_{28.3}Ga_{21.7}$ pillar showing the three consecutive straining cycles. SEM images of this pillar, (c) before deformation using 20° tilt, (d) after deformation, (e) after 2T field and, (f) after 5T field using the same tilt of 15°. Arrows in the images indicate the deformed region of the pillar.

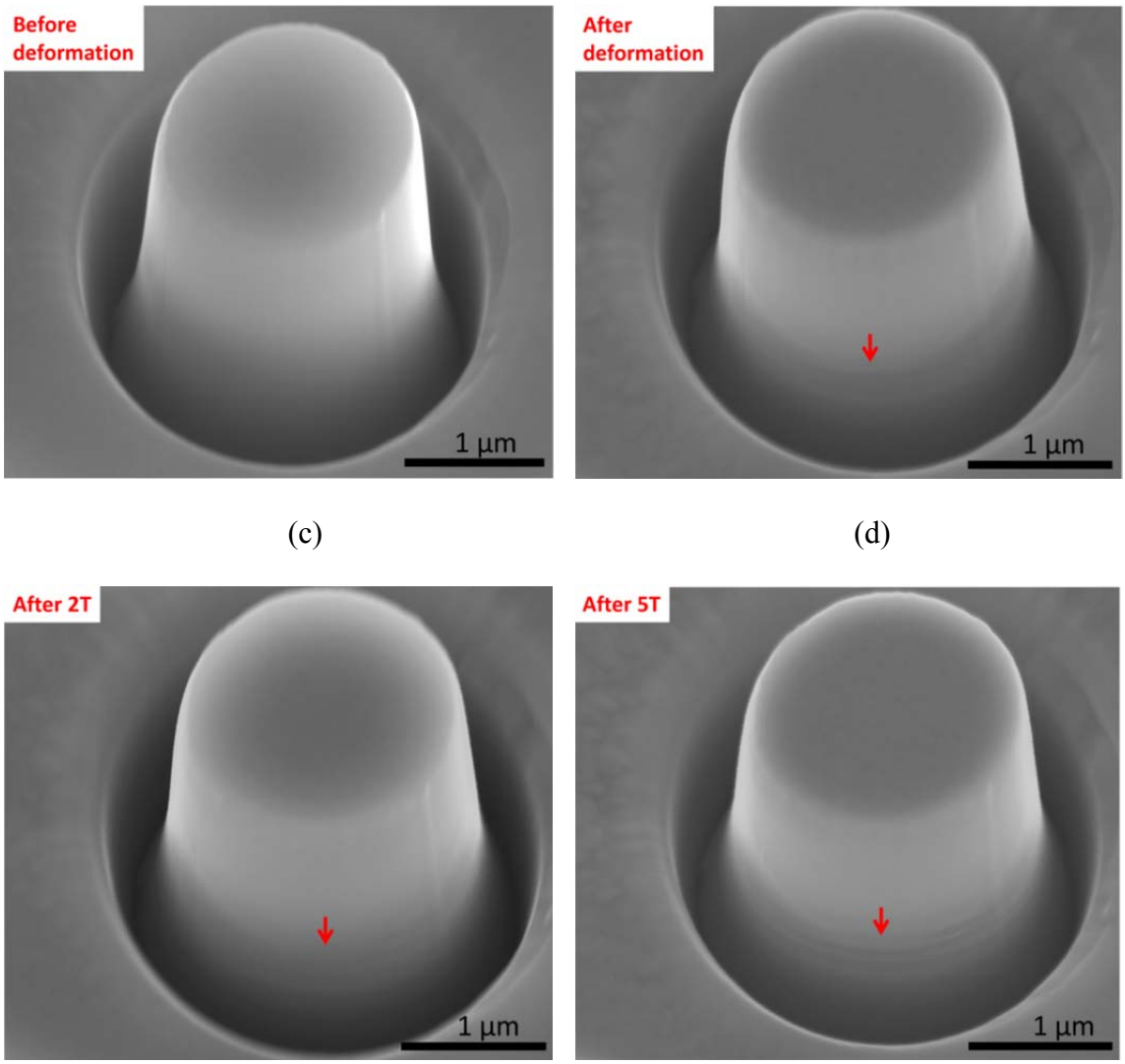

Figure 5.13 Continued.

1 µm $Ni_{50}Mn_{28.3}Ga_{21.7}$ pillar on the same magnetically-favored twin as the previous pillars exhibited a similar response to the 2 µm pillar with even more prominent superelasticity. Figure 5.14(a), (b), (c) and (d) show the loading/unloading cycles of this single crystalline 1 µm pillar. Even though the pillar was fabricated in a martensite twin,

almost perfect superelastic behavior was observed upon unloading from 4%, 5.6% and 6.8% strains incrementally. There is only small amount of residual strain after each straining cycle, which added up to be about 1% after four consecutive loading/unloading cycles. It seems like the compressive response of this 1 μm pillar is an austenite to martensite phase transformation with the onset of the transformation occurring at around 130 MPa. At 130 MPa, the plateau region was reached where the martensite nucleation and propagation took place. The sudden stress drops during loading indicate the martensite nucleation within the small single crystal pillar lacking of the pre-existing nucleation sites. Upon unloading, the pillar exhibited a reverse transformation from martensite to austenite with sudden stress increases in the stress-strain response. The stress jumps during unloading are caused by the sudden displacement changes due to the recovery of the pillar via reverse martensitic transformation. The plateau region which extended up to ~6% strain is an indicative of the 10M martensite formation in Ni-Mn-Ga [86]. At the end of the plateau region the 10M martensite started to deform elastically.

Figures 5.14(e) and (f) show the 1 μm $Ni_{50}Mn_{28.3}Ga_{21.7}$ pillar before and after deformation respectively. Images for before and after deformation of this pillar are also given in Figures 5.14(g) and (h) from a different tilt angle. Even though there appeared to be very fine residual surface relieves on the pillar surface after deformation, it was not clearly observed with the resolution that can be obtained in these images. In addition, there is no bending and noticeable residual deformation on this pillar as seen in the post deformation images.

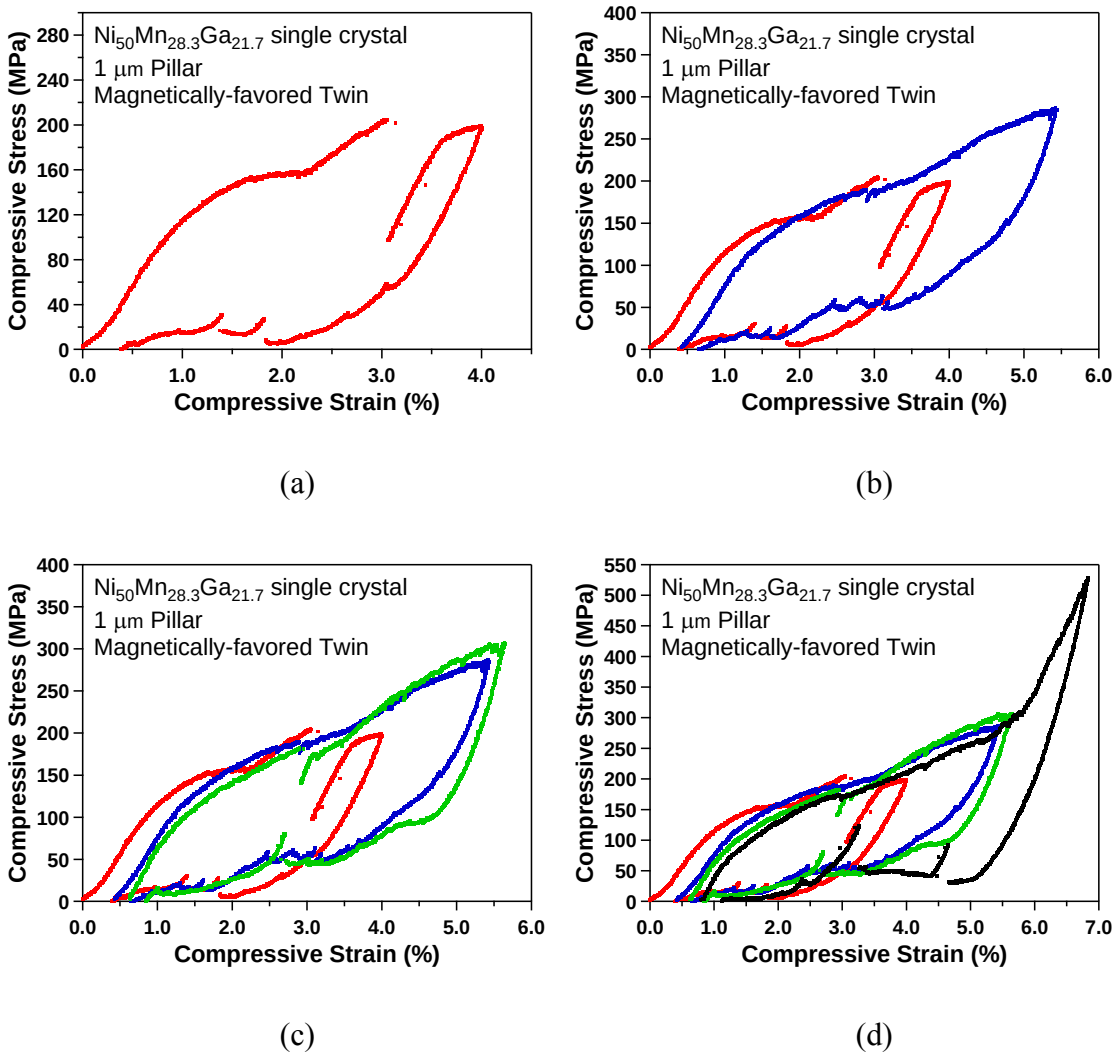

Figure 5.14 Compressive stress-strain response of the 1 μm $Ni_{50}Mn_{28.3}Ga_{21.7}$ pillar showing the first straining cycle in (a), the first two straining cycles in (b), the first three straining cycles in (c), and all the consecutive straining cycles in (d). SEM images of this pillar, (e) and (g) before deformation and, (f) and (h) after deformation. Images in (e) and (f) were both taken at 52° tilt angle and images in (g) and (h) were taken at 15° tilt angle. The residual material on the pillar in (f) and (g) comes from the pillar processing with AFM after deformation.

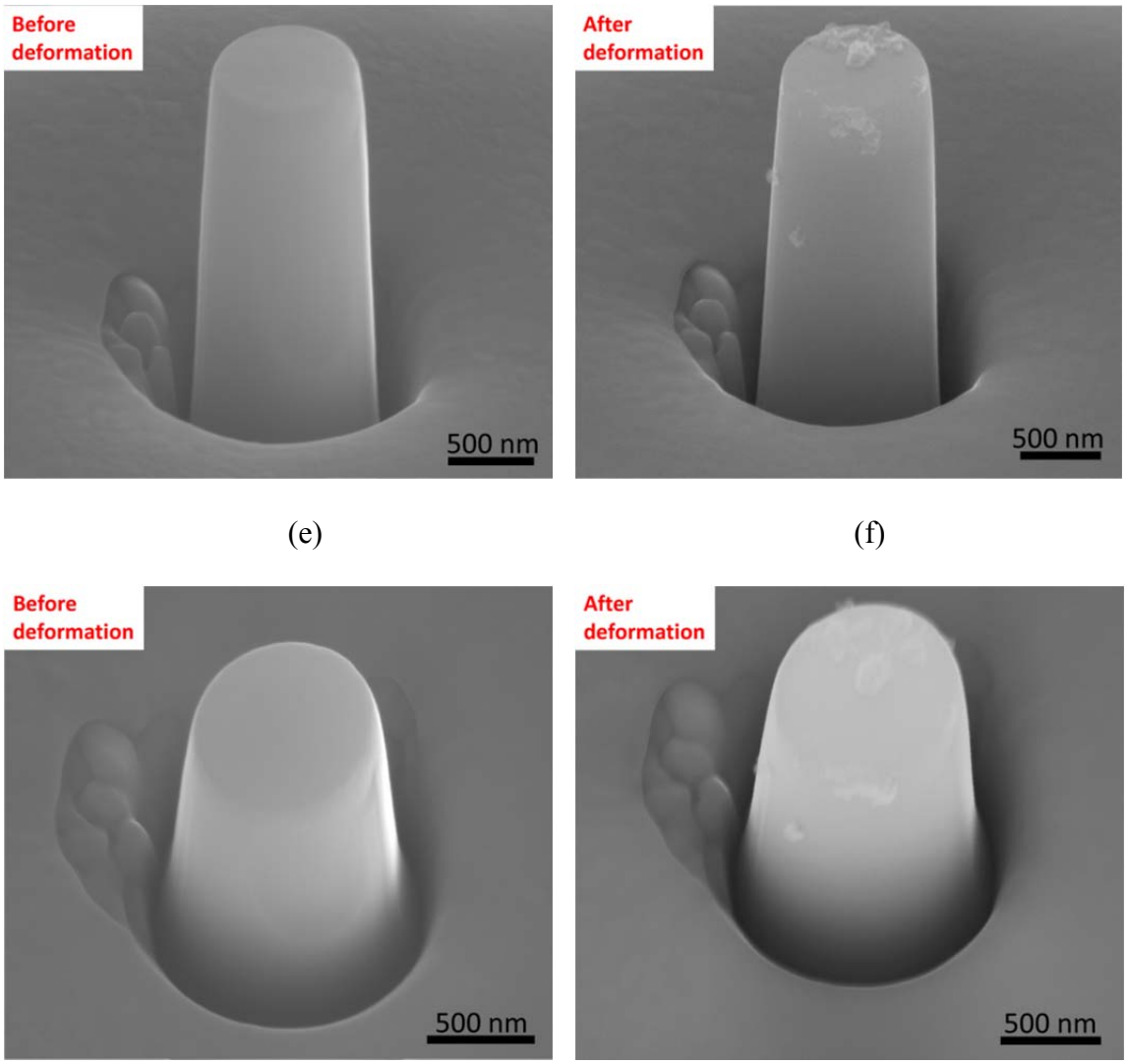

Figure 5.14 Continued.

In comparison to the 2 μm pillar, the 1 μm $Ni_{50}Mn_{28.3}Ga_{21.7}$ pillar exhibited more prominent superelasticity. Since the 1 μm is smaller, its martensitic transformation temperature should be lower than that of the 2 μm pillar. Therefore, it is expected that the 1 μm pillar is completely or mostly austenite at room temperature due to decrease in

the transformation temperatures with the sample size. Consequently, even though this pillar was fabricated using a martensitic twin, it transformed into austenite because of the size effects in the transformation temperatures and exhibited a superelastic response at room temperature.

The smallest pillar size studied for the $Ni_{50}Mn_{28.3}Ga_{21.7}$ sample was 630 nm. This pillar was fabricated in the same magnetically-favored twin as the previous $Ni_{50}Mn_{28.3}Ga_{21.7}$ pillars. Figure 5.15(a) shows the pillar image before deformation including the stress and magnetic field application direction. Compressive stress-strain response of this pillar is given in Figure 5.15(b). The pillar was incrementally strained up to 8.7% deformation. During unloading from 8.7% strain, the pillar exhibited some recovery and 3.2% residual strained remained in the pillar. Even though large recoverable strains were observed after each staining cycle, the shape of the stress-strain plot of this pillar did not exhibit a typical superelastic response. It rather seems to be plastic deformation with some amount of phase transformation associated with it. It should be noted that the stress levels reached were also very high in each cycle for the perfect superelasticity to take place.

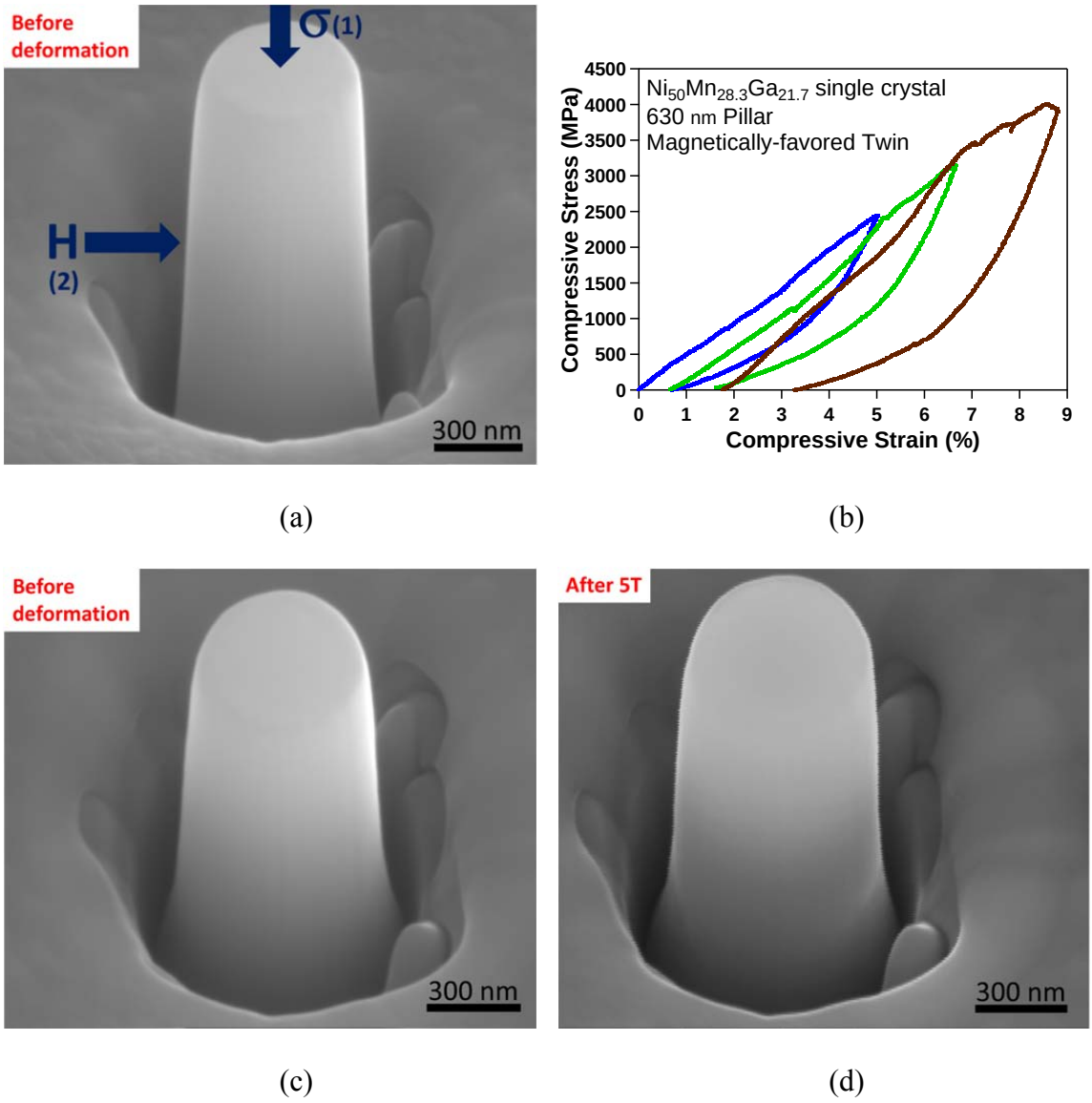

Figure 5.15 (a) SEM image of the $Ni_{50}Mn_{28.3}Ga_{21.7}$ pillar with 630 nm diameter illustrating the compression and magnetic field application directions. (b) Compressive stress-strain response of this 630 nm $Ni_{50}Mn_{28.3}Ga_{21.7}$ pillar showing the three consecutive straining cycles. SEM image of this pillar, (c) before deformation and, (d) after application of 5T magnetic field followed the pillar compression. Images in (c) and (d) were taken from the same tilt angle of 30^{o}.

Figures 5.15(c) and (d) show the 630 nm pillar before deformation and after application of 5T field following the pillar deformation, respectively. As seen in Figure 5.15(d), the pillar had a large deformation located at around its half-length and the magnetic field was not able to recover any of this deformation. The deformation appears as a bulging on the pillar surface formed as a result of the plastic deformation. It seems that the superelasticity observed in the 2 μm and the 1 μm pillars was deteriorated at the 630 nm size scale and plasticity of austenite dominated the deformation mechanism.

5.5 Plastic Deformation in $Ni_{50}Mn_{28.3}Ga_{21.7}$ Pillars

Compression pillars on the stress-favored twin of the $Ni_{50}Mn_{28.3}Ga_{21.7}$ bulk specimen were investigated in order to examine the plasticity at different sizes. Two pillar sizes studied were 10 μm and 1 μm. These two pillars were fabricate on the same stress-favored twin of the bulk specimen.

Figure 5.16(a) shows the stress-strain response of the 10 μm pillar. As a result of the incremental straining of the pillar, the pillar exhibited plastic deformation. The onset of the plastic deformation was at 1250 MPa. Figure 5.16(b) and (c) show this pillar before and after deformation, respectively. Since the pillar is on the stress-favored twin, it consists of tetragonal unit cells with their short axis (c-axis) already parallel to the compression direction as seen in Figure 5.16(b). Therefore, when the pillar was deformed, the martensite reorientation was not observed as expected and the pillar was

plastically deformed. The plastic deformation was associated with a kink formation as observed in Figure 5.16(c). Once the kink formed, it created an inhomogeneous or non-uniaxial compression of the pillar during further loading, resulting in bending-like behavior. This effect caused a spring response in the pillar which is observed as the recovery in the stress-strain response upon unloading.

Figure 5.17(a) shows the stress-strain response of the 1 μm pillar on the stress-favored twin. This pillar exhibited 1470 MPa stress at the onset of plastic deformation which is higher than the stress requires for the 10 μm pillar (1250 MPa). Large stress drops appeared during deformation due to continuous need for defect generation rather than only propagation of pre-existing defects. Additionally, the pillar did not show any martensite reorientation and phase transformation. The images of the pillar for before and after deformation are given in Figures 5.17(b) and (c), respectively. During plastic deformation, a kink formed in the pillar as indicated by the arrow in (c), similar to the 10 μm pillar.

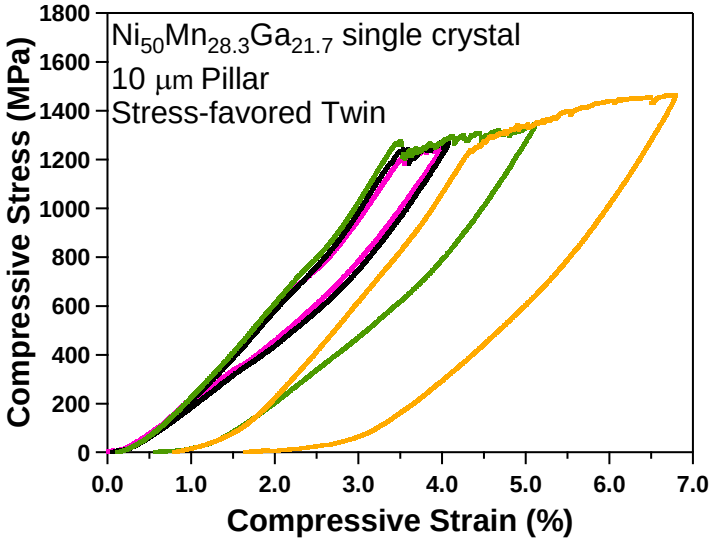

(a)

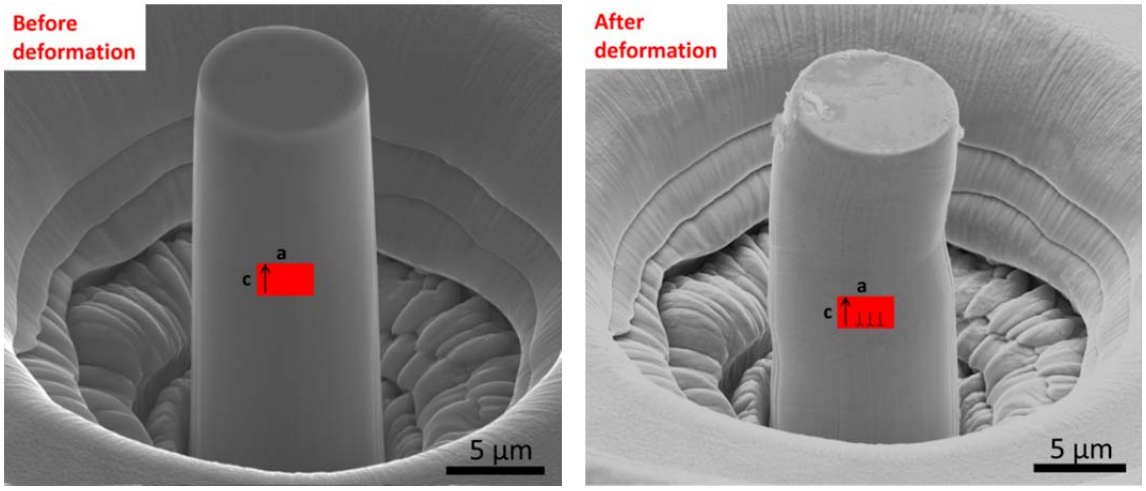

(b) (c)

Figure 5.16 (a) Compressive stress-strain response of the 10 μm $Ni_{50}Mn_{28.3}Ga_{21.7}$ pillar fabricated in the stress-favored twin. Compression response reveals the plastic deformation of the pillar. SEM images of this pillar, (b) before deformation, and (c) after deformation. The orientation of the tetragonal unit cells for the stress-favored martensite variant were sketched on the pillar images.

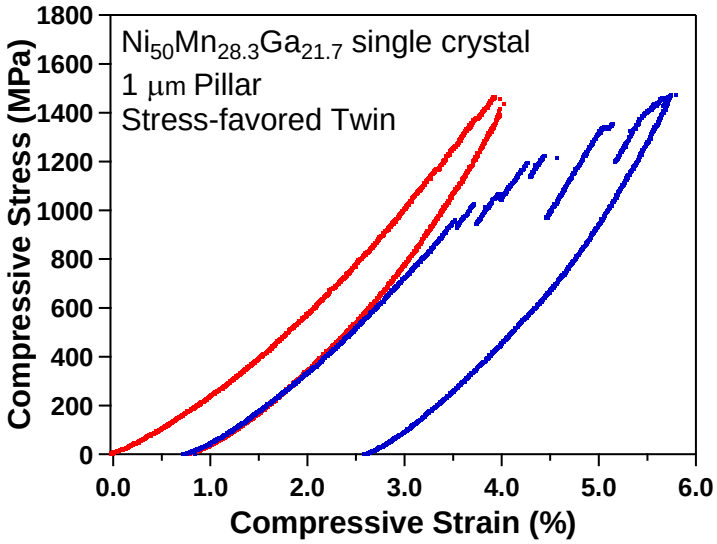

(a)

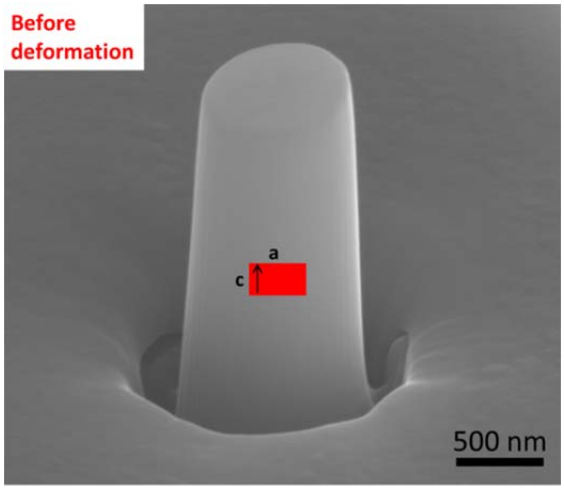

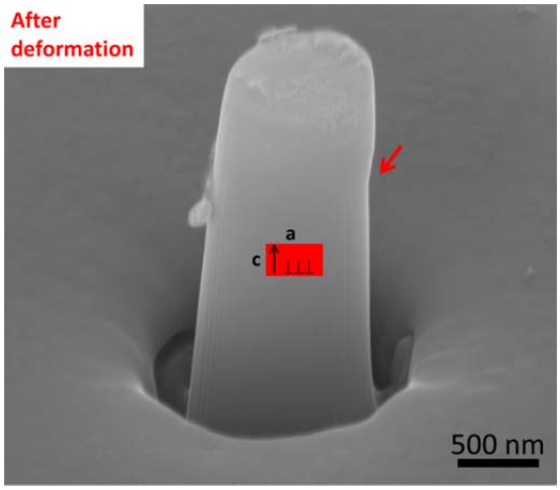

(b) (c)

Figure 5.17 (a) Compressive stress-strain response of the 1 μm $Ni_{50}Mn_{28.3}Ga_{21.7}$ pillar fabricated in the stress-favored twin. The pillar showed plasticity due to deformation of the stress-favored variant. SEM images of this pillar, (b) before deformation, and (c) after deformation. The arrow in (b) points out the kink formation during plastic deformation. Martensite variants were sketched on the pillar images. The residual material on the pillar in (c) comes from the pillar processing with AFM after deformation.

5.6 Summary and Conclusions

In the present work, stress-induced and magnetic field-induced martensite variant reorientation were investigated as a function of the sample size using the $Ni_{50}Mn_{28.3}Ga_{21.7}$ single crystal oriented along the [100] direction of the austenite. This single crystal was in the martensite phase at room temperature, thus, it was no longer a single crystal and was composed of martensite twins. All the experiments on this specimen were carried out at room temperature and in its martensitic state. Observations on the size effects on the martensite variant reorientation were conducted by fabricating micron/submicron pillars in the magnetically-favored twin of the bulk specimen. Experiments investigating the plasticity were performed on the pillars prepared in the stress-favored twin of the bulk sample. The main findings and conclusions can be summarized as follows;

- Martensite variant reorientation is size dependent. As the sample size decreased, the stress required for martensite reorientation (σ_r) increased. The bulk specimen exhibited 1.5 MPa reorientation stress whereas the 20 μm, 10 μm and the 5 μm pillars showed reorientation stresses of 10 MPa, 18 MPa and 40 MPa, respectively.
- Magnetic field-induced martensite variant reorientation was found to be still possible at the 20 μm, 10 μm and the 5 μm pillar sizes even though they exhibited such high martensite reorientation stresses. The bulk $Ni_{50}Mn_{28.3}Ga_{21.7}$ sample had 0.8T saturation magnetic field below which the martensite reorientation of the bulk was observed. On the other hand, 20 μm, 10 μm and the

5 μm pillars started to show martensite reorientation at the magnetic field levels between 2T and 5T. This was attributed to the increase in the saturation magnetic field as the sample size decreased. The increasing saturation field is associated with the increase in the magnetocrystalline anisotropy energy (MAE). We suggest that the increase in the MAE is due to the magneto-microstructural coupling these materials possess. It is expected that the smaller samples exhibit finer twins and thus smaller magnetic domains that couple with them. This results in a harder magnetic switching which in turn gives rise to the increase in MAE.

- 2 μm and 1 μm pillars on the magnetically-favored twin showed superelastic response even though they were fabricated in the martensitic twins. This was attributed to the decrease in the transformation temperatures with the size of the specimen. When the pillar size was 1 μm, the perfect superelastic response with minor residual strain was observed revealing this pillar became completely or mostly austenite phase at room temperature. 630 nm pillar on the same twin showed prominent plastic deformation in addition to some recoverable strain due to possible phase transformation.
- Plastic deformation of the 10 μm and the 1 μm pillars on the stress-favored twin revealed that the stress required for plastic deformation increased as the pillar size decreased.

CHAPTER VI

SIZE EFFECTS IN MAGNETIC FIELD-INDUCED PHASE TRANSFORMATION IN $Ni_{45}Mn_{36.6}Co_5In_{13.4}$ META-MAGNETIC SHAPE MEMORY ALLOYS

6.1 Introduction

In this chapter, the size effects in magnetic field-induced phase transformation was studied using $Ni_{45}Mn_{36.6}Co_5In_{13.4}$ single crystal oriented along the [100] direction of the austenite phase. NiMnCoIn FSMAs show magnetic field-induced martensitic phase transformation (FIPT) due to simultaneous structural and magnetic first order phase transitions and is referred to as meta-magnetic shape memory alloys [2]. After several attempts, on different crystals with different In contents the composition of $Ni_{45}Mn_{36.6}Co_5In_{13.4}$ (at.%) was selected since this composition exhibited paramagnetic martensitic structure at room temperature and transformed into ferromagnetic austenite when magnetic field of 7 Tesla was applied.

Zeeman Energy (ZE) is the magnetic energy responsible for the FIPT in these alloys and it is higher than the MAE; magnetic energy responsible for the field-induced shape change in NiMnGa alloys. The difference in the saturation magnetizations of transforming phases gives the ZE which increases continuously with the field. In addition, ZE is not strongly dependent on the crystal orientation unlike MAE. Therefore, in this mechanism, the magnetic field-induced strain does not have a similar limitation

for the magnetic energy as in the case of the first mechanism (martensite variant reorientation) [2].

In order to investigate the size effects in FIPT, micron and submicron pillars were studied on the $Ni_{45}Mn_{36.6}Co_5In_{13.4}$ single crystals along the [100] orientation of the austenite. The sample was a mixture of martensite and austenite phases at room temperature, thus, it was not a single crystal at this temperature and included martensite twin plates. Micron/submicron pillars with diameters between 10 μm and 500 nm were fabricated on the martensite twins using FIB and deformed by a nanoindenter. Magnetic field of 8 to 12 Tesla was applied to the deformed pillars to investigate the field level at which the recovery is seen in different size pillars. Detailed information on the sample preparation, testing and characterization was given in Chapter III.

The results revealed an increase in the martensite reorientation stress (σ_r) with decreasing sample size. Magnetic field-induced phase transformation was also observed in these sub-micron pillars as seen in their bulk counterparts.

These sets of experiments provided an understanding on the FIPT in sub-micron length scales. There is no report in the literature presenting the size effects in FIPT and therefore this study is expected to bring valuable knowledge for this reversible shape change mechanism in order to be utilized in small scale devices.

6.2 Thermally-induced and Magnetic Field-induced Phase Transformations in Bulk $Ni_{45}Mn_{36.6}Co_5In_{13.4}$

Phase transformation characteristics of the $Ni_{45}Mn_{36.6}Co_5In_{13.4}$ specimen were investigated in order to choose a sample for the pillar fabrication. Figure 6.1 shows the DSC plot of a $Ni_{45}Mn_{36.6}Co_5In_{13.4}$ specimen heat treated at 900 ^oC for 24 hrs and then water quenched. According to the DSC analysis, martensite start (M_s), martensite finish (M_f), austenite start (A_s) and austenite finish (A_f) temperatures were found to be 40 ^oC, 14 ^oC, 36 ^oC and 62 ^oC, respectively.

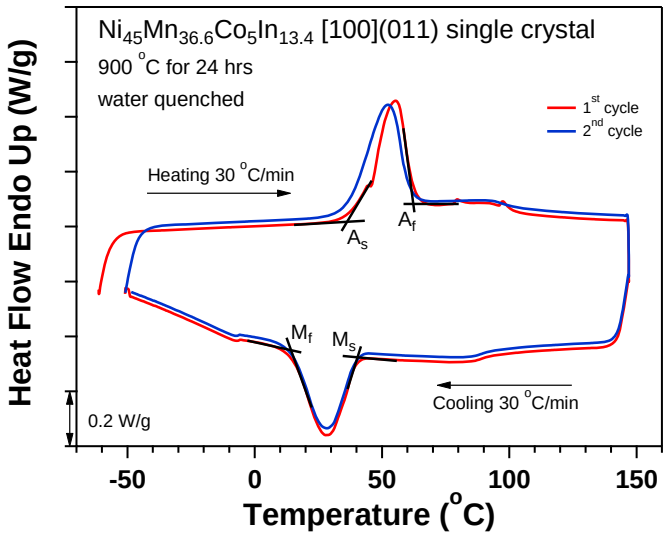

Figure 6.1 Differential scanning calorimetry (DSC) analysis of the $Ni_{45}Mn_{36.6}Co_5In_{13.4}$ single crystal showing martensitic transformation during thermal cycling. The transformation temperatures were found to be martensite start temperature, M_s: 40 ^oC; martensite finish temperature, M_f: 14 ^oC; austenite start temperature, A_s: 36 ^oC; austenite finish temperature, A_f: 62 ^oC.

In Figure 6.2 the thermo-magnetization response of the $Ni_{45}Mn_{36.6}Co_5In_{13.4}$ crystal with the same heat treatment is given. The transformation temperatures under 0.05T field were determined to be M_s: 34 ^oC, M_f: 12 ^oC, A_s: 21 ^oC, A_f: 53 ^oC. These temperatures somewhat vary from the transformation temperatures found in Figure 6.1. This difference is expected since the samples used for the DSC and the SQUID analyses were cut from the different regions of the as-received specimen and in different sizes. Due to the slight differences in their initial compositions and the insuppressible In and Mn evaporation during heat treatment, they can end up having slightly different transformation temperatures.

After many combinations of the heat treatments in vacuum and Ar environments followed by water quenching, oil quenching or furnace cooling, the bulk sample slice identical to the sample used in Figure 6.2 was found to have the most promising properties for the pillar fabrication. An image of the bulk sample slice used to machine the pillars from is shown in Figure 6.3. This NiMnCoIn specimen is a mixture of austenite and martensite at room temperature and has large martensite twin plates to use for pillar fabrication. The advantage of having a microstructure consisting of both phases is that it can fully transform to austenite structure when 7T field is applied as shown in Figure 6.2. FIPT can therefore be investigated also in micropillars fabricated from this specimen.

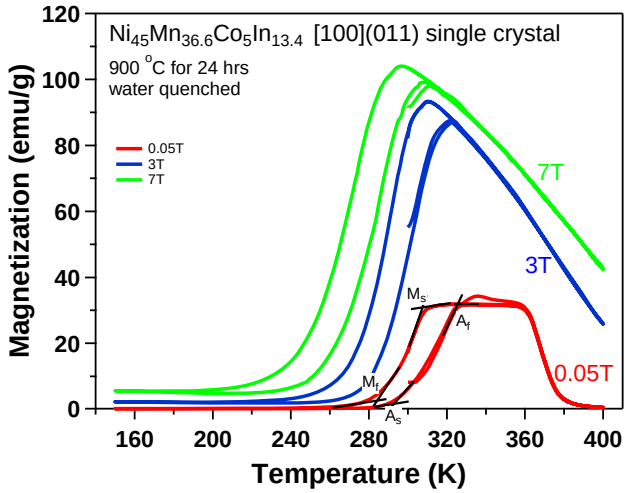

Figure 6.2 SQUID analysis showing the thermo-magnetization response of the $Ni_{45}Mn_{36.6}Co_5In_{13.4}$ single crystal at 0.05T, 3T and 7T magnetic fields. At room temperature (300K), the sample is a mixture of austenite and martensite. When 7T field is applied, all the martensite transforms into austenite due to FIPT and the sample becomes completely austenite phase. The transformation temperatures at a negligible field (0.05T) are as follows; martensite start temperature, M_s: 34 ^oC; martensite finish temperature, M_f: 12 ^oC; austenite start temperature, A_s: 21 ^oC; austenite finish temperature, A_f: 53 ^oC.

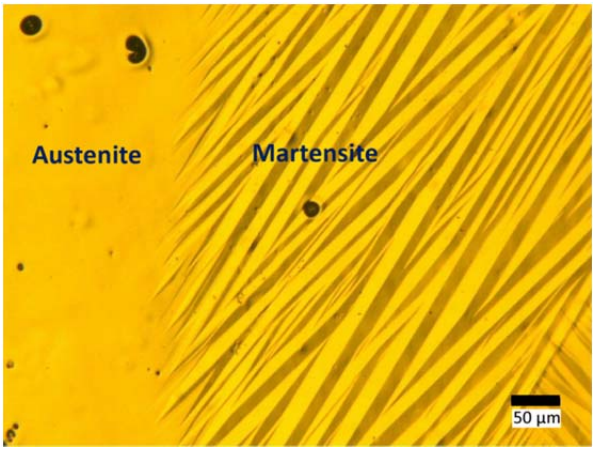

Figure 6.3 Optical microscopy image of the $Ni_{45}Mn_{36.6}Co_5In_{13.4}$ sample used to fabricate the micron and sub-micron size pillars. The sample consists of austenite and martensite phases at room temperature. Pillars were machined on the martensite twin plates of this specimen using FIB.

6.3 Stress-induced Martensite Variant Reorientation and Magnetic Field-induced Phase Transformation in $Ni_{45}Mn_{36.6}Co_5In_{13.4}$ Micropillars

Micropillars with the diameters of 10 μm, 5 μm and 1 μm were studied in order to investigate the size effects in the martensite variant reorientation and the magnetic field-induced phase transformation in $Ni_{45}Mn_{36.6}Co_5In_{13.4}$ meta-magnetic SMAs. Figure 6.4(a) shows an example of the typical micropillars machined on the same martensite twins. Since the pillars with the 1 μm and smaller diameters exhibited plastic deformation rather than the martensite variant reorientation, these pillars will be discussed in the next section. The stress and magnetic field application directions were illustrated on a micropillar in Figure 6.4(b). First the pillars were compressed and then the magnetic field was applied to them. As mentioned previously, the direction of the magnetic field is not important for the magnetic field-induced phase transformation mechanism. Therefore, the field direction in Figure 6.4(b) was randomly selected considering the convenience of attaching the sample to the holder without damaging the pillars.

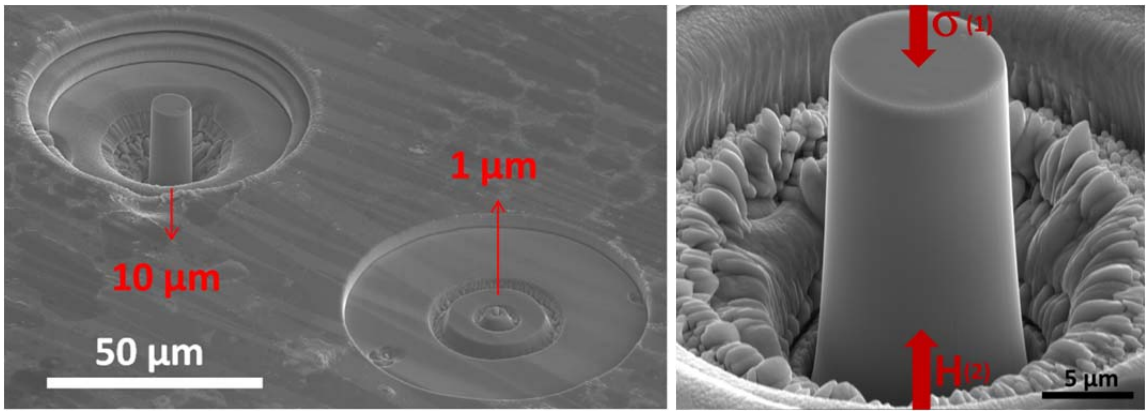

(a) (b)

Figure 6.4 (a) Compression pillars in 10 µm and 1 µm diameters fabricated on the same martensite plate of the $Ni_{45}Mn_{36.6}Co_5In_{13.4}$ sample. (b) An image of a 10 µm pillar on the $Ni_{45}Mn_{36.6}Co_5In_{13.4}$ specimen showing the stress (σ) and magnetic field (H) application directions on the pillar.

Figure 6.5 presents the findings of a 10 µm pillar. The pillar consists of two martensite plates observed as the light and the dark contrast on the pillar top surface in Figure 6.5(a). The stress-strain response of this pillar is given in Figure 6.5(b). The martensite reorientation started at around 24 MPa where the plateau region appeared. The stress plateau seemed to be very flat and only reached 25.5 MPa during the entire martensite propagation process. Post-deformation image of this pillar is presented in Figure 6.5(c). It is clear that the entire height of the pillar was deformed.

8T magnetic field was applied to this pillar after deformation. Since the bulk $Ni_{45}Mn_{36.6}Co_5In_{13.4}$ transformed into fully austenite at 7T (Figure 6.2), 8T field is a reasonable field level for investigating the FIPT in the micropillars if the slight compositional changes are considered. Figure 6.5(d) shows the image of the pillar after

application of 8T field. The surface of the pillar is different than what was observed after deformation (Figure 6.5(c)). It is obvious that this martensitic pillar transformed into austenite upon application of the magnetic field and then transformed back to martensite when the field was removed since the martensite is the stable phase at room temperature in this pillar under zero field. The new martensite twins formed in the self-accommodated morphology, thus, revealed a different twin distribution from that seen in the post-deformation image. Due to FIPT, the recovery of the pillar was also obtained. This is clearly seen when Figures 6.5(c) and (d), taken from the same tilt angle, are compared. The dashed lines in the backgrounds of these figures refer to the same reference points. While the pillar height is shorter than the level of this line in Figure 6.5(c), the pillar height increased after application of 8T in Figure 6.5(d) and became higher than the level of the dashed line. This again shows that the FIPT took place in this pillar at 8T and resulted in the recovery of the deformed pillar.

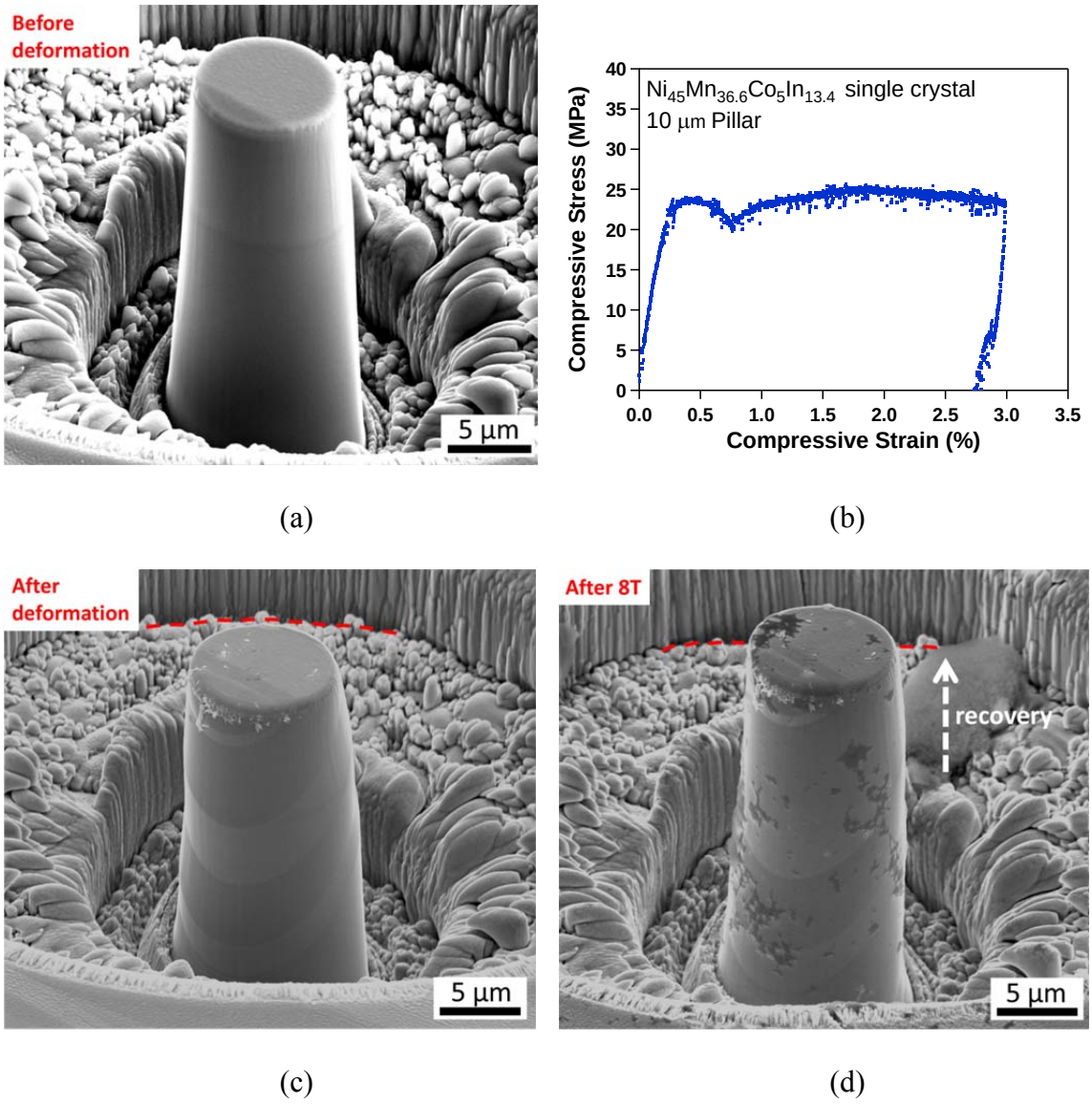

Figure 6.5 (a) A 10 μm pillar fabricated on the martensite twins of the $Ni_{45}Mn_{36.6}Co_5In_{13.4}$ specimen which is a single crystal when in austenite phase. The pillar consists of two martensite plates. (b) Compressive stress-strain response of the 10 μm pillar in (a). The compression (longitudinal) axis of the pillar is oriented along the [100] direction of the austenite. (c) Post-deformation SEM image of the pillar. (d) SEM image of the pillar after application of 8T magnetic field showing recovery due to FIPT occurring in the pillar.

Another 10 μm pillar results are given in Figure 6.6. This pillar consists of only one martensite twin and thus is a single crystal as seen in Figure 6.6(a). The martensite reorientation response of this pillar showed an onset of reorientation stress plateau at 28 MPa (Figure 6.6(b)). The formation of the stress-induced twins on the pillar surface is observed in the post-deformation image in Figure 6.6(c). After deformation, the top surface of the pillar was not flat due to the formation of two twin plates, i.e. the v-shaped surface relief formed on the pillar top surface. 12T magnetic field was applied to this pillar since some local compositional differences were realized on the bulk specimen and some of the pillars did not exhibit complete phase transformation upon application of 8T field. After 12T was applied, the pillar reached its self-accommodated morphology as seen in Figure 6.6(d). The shape of the pillar after application of 12T was completely different than that of the pillar after deformation. This shows that the pillar had martensite to austenite phase transformation when 12T was applied and it transformed back to martensite when the field was removed since the martensite is the stable phase at room temperature in this pillar. As a result, self-accommodated martensitic structure was observed. Figures (e) and (f) show the images of this pillar from a different tilt angle after deformation and 12T field application, respectively. The images taken from the other side of this pillar were also given in Figures (g) and (h) for after deformation and application of 12T field, respectively. Formation of fine twins at the bottom of the pillar and the change in the shape of the pillar due to self-accommodation are clearly seen in (h).

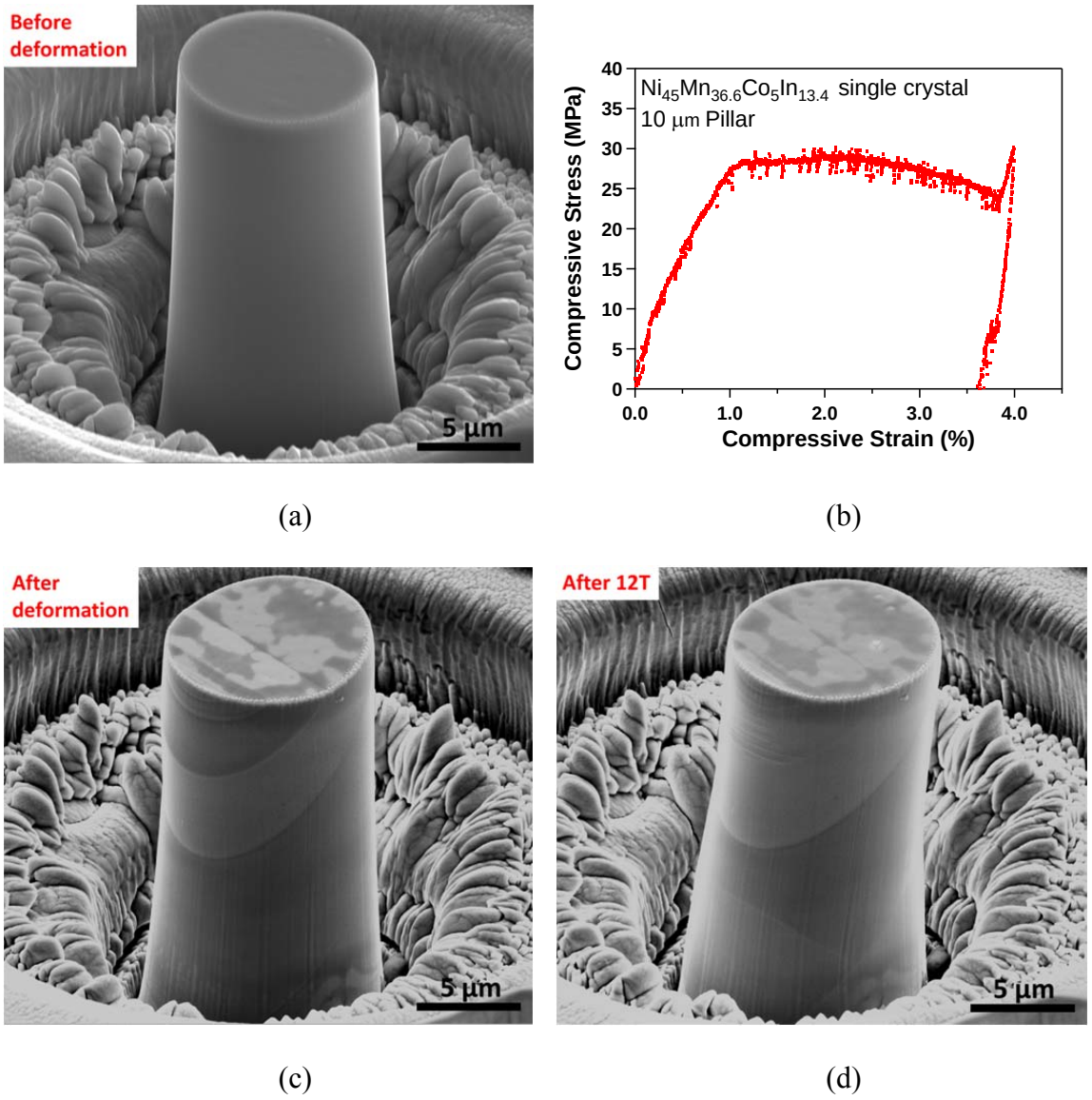

Figure 6.6 (a) A single crystalline 10 μm pillar fabricated on a martensite twin of the $Ni_{45}Mn_{36.6}Co_5In_{13.4}$ specimen. (b) Compressive stress-strain response of the 10 μm pillar in (a). The compression (longitudinal) axis of the pillar is oriented along the [100] direction of the austenite. (c) Post-deformation SEM image of the pillar. (d) SEM image of the pillar after application of 12T magnetic field taken from the same tilt angle of 52 ^{o}C in (c). SEM images of the pillar, (e) after deformation and (f) after application of 12T field taken using the same tilt angle of 30^{o}. SEM images, (g) of the back side of the pillar after deformation and (h) after 12T field taken from the same tilt angle of 30^{o}. Due to self-accommodated martensite formation, the shape of the pillar changed after 12T field application as is seen when (c) and (d), (e) and (f), (g) and (h) are compared.

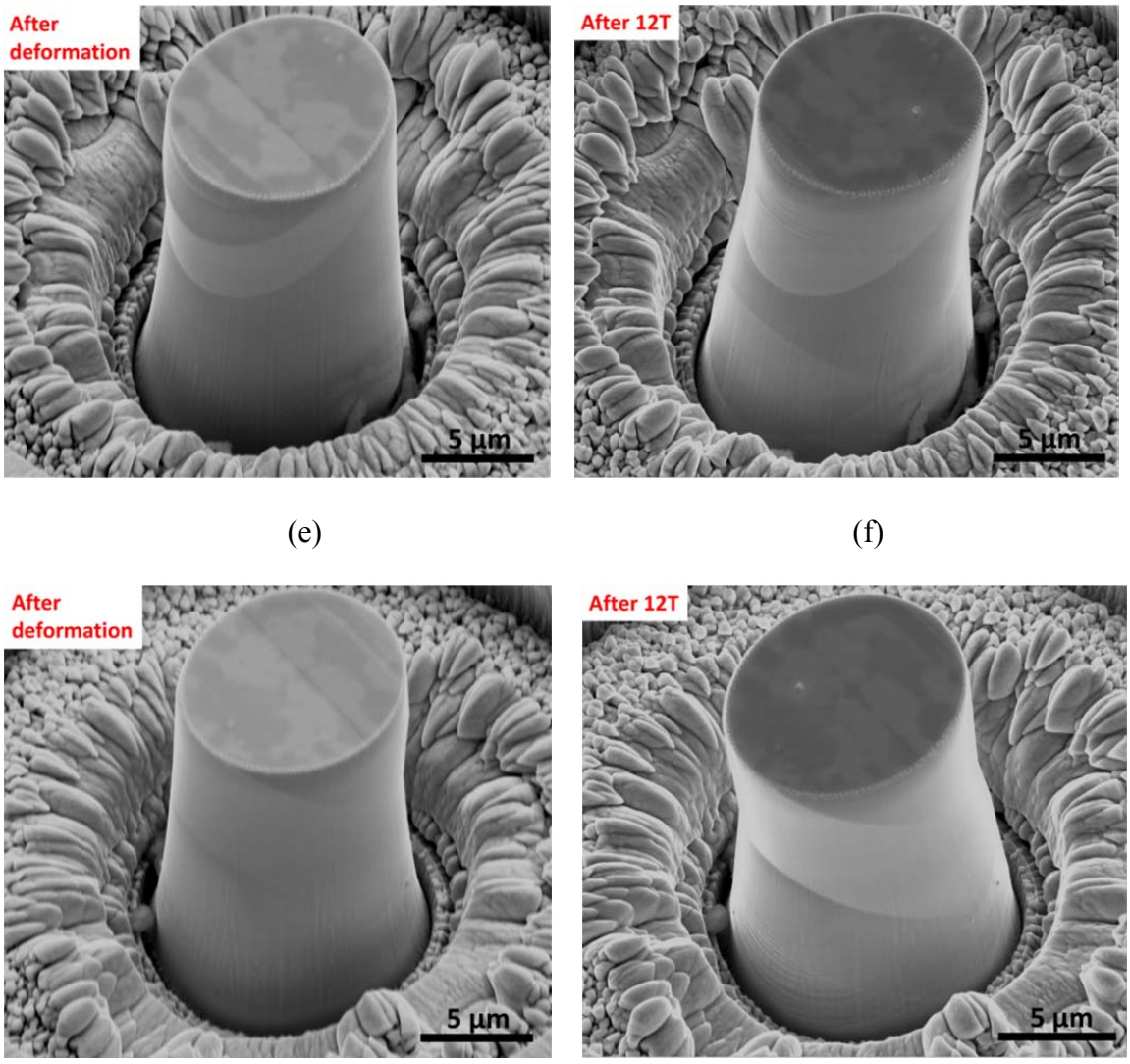

Figure 6.6 Continued.

Another 10 µm pillar is presented in Figure 6.7. This pillar is a single crystalline pillar prepared on a single martensite twin (Figure 6.7(a)). This pillar had an onset of the martensite reorientation stress of 20MPa where the plateau region started to appear (Figure 6.7(b)). The stress-strain plot revealed local increases in the stress level followed

by a plateau region as the deformation proceeded. This indicates the nucleation of a different martensite twin once the propagation of the previously formed twin was interrupted. Figures 6.7(c) and (d) shows the images of this pillar after deformation. Stress-induced martensite twins were observed on the pillar surface. When 8T field was applied to this pillar, this pillar experienced a partial FIPT. This conclusion was made because the pillar did reach its self-accommodated morphology and the upper section of it was not affected by the field as seen in Figure 6.7(e). However, there were some changes in the twin morphology on the pillar surface which indicated the partial FIPT and thus partial recovery of the pillar. 12T field was also applied after the 8T. Figure 6.7(f) reveals that additional changes occurred in the twins on the pillar surface upon application of 12T. This is again due to FIPT taking place in the pillar. However, it seems like this pillar only had a partial FIPT most probably due to slightly lower In content and higher transformation temperatures at that particular sample location where the pillar was fabricated.

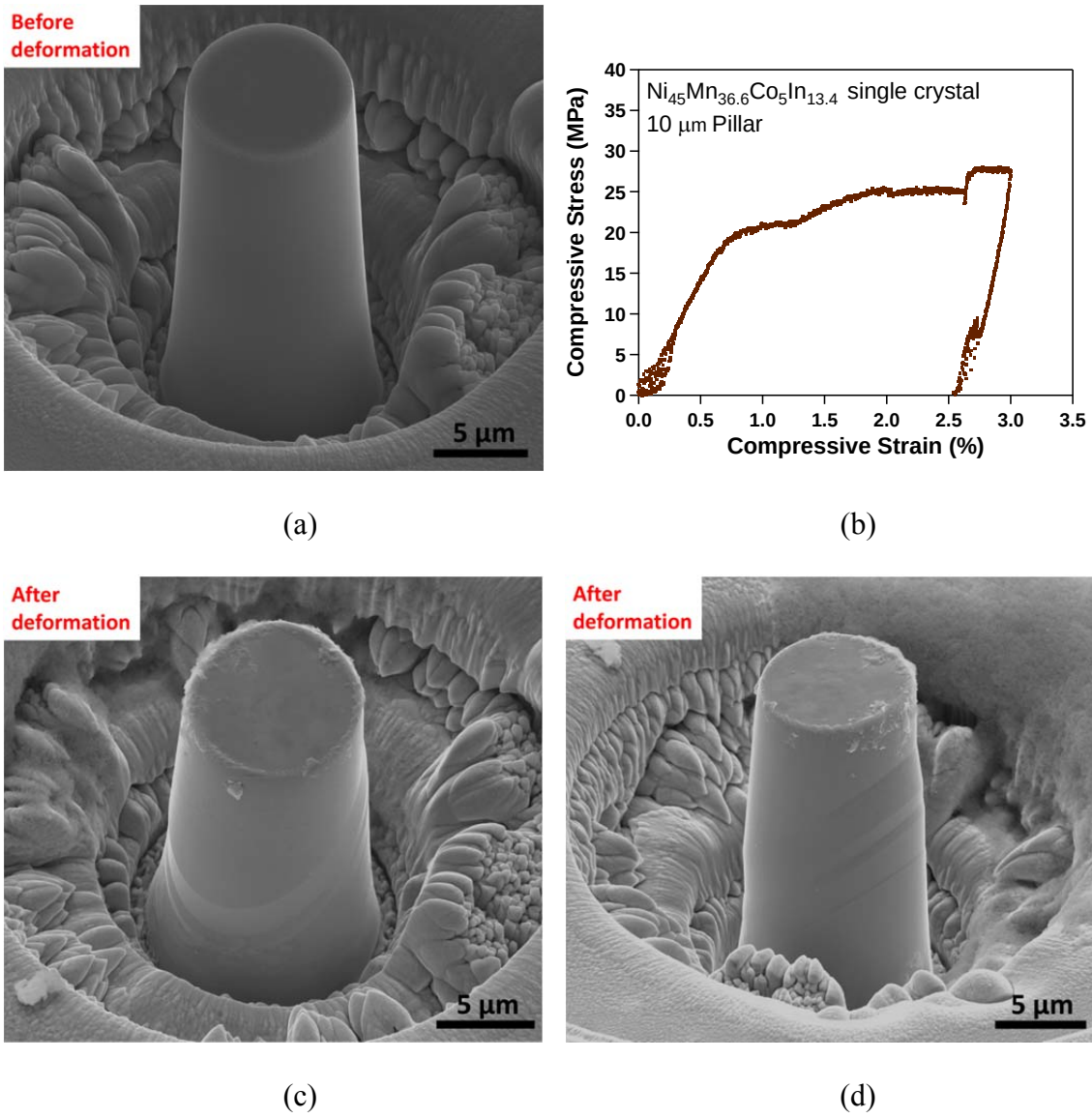

Figure 6.7 (a) A single crystalline 10 µm pillar fabricated on a martensite twin of the $Ni_{45}Mn_{36.6}Co_5In_{13.4}$ specimen. (b) Compressive stress-strain response of the 10 µm pillar in (a). The compression (longitudinal) axis of the pillar is oriented along the [100] direction of the austenite. Post-deformation SEM images taken, (c) from 30^o and, (d) from 52 ^{o}C tilt angle. SEM images of the pillar, (e) after application of 8T and, (f) after application of 12T field taken using the same tilt angle of 52^o.

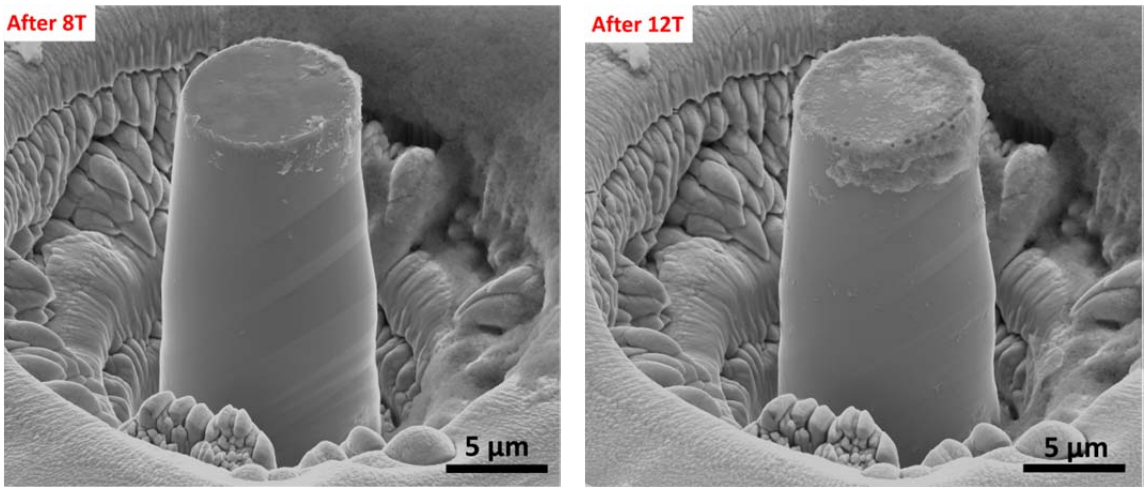

(e) (f)

Figure 6.7 Continued.

Figure 6.8 shows another example for the 10 µm pillars prepared on a single twin of the $Ni_{45}Mn_{36.6}Co_5In_{13.4}$ specimen. In the pre-deformation SEM image of the pillar (Figure 6.8(a)), there is no existing twin boundary, which confirms that the pillar is a single crystal. The stress-strain response of the pillar in Figure 6.8(b) reveals that a plateau was reached at around 22 MPa and then a rapid stress increase was observed followed by another plateau region at around 28 MPa. As mentioned earlier, this is because of the difficult propagation of the martensite twins due to the surface effects and continuous generation of other twins as a result of further loading. Figure 6.8(c) is the image of the pillar after deformation showing stress-induced martensite twins formed due to martensite reorientation. When 12T field was applied to the deformed pillar, FIPT took place which was observed as the different twin morphology on the pillar surface

(Figure 6.8(d)). Figures 6.8(e) and (f) show the other side of the pillar after deformation and 12T field application. It is clear that the twin morphology completely changed after 12T and the pillar became a self-accommodated martensite. Self-accommodation is realized especially when the figures (e) and (f) are compared. This confirms the presence of the FIPT in the pillar at 12T and therefore the recovery after deformation.

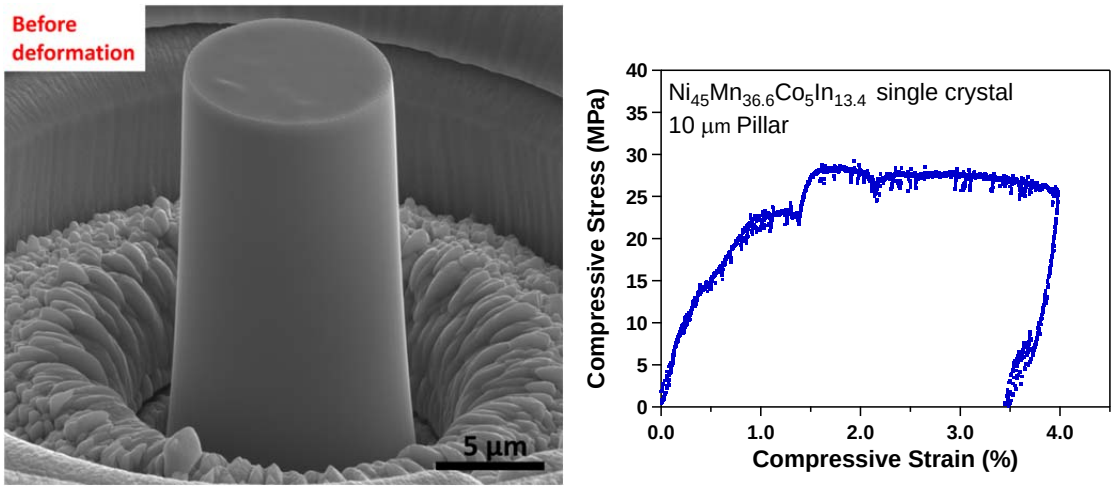

(a) (b)

Figure 6.8 (a) A single crystalline 10 μm pillar fabricated on a martensite twin of the $Ni_{45}Mn_{36.6}Co_5In_{13.4}$ specimen. (b) Compressive stress-strain response of the 10 μm pillar in (a). The compression (longitudinal) axis of the pillar is oriented along the [100] direction of the austenite. SEM images of this pillar, (c) after deformation and, (d) after application of 12T field taken from 52 ^{o}C tilt angle. SEM images of the pillar taken, (e) after deformation and, (f) after application of 12T field using the same tilt angle of 30^{o}. Due to self-accommodated martensite formation, the shape of the pillar changed after 12T field application as is seen when (c) and (d), (e) and (f) are compared.

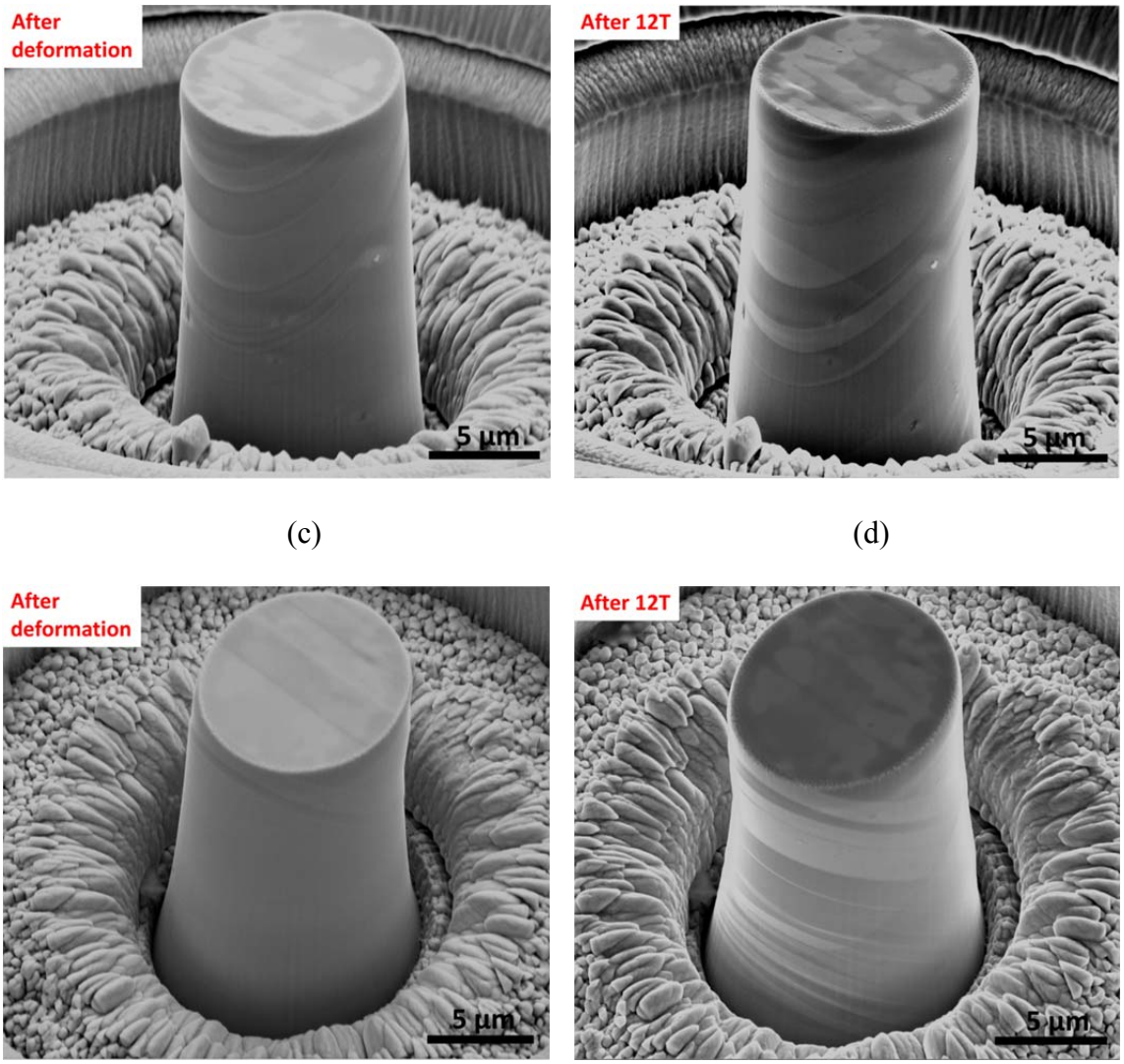

Figure 6.8 Continued.

Figure 6.9 compares all the 10 µm pillars on the $Ni_{45}Mn_{36.6}Co_5In_{13.4}$ specimen. These pillars were fabricated on various martensite plates as single crystalline pillars and also pillars consisted of two martensite plates. Martensite variant reorientation took place at a plateau stress of between 20 MPa and 28 MPa for all the 10 µm pillars tested.

Within this stress range, the tests seem to be consistent which indicated that there is no significant plateau stress level differential for various martensite plates at the 10 μm size.

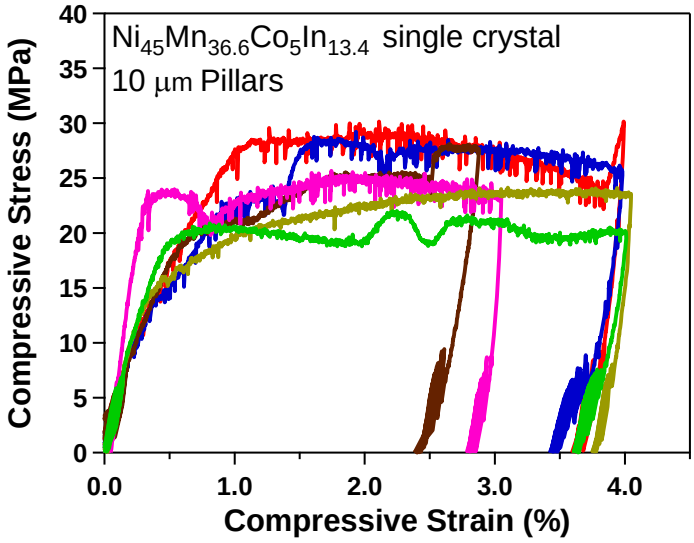

Figure 6.9 Martensite reorientation responses of the 10 μm $Ni_{45}Mn_{36.6}Co_5In_{13.4}$ pillars.

Additionally, 8 MPa plateau stress difference during pillar testing is considered to be repeatable and might simply be coming from the pillars being made from different martensite twins and at different sample locations.

5 μm pillar size was also studied in order to make comparisons with the previous 10 μm pillar results. Figure 6.10(a) shows a single crystalline 5 μm pillar on the $Ni_{45}Mn_{36.6}Co_5In_{13.4}$ specimen. This pillar exhibited a martensite reorientation stress of 40 MPa as seen in the stress-strain response in Figure 6.10(b). After the pillar was deformed, stress-induced martensite twins were formed on the pillar surface (Figure 6.10(c)). When 12T magnetic field was applied, FIPT occurred in the pillar which was observed as the self-accommodated martensitic pillar morphology in Figure 6.10(d). When Figures 6.10(e) and (f) are compared, the formation of the martensite twins as surface relieves is seen after 12T field in the non-deformed bulk surrounding material of the pillar. This is due to the magnetic field-induced martensite to austenite phase transformation and then back transformation to martensite upon removal of the field. These findings clearly reveal that the pillar and its surrounding showed the FIPT.

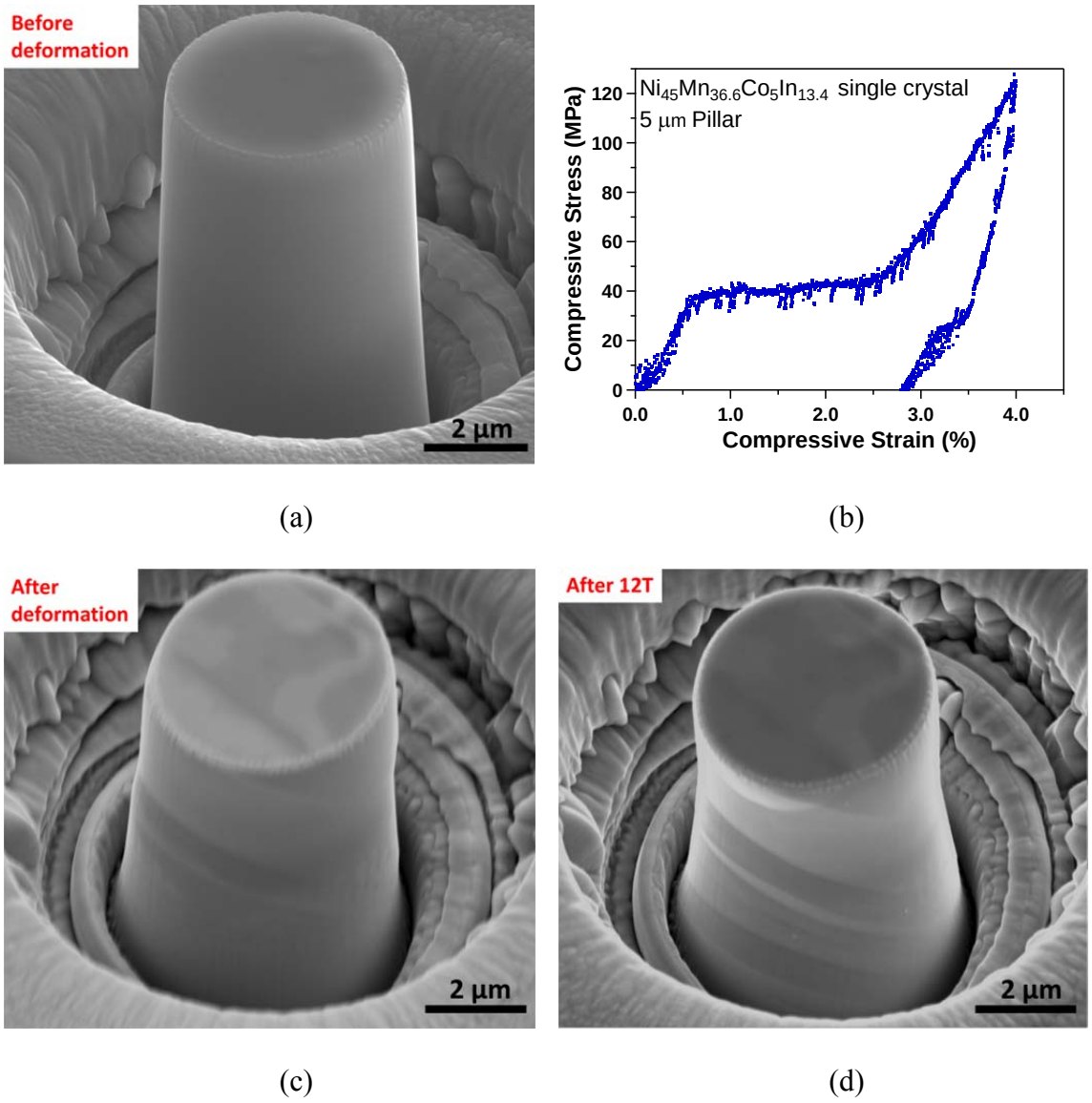

Figure 6.10 (a) A single crystalline 5 µm pillar fabricated on a martensite twin of the $Ni_{45}Mn_{36.6}Co_5In_{13.4}$ specimen. (b) Compressive stress-strain response of the 5 µm pillar in (a). The compression (longitudinal) axis of the pillar is oriented along the [100] direction of the austenite. SEM images of this pillar, (c) after deformation and, (d) after application of 12T field taken from 30 ^{o}C tilt angle. SEM images of the pillar taken, (e) before deformation and, (f) after application of 12T field. FIPT was obtained when 12T field was applied leaving the self-accommodated martensite twins as surface relives upon removal of the field. Due to self-accommodated martensite formation, the shape of the pillar changed after FIPT as is seen when (c) and (d) are compared.

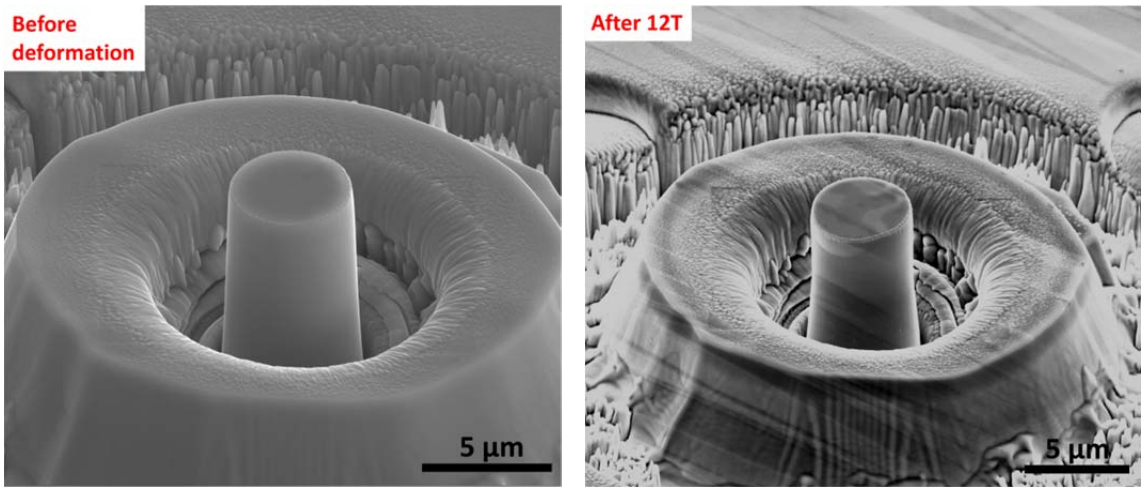

(e) (f)

Figure 6.10 Continued.

Figure 6.11 compares all the 5 µm pillars on the $Ni_{45}Mn_{36.6}Co_5In_{13.4}$ bulk specimen. The stresses at the onset of martensite reorientation range between 40 MPa and 50 MPa whereas the higher plateau stresses were reached as the martensite twin formation and propagation proceeded in plots (B) and (C). Post-deformation SEM images of these 5 µm pillars are also shown in the figure. Easier propagation of the martensite twins in (A) is realized from the completely flat stress-strain response of the pillar and its image after deformation showing a relatively homogeneous deformation throughout the pillar height.

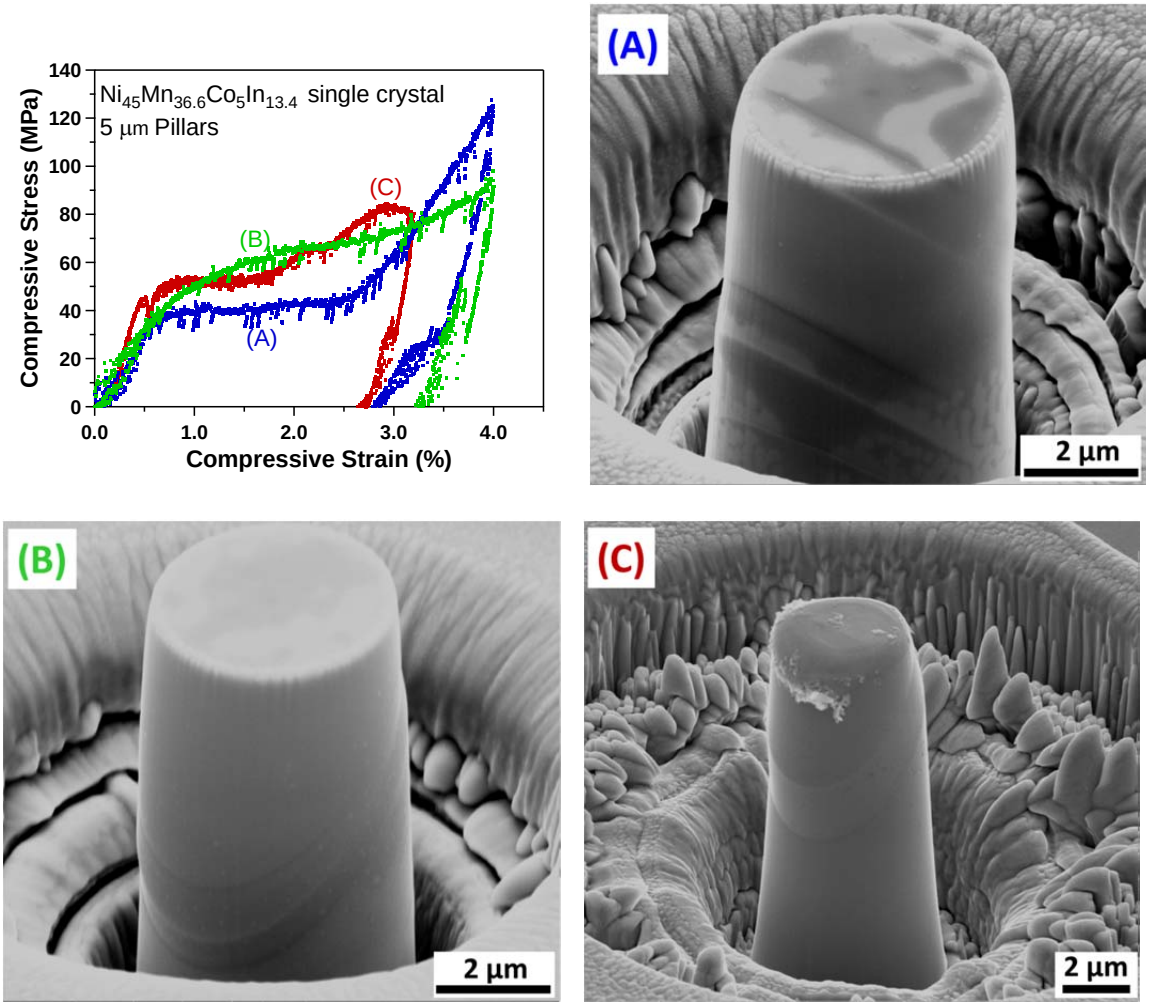

Figure 6.11 Martensite reorientation responses of the 5 μm $Ni_{45}Mn_{36.6}Co_5In_{13.4}$ pillars and their images after deformation. Post-deformation SEM images marked as (A), (B) and (C) are corresponding to the stress-strain responses of (A), (B) and (C).

The 10 μm and the 5 μm pillars on the $Ni_{45}Mn_{36.6}Co_5In_{13.4}$ bulk sample showed different martensite variant reorientation stresses. Figure 6.12 compares the stress levels for these two sizes. The 5 μm pillar with the lowest martensite reorientation stress was plotted together with some of the 10 μm pillar results. It is clear that the martensite reorientation stress is size dependent and increases as the size of the specimen decreases.

The same trend and similar stress values were observed for the same size NiMnGa pillars in Chapter V. According to the best of our knowledge, the size effect in martensite variant reorientation has never been reported previously. Therefore, these findings provide an understanding on the martensite reorientation response in sub-micron length scales. Additionally, the shape change due to magnetic field-induced phase transformation was shown to be possible down to 5 μm size scale for the first time with no significant size effect on the required magnetic field levels.

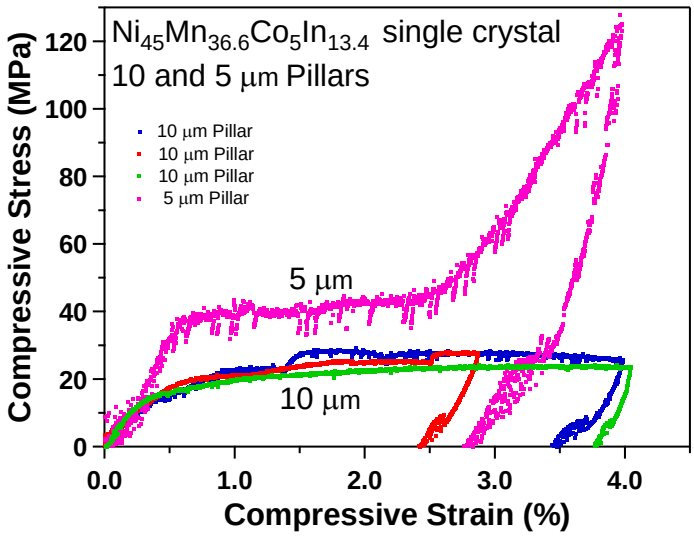

Figure 6.12 Comparison of the martensite reorientation stresses of the 10 μm and 5 μm $Ni_{45}Mn_{36.6}Co_5In_{13.4}$ pillars.

6.4 Mechanical Response of $Ni_{45}Mn_{36.6}Co_5In_{13.4}$ Pillars ≤ 1 μm Size

1 μm and smaller single crystalline pillars were also investigated using the $Ni_{45}Mn_{36.6}Co_5In_{13.4}$ specimen. Figure 6.13(a) shows a 1 μm pillar on a martensite twin of this bulk specimen. When the pillar was deformed, the yielding started to take place at around 1730 MPa and a stress plateau was reached at 2275 MPa (Figure 6.13(b)). The high stress level and the shape of the stress-strain response of this pillar indicated the existence of the plastic deformation.

Figure 6.13(c) shows the image of this pillar after deformation. The pillar had a mushroom-shaped permanent deformation at the top part. This was due to the very high stress levels reached at the top of the pillar since the pillars are slightly tapered and the top diameter is the smallest section and thus experiences the largest stress. Additionally, some striations formed on the top of the pillar after deformation. These are indicative of microstructural events taking place due to either twinning or dislocation plasticity and appeared as stress drops at the onset of yielding and during the plateau region in (b). Figure 6.12(c) also reveals some color contrast on the pillar surface. More than half length of the pillar towards the top was deformed and appeared in light contrast whereas the bottom part of the pillar was in dark contrast. After deformation, 12T magnetic field was applied to the pillar to study if there are any noticeable changes in the pillar caused by FIPT. As seen in Figure 6.13(d), the plastically deformed top part of the pillar remained the same after 12T field. However, the bottom section of the pillar where it connects to its substrate material got slightly bent. This suggests that the FIPT still took place in the part of the 1 μm pillar where there was not any plastic deformation involved.

The drop in the martensitic transformation temperatures is expected with the reduction in the sample size. At 1 μm size, the pillars might also have become partially austenite and thus the plastic deformation in Figure 6.13(b) may exhibit the plasticity in austenite as well as in martensite. In addition, it was clear from the SEM pictures that the FIPT occurred in the surrounding bulk material next to the pillar, confirming that the pillar was fabricated on a martensite phase at room temperature.

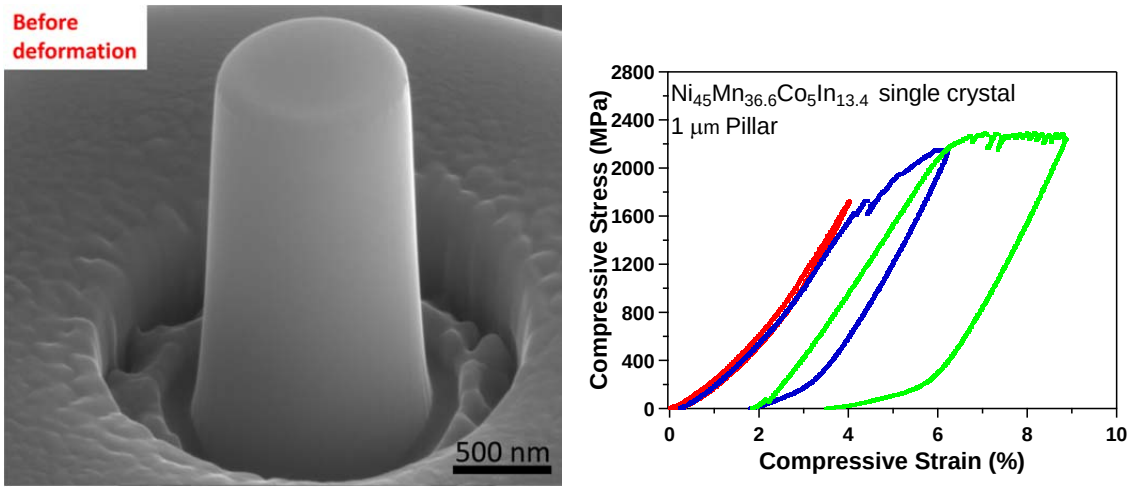

(a) (b)

Figure 6.13 (a) A single crystalline 1 μm pillar fabricated on a martensite twin of the $Ni_{45}Mn_{36.6}Co_5In_{13.4}$ specimen. (b) Compressive stress-strain response of the 1 μm pillar in (a). The compression (longitudinal) axis of the pillar is oriented along the [100] direction of the austenite. SEM images of this pillar, (c) after deformation and, (d) after application of 12T field.

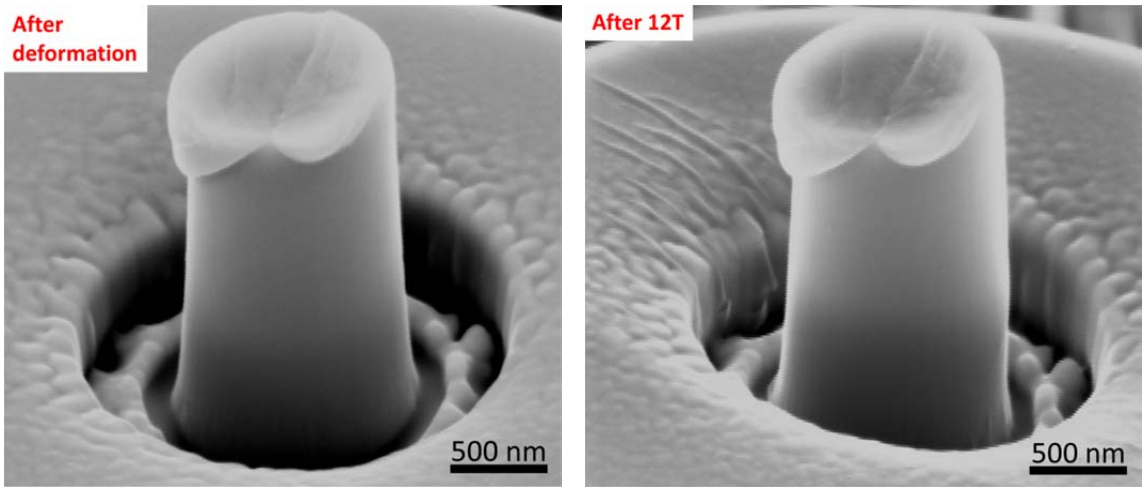

(c) (d)

Figure 6.13 Continued.

The findings for another 1 μm pillar were given in Figure 6.14. Figure 6.14(a) shows the stress-strain response of this 1 μm pillar in Figure 6.14(b). The yielding of the pillar started at around 1820 MPa followed by a stress plateau with some hardening associated at above 2000 MPa. Abrupt stress drops in the stress-strain response are due to large displacement changes because of defect generation in the perfect single crystal of such small size. Upon unloading from 10% strain, 5% deformation remained on the

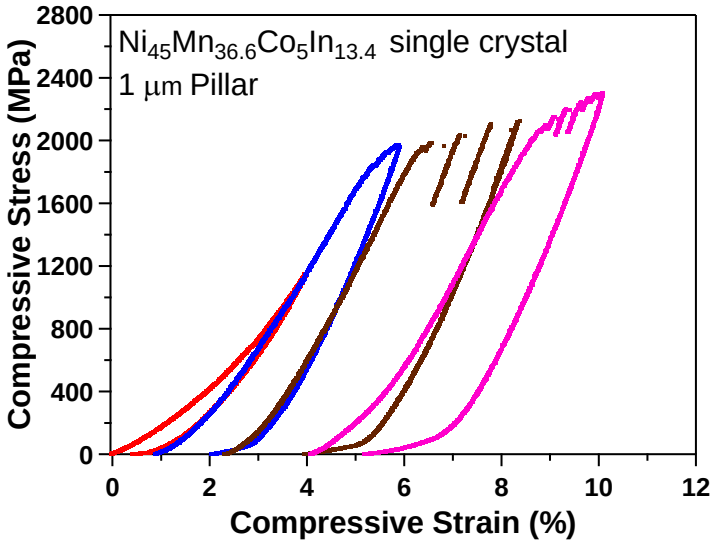

(a)

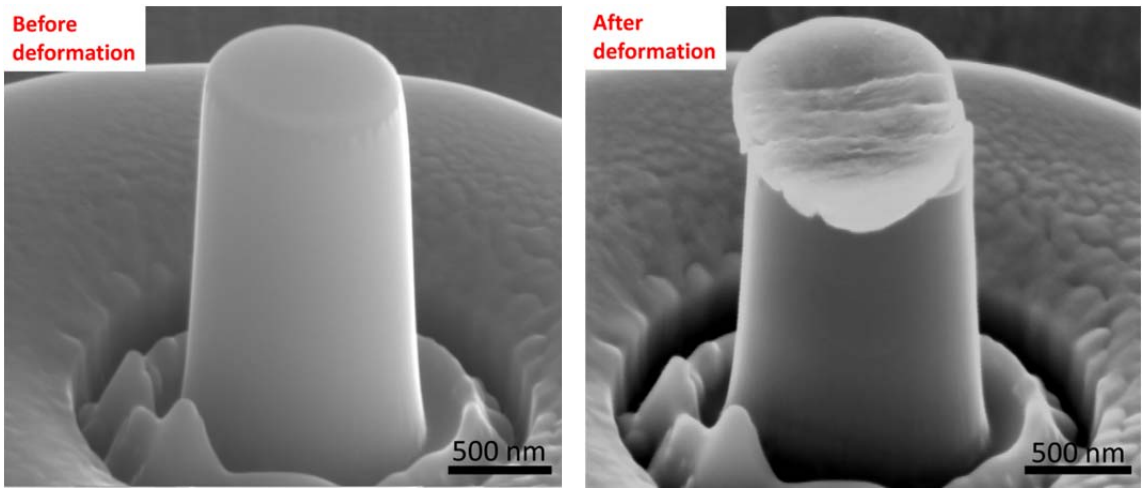

(b) (c)

Figure 6.14 (a) Compressive stress-strain response of a single crystalline 1 μm pillar fabricated on a martensite twin of the $Ni_{45}Mn_{36.6}Co_5In_{13.4}$ specimen. The compression (longitudinal) axis of the pillar is oriented along the [100] direction of the austenite. SEM images of this pillar, (b) before deformation and, (c) after deformation.

pillar. The residual deformation of the pillar is seen in Figure 6.14(c) as the heavily deformed top surface of the pillar. Additionally, the striations formed on the top pillar surface, which are responsible from the rapid stress drops in the stress-strain response.

Figure 6.15 includes the results for another $Ni_{45}Mn_{36.6}Co_5In_{13.4}$ pillar with 1 μm diameter. The stress-strain response of this pillar in Figure 6.15(a), shows an onset of yielding at 1335 MPa with a sudden stress drop. Then, the further pillar deformation revealed another very large stress drop, 650 MPa in magnitude, at the beginning of the 4^{th} cycle right before the 2000 MPa stress plateau was reached. SEM images of this pillar before and after deformation are shown in Figure 6.15(b) and (c). After deformation, the top surface of the pillar had wavy striations as seen in the previous 1 μm $Ni_{45}Mn_{36.6}Co_5In_{13.4}$ pillars. These striations are related to the deformation mechanism leading to the plasticity of the pillar. In this case, the plasticity might be governed by the twinning or dislocation plasticity. When compared with those previous 1 μm pillars, this pillar revealed more homogeneous deformation since there is no localized plasticity such as bulged material at the top surface of the pillar.

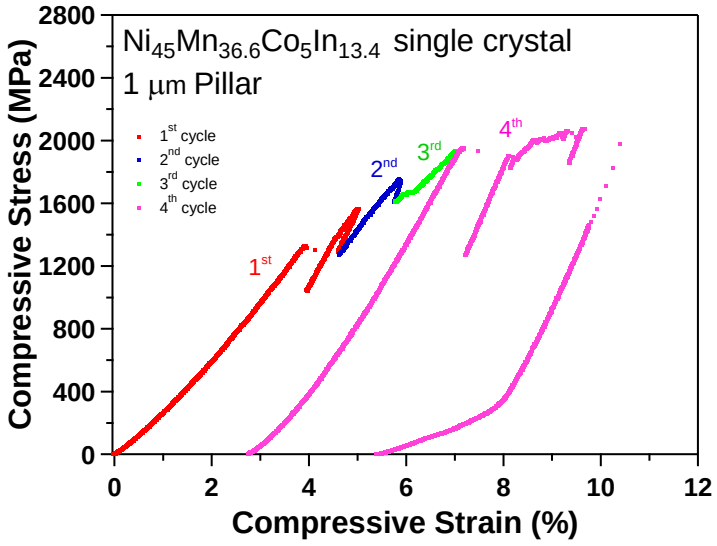

(a)

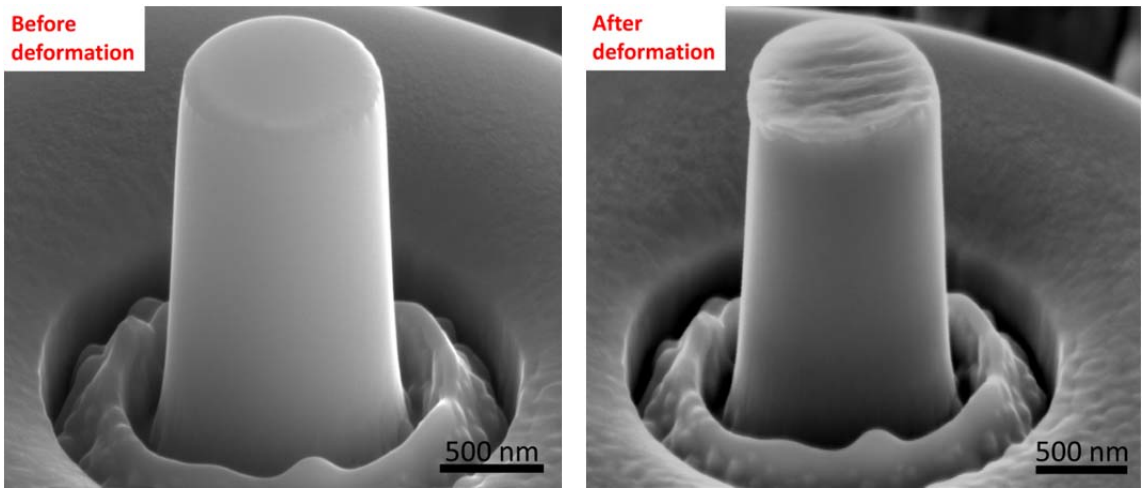

(b) (c)

Figure 6.15 (a) Compressive stress-strain response of a single crystalline 1 μm pillar fabricated on a martensite twin of the $Ni_{45}Mn_{36.6}Co_5In_{13.4}$ specimen. The compression (longitudinal) axis of the pillar is oriented along the [100] direction of the austenite. Unloading curves of the 1st, 2nd and the 3rd cycles are deleted for clarity. SEM images of this pillar, (b) before deformation and, (c) after deformation.

The smallest pillar size studied on the $Ni_{45}Mn_{36.6}Co_5In_{13.4}$ sample was 590 nm in diameter. The stress-strain plot of the pillar (Figure 6.16(a)) showed a similar response to the 1 μm pillars. The pillar was plastically deformed with the onset of yielding at around 1760 MPa. The sudden stress drop at the onset of yielding was followed by the stress plateau at around 2000 MPa. Since there were three loading/unloading cycles during the entire deformation process, the contact made with the top surface of the pre-deformed pillar and that of the deformed pillar were different each time the test was started in such a small length scale. As a result, some inconsistencies in the plateau stress values are seen in Figure 6.16(a), especially between the second and the third cycles. Figure 6.16(b) and (c) show the images of this 590 nm pillar before and after deformation. After deformation, the localized plastic deformation on the top of the pillar was observed, which is very similar to the 1 μm pillar in Figure 6.13(d). Since the pillar is slightly tapered leading to a smaller cross section at the top section, it is expected to see the deformation first at the top and then towards the bottom part.

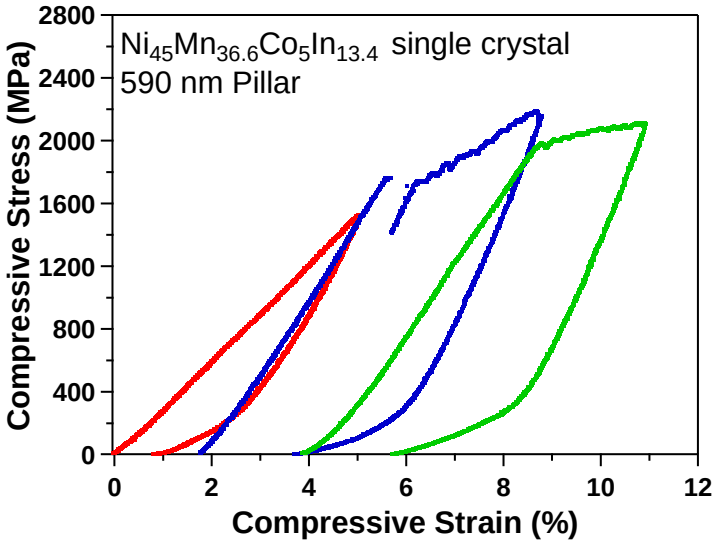

(a)

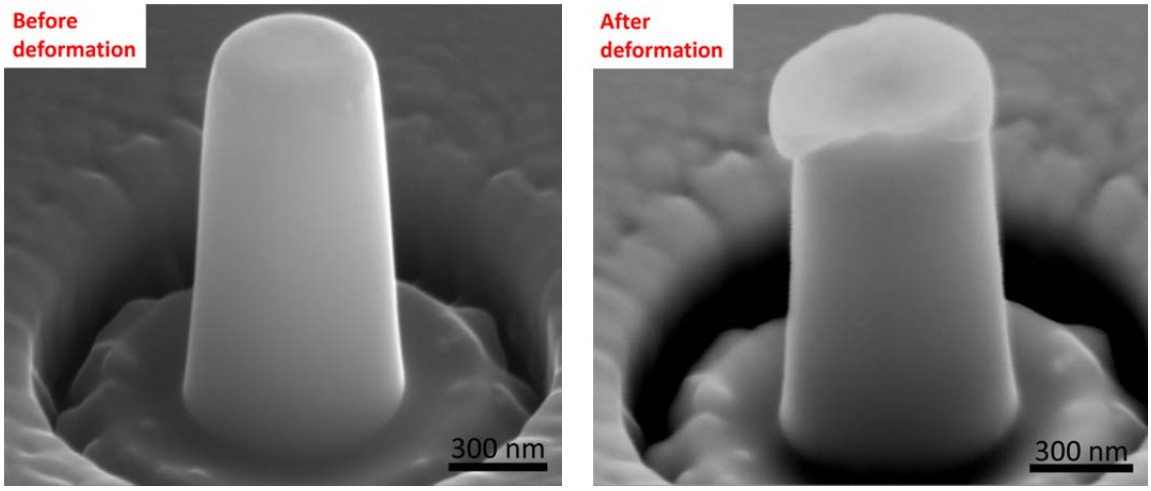

(b) (c)

Figure 6.16 (a) Compressive stress-strain response of a single crystalline 590 nm pillar fabricated on a martensite twin of the $Ni_{45}Mn_{36.6}Co_5In_{13.4}$ specimen. The compression (longitudinal) axis of the pillar is oriented along the [100] direction of the austenite. SEM images of this pillar, (b) before deformation and, (c) after deformation.

6.5 Summary and Conclusions

In this chapter, $Ni_{45}Mn_{36.6}Co_5In_{13.4}$ meta-magnetic SMAs were investigated at micron and sub-micron length scales by testing compression pillars at room temperature and in the martensite phase. The compression pillars were fabricated on the martensite twins in a way that their compression (longitudinal) axis were in the [100] direction of the austenite. Size effects in the martensite variant reorientation and magnetic field-induced phase transformation were studied in these compression pillars having diameters between 10 μm and 1 μm. The main findings and conclusions can be summarized as follows;

- Martensite variant reorientation was found to be size dependent in $Ni_{45}Mn_{36.6}Co_5In_{13.4}$ meta-magnetic SMAs. The pillars with the 10 μm size showed 20-28 MPa martensite reorientation stresses whereas the 5 μm pillars exhibited higher martensite reorientation stresses of between 40 MPa and 50 MPa. A stress-plateau was observed for every pillar tested in these sizes during the reorientation process. These pillars were deformed up to 3% and 4% strains and except the elastic strain of martensite, all the applied strain remained in the pillars upon unloading.
- 8T and 12T magnetic fields were applied to the deformed pillars to obtain recovery due to the field-induced phase transformation at room temperature (300K). The martensite to austenite phase transformation took place in the 10 μm and the 5 μm pillars when the field was applied. After removal of the field, the martensitic pillars were obtained at room temperature in a self-accommodated

morphology. These findings show that the field-induced phase transformation can be achieved down to 5 μm sample size with no significant size effect in the required magnetic field.

- Single crystalline $Ni_{45}Mn_{36.6}Co_5In_{13.4}$ pillars with 1 μm and 590 nm diameters showed plastic deformation at around 2000 MPa. These pillars did not exhibit martensite reorientation. Since the drop in the martensitic transformation temperature (M_s) is expected at this length scale, the pillars might be partially in austenite phase even though they were fabricated from the martensite twins. Therefore, the plastic deformation of these pillars might be associated with the plasticity in austenite as well as martensite.

CHAPTER VII

SUMMARY, MAIN CONCLUSIONS AND FUTURE DIRECTIONS

7.1 Summary and Main Conclusions

Size effects in superelasticity, stress- and magnetic field-induced martensite variant reorientation, and magnetic field-induced phase transformation were studied using single crystalline bulk and pillar ferromagnetic shape memory alloy (FSMA) samples with sizes ranging from 10 μm down to 200 nm in this dissertation. These mechanisms are responsible from the conventional shape memory and magnetic shape memory effects and therefore, investigating them at small structural length scales is critical for the utilization of these FSMAs in small scale devices.

In order to study the effect of small length scales on the reversible shape change mechanisms for superelasticity, magnetic field-induced martensite reorientation and phase transformation, micropillar testing was employed. Micropillars were the small single crystalline compression samples that resemble the bulk compression specimens. Since they were fabricated from their bulk counterparts, the major compositional differences between the pillars are eliminated. The micropillars are very similar to the bulk compression samples in terms of the dimensionality and are not constrained as some of the other small scale samples, i.e., thin films. This allows them to meet the requirements needed for the micron/submicron size samples in the present work. Thus,

our focus has been to study the aforementioned reversible shape change mechanisms in unconstrained geometries.

Single crystalline $Ni_{54}Fe_{19}Ga_{27}$ FSMA oriented along the [110] direction was used to investigate the size effects in two-stage superelasticity. This material was selected because it exhibits two-stage martensitic transformation at room temperature in bulk form. Even though there were studies reported on the size effects in superelasticity, there has been no work in the literature studying the size effects in the two-stage martensitic transformation. The results revealed an increase in the critical stress for austenite to martensite phase transformation which led to the suppression of two-stage martensitic transformation at and below 1 μm pillar size. Increase in the critical stress was shown to be due to decreasing martensitic transformation temperatures with the reduction in the pillar size. Increase in the stress hysteresis was also significant at the 1 μm size. Suppression of superelasticity was determined in these pillars as the pillar size decreased.

Single crystalline $Ni_{50}Mn_{28.3}Ga_{21.7}$ oriented along the [100] direction of the austenite phase was used to study the size effects on martensite variant reorientation. The initial sample was in the martensite phase at room temperature and all the micropillars were prepared on the martensite twins of this specimen. There is no report systematically investigating the size dependence of the martensite reorientation. In the present study, it was clearly shown that the martensite reorientation is size dependent and becomes more difficult with the decreasing sample size. Even though the martensite reorientation/twinning stress significantly increased in the micropillars as compared to

the bulk specimen, it was still possible to magnetically activate the shape change in the micropillars due to the magnetic field-induced martensite reorientation. However, it required higher magnetic fields to reorient the martensite in the micropillars than the bulk material. This magnetic field requirement for the micropillars was even higher than the saturation field of the bulk specimen but it was still possible to magnetically activate the twin boundary motion. This was a surprising and a unique finding since the field-induced twin boundary motion was not expected above the saturation field of the bulk specimen. This was attributed to the increase in the saturation magnetic field with the reduction in size, which in turn gives rise to the increase in the magnetocrystalline anisotropy energy (MAE) in the micropillars. Possible reasons for such increase in MAE with reduction in size were discussed in the light of magneto-microstructural domain coupling.

Single crystalline $Ni_{45}Mn_{36.6}Co_5In_{13.4}$ oriented along the [100] direction of the austenite was selected to study the size effects in the magnetic field-induced phase transformation. The sample was a mixture of the austenite and the martensite phases at room temperature and the micropillars were fabricated on the martensite twins. Stress-induced martensite variant reorientation was found to be size dependent as seen in the $Ni_{50}Mn_{28.3}Ga_{21.7}$ micropillars. Magnetic field-induced phase transformation was shown to be still possible down to 5 μm length scale using the magnetic fields similar to what is required for the bulk samples. As a result, we suggest that the meta-magnetic SMAs showing the field-induced phase transformation can still be utilized in micron scale applications. On the other hand, our findings show that the magnetic field-induced

martensite variant reorientation in $Ni_{50}Mn_{28.3}Ga_{21.7}$ at 5 μm size scale was much more difficult than that of the bulk samples. Field-induced martensite reorientation took place below 0.8T in the bulk specimen whereas it started at 5T in the 5 μm pillar. However, while 7T field was needed for the magnetic field-induced martensite to austenite phase transformation in the bulk $Ni_{45}Mn_{36.6}Co_5In_{13.4}$ specimen which was a mixture of austenite and martensite, only 8T to 12T field levels were required for the field-induced phase transformation in the martensitic pillars down to 5 μm size. These findings reveal that the magnetic field-induced martensite variant reorientation is more size dependent than the magnetic field-induced phase transformation, which has not been demonstrated previously.

Decrease in the martensitic transformation temperature (M_s) with the reduction in the sample size is one of the major size effects observed in SMAs. In the present work, we demonstrated this effect on the sub-micron pillars. In the SMA pillar literature, increase in the critical stress for austenite to martensite phase transformation is attributed to the decrease in the M_s with the size. In this study, we not only demonstrated the same effect in the $Ni_{54}Fe_{19}Ga_{27}$ pillars during superelasticity but also showed the transition from the martensitic pillars to the austenitic pillars with the reduction in size. $Ni_{50}Mn_{28.3}Ga_{21.7}$ pillars fabricated from the martensite twins started to exhibit a superelastic response below 2 μm. This clearly showed the decrease in the transformation temperatures with the reduction in size for the first time on the martensitic pillars. Additionally, the direct plastic deformation without showing any indications for the martensite variant reorientation was obtained in the 1 μm

$Ni_{45}Mn_{36.6}Co_5In_{13.4}$ pillars machined from the martensite twins. Since the aforementioned $Ni_{50}Mn_{28.3}Ga_{21.7}$ pillars in 1 μm size became austenite due to decrease in the M_s, the same response can be expected in the 1 μm $Ni_{45}Mn_{36.6}Co_5In_{13.4}$ pillars. This suggests that the plastic deformation response in the 1 μm $Ni_{45}Mn_{36.6}Co_5In_{13.4}$ pillars might be associated with the plasticity in austenite. However, more observations are needed in order to prove this argument.

These findings on the size effects in the FSMAs should shed light into these three reversible shape change mechanism at the micron and submicron length scales.

7.2 Future Directions

The size effects observed in the present study are believed to be dependent on the magneto-microstructural coupling (i.e. the coupling between martensite twins and magnetic domain walls). Therefore, more work is needed to identify this magneto-microstructural coupling at the micron and nano length scales in order to fully understand the microstructural mechanisms responsible for the observed behavior functionality of these FSMAs at small structural length scales. It is important to determine the effect of the sample size on the twin size and the effect of the twin size on the magnetic domain size. The observed increase in the saturation magnetization and the magnetocrystalline anisotropy energy in the $Ni_{50}Mn_{28.3}Ga_{21.7}$ micropillars can therefore be explained in more detail. For this purpose, the magnetization should be locally measured and the twin-magnetic domain coupling should be captured by imaging in the unconstrained and/or free standing structures.

Even though performing compression experiments on the micron/submicron pillars was the main focus in the present work, various FIB cut specimens can be made to study the size effects in FSMAs. For example, investigating different size cantilevers in micron to nano thickness range can also provide valuable information on the size dependence of the reversible shape change mechanisms in FSMAs. There are several advantages of studying cantilevers. First of all, thin films have been the mostly studied small size samples in FSMAs. Some findings were demonstrated on the magnetic field-induced martensite variant reorientation in submicron thicknesses. Since the thin films have only one small dimension and the FIB machined cantilevers have three small dimensions, their response under magnetic field is expected to be different. Therefore, investigating this mechanism in cantilevers with submicron to nano size thicknesses gives an opportunity to directly assess the effect of dimensionality on the field-induced martensite reorientation. In addition to this, since cantilevers have a flat surface which can be made in the same level with the bulk specimen surface, it would be easier to locally investigate the magnetization response, i.e, scanning hall probe microscopy (SHPM) can be used to locally measure the magnetization. Additionally, cutting micro/nano compression pillars from FSMA thin films also gives an understanding on the dimensionality effect in the reversible shape change mechanisms, i.e, the thickness effect in thin films versus the effect of a small sample in 3-D.

The microstructural evolution in the micron/submicron pillars in the present work was indirectly shown to change with the reduction in size, i.e, the change in the twin size, the structure of martensite and the change in the stable phases at room

temperature due to decrease in the M_s. In order to have a direct evidence on the evolution of the microstructure with the decreasing pillar size, transmission electron microscopy (TEM) specimens should be prepared from the deformed pillars and the TEM analysis should be performed.

FIB can be used to make structures in a different shape of arrays such as pillar or cantilever arrays. The size dependence of the reversible shape change mechanisms observed in the present study can be incorporated in this type of an array system. Putting different size FSMA structures, for instance different size pillars, in an array of a desired shape can produce a device consisting of components having different characteristics. For example, the magnetic field requirement for the recovery of the pillars due to martensite reorientation was shown to increase with the reduction in the pillar size. This different magnetic field requirement can be used in an array having different size pillars. This may lead to utilize these arrays in various applications where different actuation levels are desired from different components of the device.

FIB technique also allows to machine complicated structures and even an entire micro/nano device. For example, micro/nano springs with various thicknesses can be engraved from a thin film or a thinned bulk FSMA, which can expand and contract with the application of magnetic field or stress. Therefore, the functionality of these different size micro/nano springs can be investigated. Ultimately, FIB can be used to machine complicated microdevices with different size components that can be activated at different field levels, e.g., a microdevice including different size micro/nano valves. This gives an opportunity to easily implement the FSMAs in small scale applications.

REFERENCES

[1] Karaca HE, Karaman I, Basaran B, Chumlyakov YJ, Maier HJ. Acta Mater 2006;54:233.

[2] Karaca HE, Karaman I, Basaran B, Ren Y, Chumlyakov YI, Maier HJ. Adv Funct Mater 2009;19:983.

[3] Arzt E. Acta Mater 1998;46:5611.

[4] Greer JR, Oliver WC, Nix WD. Acta Mater 2005;53:1821.

[5] Waitz T, Antretter T, Fischer FD, Simha NK, Karnthaler HP. J Mech Phys Solids 2007;55:419.

[6] Yu Q, Shan ZW, Li J, Huang XX, Xiao L, Sun J, Ma E. Nature 2010;463:335.

[7] Mughrabi H. Materials Science and Engineering 1978;33:207.

[8] Ganor Y, Shilo D, Shield TW, James RD. Appl Phys Lett 2008;93.

[9] Efstathiou C, Sehitoglu H, Carroll J, Lambros J, Maier HJ. Acta Mater 2008;56:3791.

[10] Hamilton RF, Sehitoglu H, Efstathiou C, Maier HJ. Acta Mater 2007;55:4867.

[11] Efstathiou C, Sehitoglu H, Kurath P, Foletti S, Davoli P. Scr Mater 2007;57:409.

[12] Sutou Y, Kamiya N, Omori T, Kainuma R, Ishida K, Oikawa K. Appl Phys Lett 2004;84:1275.

[13] Dunand DC, Mullner P. Adv Mater 2011;23:216.

[14] Kohl M, Liu Y, Krevet B, Durr S, Ohtsuka M. J Phys IV 2004;115:333.

[15] Tomozawa M, Kim HY, Yamamoto A, Hiromoto S, Miyazaki S. Acta Mater 2010;58:6064.

[16] Kohl M, Agarwal A, Chernenko VA, Ohtsuka M, Seemann K. Mater Sci Eng A-Struct Mater Prop Microstruct Process 2006;438:940.

[17] Barth J, Krevet B, Kohl M. Smart Mater Struct 2010;19.

[18] Krulevitch P, Lee AP, Ramsey PB, Trevino JC, Hamilton J, Northrup MA. J Microelectromech Syst 1996;5:270.

[19] Fu YQ, Zhang S, Wu MJ, Huang WM, Du HJ, Luo JK, Flewitt AJ, Milne WI. Thin Solid Films 2006;515:80.

[20] Wan D, Komvopoulos K. J Mater Res 2005;20:1606.

[21] Ishida A, Sato M. Acta Mater 2003;51:5571.

[22] Babanly MB, Lobodyuk VA, Matveyeva NM. Fiz Metallov Metalloved 1993;75:89.

[23] Busch JD, Johnson AD, Lee CH, Stevenson DA. J Appl Phys 1990;68:6224.

[24] Glezer AM, Blinova EN, Pozdnyakov VA, Shelyakov AV. J Nanopart Res 2003;5:551.

[25] Fu YQ, Shearwood C. Scr Mater 2004;50:319.

[26] Phillips FR, Fang D, Zheng HX, Lagoudas DC. Acta Mater 2011;59:1871.

[27] Frick CP, Orso S, Arzt E. Acta Mater 2007;55:3845.

[28] Clark BG, Gianola DS, Kraft O, Frick CP. Adv Eng Mater 2010;12:808.

[29] Juan JS, No ML, Schuh CA. Nature Nanotechnology 2009;4:415.

[30] Juan JMS, No ML, Schuh CA. Adv Mater 2008;20:272.

[31] Chen Y, Schuh CA. Acta Mater 2011;59:537.

[32] Waitz T, Kazykhanov V, Karnthaler HP. Acta Mater 2004;52:137.

[33] Frommen C, Wilde G, Rosner H. J Alloy Compd 2004;377:232.

[34] Norfleet DM, Sarosi PM, Manchiraju S, Wagner MFX, Uchic MD, Anderson PM, Mills MJ. Acta Mater 2009;57:3549.

[35] Manjeri RM, Qiu S, Mara N, Misra A, Vaidyanathan R. J Appl Phys 2010;108.

[36] Frick CP, Clark BG, Orso S, Schneider AS, Arzt E. Mater Sci Eng A-Struct Mater Prop Microstruct Process 2008;489:319.

[37] Dimiduk DM, Uchic MD, Parthasarathy TA. Acta Mater 2005;53:4065.

[38] Uchic MD, Dimiduk DM, Florando JN, Nix WD. Science 2004;305:986.

[39] Uchic MD, Dimiduk DA. Mater Sci Eng A-Struct Mater Prop Microstruct Process 2005;400:268.

[40] Volkert CA, Lilleodden ET. Philos Mag 2006;86:5567.

[41] Kim JY, Jong DC, Greer JR. Acta Mater 2010;58:2355.

[42] Frick CP, Clark BG, Orso S, Sonnweber-Ribic P, Arzt E. Scr Mater 2008;59:7.

[43] Ye J, Mishra RK, Pelton AR, Minor AM. Acta Mater 2010;58:490.

[44] Chen IW, Chiao YH, Tsuzaki K. Acta Metallurgica 1985;33:1847.

[45] Guimaraes JRC, Rios PR. J Mater Sci 2010;45:1074.

[46] Leslie WC, Miller RL. Transactions of the ASM 1964;57:972.

[47] Roytburd AL, Kim TS, Su QM, Slutsker J, Wuttig M. Acta Mater 1998;46:5095.

[48] Greer JR, Nix WD. Phys Rev B 2006;73.

[49] Shan ZW, Mishra RK, Asif SAS, Warren OL, Minor AM. Nat Mater 2008;7:115.

[50] Scheerbaum N, Hinz D, Gutfleisch O, Muller KH, Schultz L. Acta Mater 2007;55:2707.

[51] Reinhold M, Kiener D, Knowlton WB, Dehm G, Mulllner P. J Appl Phys 2009;106.

[52] Buschbeck J, Niemann R, Heczko O, Thomas M, Schultz L, Fahler S. Acta Mater 2009;57:2516.

[53] Chernenko VA, Anton RL, Kohl M, Barandiaran JM, Ohtsuka M, Orue I, Besseghini S. Acta Mater 2006;54:5461.

[54] Heczko O, Thomas M, Buschbeck J, Schultz L, Fahler S. Appl Phys Lett 2008;92.

[55] Jenkins CA, Ramesh R, Huth M, Eichhorn T, Porsch P, Elmers HJ, Jakob G. Appl Phys Lett 2008;93.

[56] Thomas M, Heczko O, Buschbeck J, Rossler UK, McCord J, Scheerbaum N, Schultz L, Fahler S. New J Phys 2008;10.

[57] Thomas M, Heczko O, Buschbeck J, Schultz L, Fahler S. Appl Phys Lett 2008;92.

[58] Zhang Y, Hughes RA, Britten JF, Gong W, Preston JS, Botton GA, Niewczas M. Smart Mater Struct 2009;18.

[59] Zhang YP, Hughes RA, Britten JF, Preston JS, Botton GA, Niewczas M. Phys Rev B 2010;81.

[60] Giannuzzi LA, Stevie FA. Micron 1999;30:197.

[61] Omori T, Kamiya N, Sutou Y, Oikawa K, Kainuma R, Ishida K. Mater Sci Eng A-Struct Mater Prop Microstruct Process 2004;378:403.

[62] Oikawa K, Ota T, Ohmori T, Tanaka Y, Morito H, Fujita A, Kainuma R, Fukamichi K, Ishida K. Appl Phys Lett 2002;81:5201.

[63] Li JQ, Liu ZH, Yu HC, Zhang M, Zhou YQ, Wu GH. Solid State Commun 2003;126:323.

[64] Liu ZH, Zhang M, Cui YT, Zhou YQ, Wang WH, Wu GH, Zhang XX, Xiao G. Appl Phys Lett 2003;82:424.

[65] Santamarta R, Font J, Muntasell J, Masdeu F, Pons J, Cesari E, Dutkiewicz J. Scr Mater 2006;54:1105.

[66] James RD, Hane KF. Acta Mater 2000;48:197.

[67] Sehitoglu H, Karaman I, Anderson R, Zhang X, Gall K, Maier HJ, Chumlyakov Y. Acta Mater 2000;48:3311.

[68] Bhattacharya K. Microstructure of Martensite. Oxford: Oxford University Press; 2003.

[69] Karaca HE, Karaman I, Chumlyakov YI, Basaran B, Maier HJ. Personal collection, N. Ozdemir.

[70] Chumlyakov YI, Kireeva IV, Panchenko EY, Timofeeva EE, Pobedennaya ZV, Chusov SV, Karaman I, Maier H, Cesari E, Kirillov VA. Russ Phys J 2008;51:1016.

[71] Monroe JA, Karaman I, Karaca HE, Chumlyakov YI, Maier HJ. Scr Mater 2010;62:368.

[72] Cech RE, Turnbull D. Transactions of the American Institute of Mining and Metallurgical Engineers 1956;206:124.

[73] Meng QP, Rong YH, Hsu TY. Phys Rev B 2002;65.

[74] Brofman PJ, Ansell GS. Metallurgical Transactions a-Physical Metallurgy and Materials Science 1983;14:1929.

[75] Glezer AM, Pankova MN. J Phys IV 1995;5:299.

[76] Karaman I, Kulkarni AV, Luo ZP. Philos Mag 2005;85:1729.

[77] Karaca HE, Karaman I, Lagoudas DC, Maier HJ, Chumlyakov YI. Scr Mater 2003;49:831.

[78] Girault B, Schneider AS, Frick CP, Arzt E. Adv Eng Mater 2010;12:385.

[79] Guimaraes JRC. Scr Mater 2007;57:237.

[80] Waitz T. Acta Mater 2005;53:2273.

[81] Sun QP, He YJ. Int J Solids Struct 2008;45:3868.

[82] Kim YH, Cho GB, Hur SG, Jeong SS, Nam TH. Mater Sci Eng A-Struct Mater Prop Microstruct Process 2006;438:531.

[83] Liu Y, McCormick PG. Acta Metall Mater 1994;42:2401.

[84] McCormick PG, Liu YN. Acta Metall Mater 1994;42:2407.

[85] Salzbrenner RJ, Cohen M. Acta Metallurgica 1979;27:739.

[86] Murray SJ, Marioni M, Allen SM, O'Handley RC, Lograsso TA. Appl Phys Lett 2000;77:886.

[87] Tickle RJ. Ph.D. Thesis, University of Minnesota; 2000.

[88] Karaca HE, Karaman I, Basaran B, Lagoudas DC, Chumlyakov YI, Maier HJ. Acta Mater 2007;55:4253.

VITA

Name:	Nevin Ozdemir
Address:	Materials Science and Engineering Program, c/o Dr. Ibrahim Karaman Texas A&M University, College Station, TX 77843-3003
Email Address:	nevozdemir@gmail.com
Education:	B.S., Materials Science and Engineering, Anadolu University, 2003 M.S., Materials Engineering, New Mexico Institute of Mining and Technology, 2006